An X-Ray Photoelectron Spectroscopy Study of Multilayered Transition Metal Carbides (MXenes)

A Thesis

Submitted to the Faculty

of

Drexel University

by

Joseph Halim

in partial fulfillment of the

requirements for the degree

of

Doctor of Philosophy

June 2016

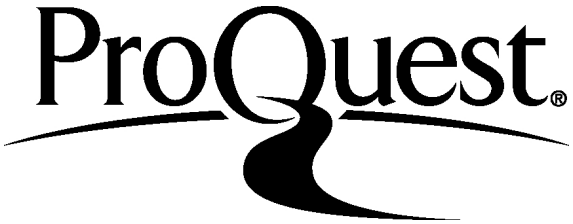

DEDICATIONS

To my mother Salwa,

Thank you for your unconditional love,

support and motivation to be a better person.

ACKNOWLEDGEMENTS

I would like to express my gratitude and appreciation to my advisor, Prof. Michael Barsoum, for his continuous support, curiosity about science, pushing my scientific boundaries to step out of my comfort zone and explore new areas in the materials science field. Most importantly, giving me the freedom in expressing my scientific ideas as well as performing them. I would like to equally thank my co-advisor, Prof. Johanna Rosén for her never-ending support, encouragement and being very passionate about research and exploring new areas in the field, in addition to finding the time for a progress meeting once per week despite being extremely busy. I feel honoured and lucky to have such great PhD advisors who helped me to grow as a scientist and a person and taught me to look at the bigger picture

I would like to thank my committee members: Prof. Yury Gogotsi, Prof. Lars Hultman, Prof. Steve J. May, and Prof. Goran Karapetrov for finding the time through their busy schedules to provide feedback and guidance while reviewing and evaluating this work.

I would like to thank our collaborator Prof. Per Eklund, at Linköping University, for providing insights on understanding MXenes and finding the time to read, review and provide constructive comments to the manuscripts.

I am especially thankful to Dr. Lars-Åke Nälsund and Dr. Kevin Cook, my two XPS masters. No words can express my sincere gratitude for all the knowledge and experience you continuously provide.

I would like to thank all members (current and former) of the MAX/MXene group for their help and support. I want to thank in particularly the following people whom worked closely to me and contributed to this work: Dr. Michael Naguib, Sankalp Kota, Michael Ghidiu, Dr. Maria Lukatskaya, Dr. Kelsey Hatzell, Dr. Darin J. Tallman,

Grady Bentzel, Dr. Babak Anasori, Dr. Nina Lane, Dr. Olha Mashtalir, Chang (Evelyn) Ren, Boris Dyatkin, Elisa Mayerberger, Katie Van Aken, and Dr. John (Jake) McDonough. Especially, I would like to thank Michael Naguib, Michael Ghidiu, Sankalp Kota, Kelsey Hatzell and Maria Lukatskaya for their friendship and support.

I wanted to thank the funding agencies that made it possible to conduct this research. The work has been funded by the Swedish Research Council, and the Swedish Foundation for Strategic Research through the Synergy Grant FUNCASE Functional Carbides for Advanced Surface Engineering. I would like to thank the Drexel Core Facility and staff, especially Dr. Dmitri Barbash, for assistance with the characterization techniques.

I am very grateful to the staff members of Materials Science and Engineering Department and Drexel Nanomaterials Institute stuff, particularly Keiko Nakazawa, Yenneeka Long, Sarit Kunz and Danielle Tadros Kopicko for their patience, great help and support with all the administrative work.

All my friends and colleagues in Drexel University and Linköping University; Thank you for your support and help.

In the end, I would like to thank my close very supportive friends, especially Rim Mofid, and my family for your never-ending support for all my decisions and your encouragement to always follow my dreams.

TABLE OF CONTENTS

LIST OF TABLES

LIST OF FIGURES

LIST OF ABBREVIATIONS

BE	binding energy
DFT	Density Function Theory
DI	Deionized
DMSO	Dimethylsulfoxide
Ef	Fermi-edge
DOS	density of states
FETs	field-effect transistor
FTIR	Fourier transform infrared
FWHM	Full width at half maximum
GL	Gaussian Lorentzian
H SA	hemispherical analyser
hBN	hexagonal boron nitride
PDF	pair distribution function
PEG	polyethylene glycol
PEI	Polyethylenimine
PEO	poly(ethylene oxide)
PL	Photoluminescent
LIB	Li-ion batteries
LA	Lorentzian Asymmetric
NMR	Nuclear magnetic resonance
PVA	polyvinyl alcohol
SAM	self-assembled monolayers
TEM	transmission electron microscopy
TPD	temperature programmed desorption
RT	Room temperature
XAS	X-ray absorption spectroscopy
XPS	X-ray photoelectron spectroscopy
XRD	X-ray diffraction
2D	two-dimensional

ABSTRACT

Recently, a new family of two-dimensional (2D) early transition metal carbides and carbonitrides, labeled MXenes, was discovered at Drexel University. MXenes are produced by selectively etching mostly Al from Al-containing MAX phases and replacing Al with surface termination groups. Theoretically it has been predicted that changing the nature of the surface terminations, T, can change MXenes' properties, such as electronic and optical, resulting in changes in performance in various applications such as electrodes for Li-ion batteries. Prior to this work, there had been little systematic effort devoted to carefully identifying and quantifying the exact nature of T. In this work, high resolution XPS spectra of multilayered $Ti_3C_2T_x$, Ti_2CT_x, Ti_3CNT_x, Nb_2CT_x, $Nb_4C_3T_x$, V_2CT_x, Mo_2CT_x, $Mo_2TiC_2T_x$, and $Mo_2Ti_2C_2T_x$ were acquired and analyzed. The influence of the M and X elements, the order of MXene, *n*, aging, Ar^+ sputtering, and the concentration/nature of the etchants on the amounts of –O, –OH and –F, were systematically investigated.

XPS analysis confirmed the intercalation of Li^+ ions upon etching Ti_3AlC_2 using a mixture of LiF and HCl or LiCl and HF; when $Ti_3C_2T_x$ multilayers is immersed in RbCl or NaCl solutions, cation exchange resulted in the replacement of Li^+ ions with Rb^+ or Na^+, respectively. Similar cation intercalations were confirmed when treating HF-etched $Ti_3C_2T_x$ samples with $Ti_3C_2T_x$ with alkali metal hydroxides, such as NaOH and KOH. Based on quantification of the various chemical species before and after treatment, a mechanism was suggested where the reduction of -F terminations took place by exchanging with -OH and -O terminations and/or complete removal of Ti-F species and converting them to TiO_2-F_x.

From XPS peak fits for all MXene samples in this study, it was established that x was ≈ 2.0±0.2. Both -F and -OH terminations are formed during etching through the reaction of MXene with HF or H_2O, respectively. However, for the -O terminations to form, a mechanism was suggested were some of the -OH terminations dissociate into -O termination and H^+, where the latter reacts with an intercalated H_2O forming $[H_3O]^+$. The latter are then replaced with cations via ion exchange. This reaction has been suggested based on the trend that, for most MXenes analyzed, the ratio between -O terminations and adsorbed water plus cations is equal to unity or lower, suggesting that all H^+ that dissociates from the -O terminations reacts with H_2O molecules to form H_3O^+. Only five compounds out of the sixteen studied were found not to follow this trend (in those cases the ratio was higher than unity) where further investigation is needed to determine the cause of this anomaly.

Given that recent work reported that the average oxidation state of Ti in $Ti_3C_2T_x$ is + 2.4, the average oxidation state of C - for 8 different samples - was determined to be ≈ -2.6±0.1. It is thus reasonable to conclude that the average oxidation states of Ti and C in $Ti_3C_2T_x$ are weakly dependent on the etching conditions and/or intercalated cations. Similarly, the average oxidation state of C - for 2 different samples – was determined to be ≈ -3.96±0.2 assuming the oxidation state of V determined in recent work to be +3.0.

Based on this work, it is now possible to quantify the nature of the surface terminations in MXenes; information that can, in turn, be used to better design and tailor these novel 2D materials for various applications.

CHAPTER 1: INTRODUCTION

The isolation and characterization of graphene in 2004 [1] from graphite has marked the beginning of a new form of materials called two-dimensional (2D) materials. 2D solids can be defined as a form of material that has an infinite length in the x and y direction and a thickness equal to a single atomic plane which is 0.34 nm for graphene [2]. However, the scientific community tends to define 2D materials as materials that exhibit novel properties different from their 3D counterparts when reaching a certain thickness. For instance, the electronic structure of graphite changes to a zero-gap semiconductor (referred to as a semi metal) when its thickness ranges between 1 to 10 monolayers. At that thickness range Bianco *et al*. [3] defined graphene to be 2D. Thus, one can consider any material reaching a certain thickness where it exhibits properties different from its 3D counterpart to be called 2D.

Graphene became the most researched 2D material not only because it was the first 2D material isolated into single flakes but because of its impressive properties such as ballistic conductivity [1], high thermal conductivity [4], high in-plane mechanical strength [5], optical transparency of visible light reaching 97.7% per monolayer [6]. These properties rendered graphene a promising material for various applications such as field-effect transistors (FETs) [7,8], memory devices [9,10], photovoltaic devices, transparent electrodes[11-13], electron acceptors [14], and light absorbers [15] and electrochemical sensors [16-18].

After the discovery of graphene, scientists devoted their efforts in finding new 2D materials with different chemistries and various electronic structures. Among the earliest discovered was hexagonal boron nitride, (hBN) which is an insulator [19]. It also has an extremely smooth surface that allows it to be deposited between graphene

and SiO_2 wafers in electronics to prevent the distortion of the graphene electronic properties due to the roughness of the SiO_2 wafers [20]. Following hBN, other 2D materials ranging from insulators to semiconductors to metals to even superconductors were discovered. These 2D materials include transition-metal dichacogenides (TDMs) [21], transition metal oxides and hydroxides including clays [22], and monoelemental 2D materials such as silicone [23], phosphorene [24] and germanene [25].

The high surface to volume ratio which 2D materials possess makes their surfaces reactive allows them to interact easily with other elements and compounds through chemical surface functionalization. This in turn can alter their optical and electronic properties in addition to improving charge storage, chemical and biological sensing and other applications as well [26].

The electronic structure of graphene can be altered from a zero-gap semiconductor to a p-type or n-type semiconductor using several methods such as:

1. Metallic contact: Immersing graphene films in $AuCl_3$ or $HAuCl_4$ solutions, where Au nanoparticles can adhere to graphene's surface resulting in a heavily p-doped graphene [27].
2. Acid modification: By immersing graphene in nitric acid solution, the HNO_3 molecules are adsorbed on the graphene's surface resulting again in a heavily p- doped material [28,29].
3. Molecule coating [30]: n-type semiconducting graphene can be achieved through introducing a dipole moment using self-assembled monolayers (SAM) of polymers or molecules such as polyethylene glycol (PEG) [31], polyvinyl alcohol (PVA) [32], polyethylenimine (PEI) [33] and poly(ethylene oxide) (PEO) [34], which are more electropositive than C. These SAM polymers or molecules can be adsorbed on the surface of

graphene to tailor its electronic properties with little damage to the graphene lattice.

Similar to graphene, various chemical methods can be used to tailor the electronic properties of TMCs such as

1. Molecular physisorption: Physisorption of electronegative gaseous molecules such as O_2 or H_2O molecules result in electronically depleted n-type MoS_2 and $MoSe_2$ solids that are strongly photoluminescent (PL) [35], while less electronegative gaseous molecules such as NO_2 can be used as p-type dopants for WSe_2 [36]. NO_2 molecules would adsorb on WSe_2 surface and transfer electrons from WSe_2 due to its strong oxidizing nature.
2. Metallic nanoparticles: depositing metallic nanoparticles of Au, Ag, Pd or Pt on MoS_2 has shown to induce p-type doping [37,38].

In 2011, a new family of 2D materials of transition metal carbides and nitrides was discovered [39,40] and labeled “MXene”. MXenes are synthesized by selective etching of the “A” layers from the layered transition metal carbides and nitrides known as MAX phases. The latter have a general formula of $M_{n+1}AX_n$ (n=1, 2, or 3), where M represents a transition metal, A represents mostly elements from the III A or IV A group elements such as Al, Ga, Si, or Ge, and X represents C and/or N [41].

MXenes have shown promise for several applications such as energy storage [42-46], water purification [47,48] , electrochemical actuators [49], photocatalysis [50], transparent conductive electrodes [51], and sensors [52]. When the A element is removed from the MAX phase to produce MXene, it is replaced by a mixture of surface functional groups or surface terminations. Thus one can consider MXene as a family of 2D materials that is readily functionalized with a formula of $M_{n+1}X_nT_x$, where T stands for surface termination groups. Early one, the latter were shown to be a mixture of O,

OH and/or F groups [53]. A lot of theoretical work using Density Function Theory (DFT) calculations was done to understand how these surface terminations can affect the electronic structure of MXenes and what influence they have on their properties [54-57]. However, there has been little systematic experimental studies to accurately determine the exact nature and quantity of these surface termination groups.

CHAPTER 2: BACKGROUND AND LITERATURE SURVEY

In this chapter the importance of utilizing XPS for chemical characterization of nanomaterials, in particular 2D materials, will be reviewed. I will summarize the status of the field of 2D metal carbides and nitrides (MXenes) focusing on synthesis methods and structural and chemical studies and state the research objectives of this work. Furthermore, XPS studies of the interaction of water with metal oxides, in particular titanium oxide, and metal carbides will be reviewed, since they are the closest materials systems to MXenes when trying to understand their surface terminations.

2.1 XPS for chemical analysis of 2D materials

Several techniques are used to investigate the chemistry of 2D materials in particular, such as:

1. Fourier transform infrared (FTIR) spectroscopy: This technique can identify several groups (nitro groups, oxygen-containing groups, *etc*.) and bonds (C-F, C-N, *etc*. [58]). However, it is not ideal for elemental quantification.
2. Raman spectroscopy: This technique can also identify various bonds as it measures their atomic vibrations. In 2D materials it is used to determine the number of layers or doping levels. For example, in graphene, p (n)-type doping can cause a decrease in the wavelength (increase in the wavelength) of the 2D and G bands of graphene due to the influence of the Fermi level on the photon frequencies of graphene. However, it is not possible to perform elemental quantification using Raman [59].
3. X-ray photoelectron spectroscopy (XPS): this technique is ideal for exact elemental quantification for 2D materials in particular as it is a surface

sensitive technique. Its penetration depth is about 10 nm. It is also used for the determination of the chemical components and the electronic states of the elements in nanomaterials and 2D materials. One of the limitations of XPS is that it is not able to detect hydrogen.

Looking at the above techniques, it is obvious that XPS is the most ideal technique for identifying and quantifying elements and surface terminations in these materials. In fact, XPS has been used extensively for identifying and quantifying various chemical species in 2D materials. For instance, Sheng *et al.* [60] explored the nitrogen (N) bonding configurations in N doped graphene synthesized by thermal annealing of graphite oxide using melamine as a N source. From the XPS results shown in **(Figure 1.a**). After annealing in the presence of melamine, the (C-C) peak is shifted to higher binding energy and its full width half maximum (FWHM) increases due to the distortion of the lattice resulting from the introduction of N atoms (**Figure 1.b**). Other small new peaks appear at 285.8 and 287.5 eV corresponding to sp^2-C and sp^3-C atoms, respectively. The high-resolution N 1s XPS spectra for N-doped graphene (**Figure 1.d**).

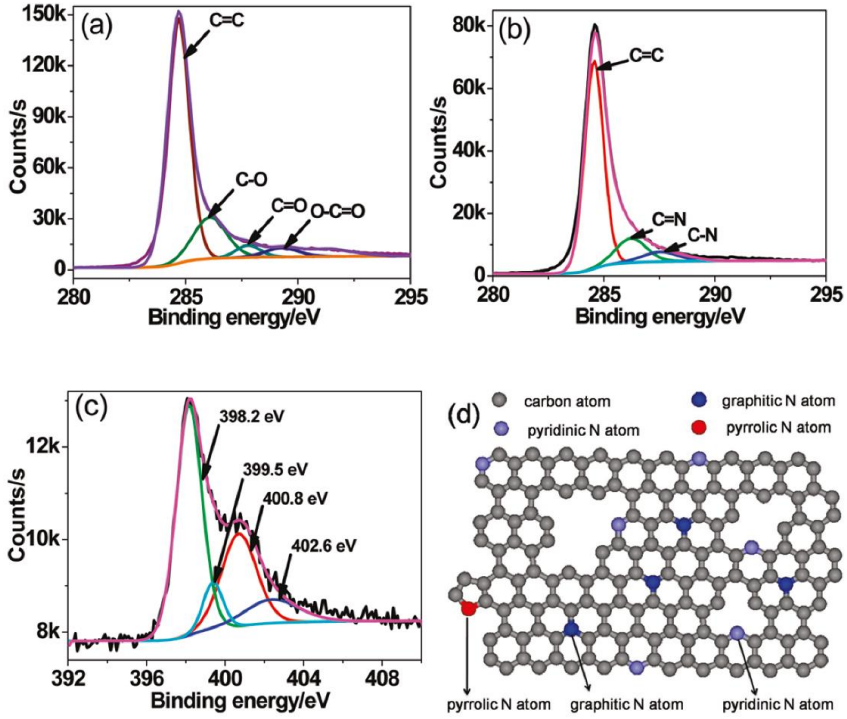

Figure 1. *(a) XPS high-resolution C 1s spectra of pristine graphene prepared by thermal annealing at 800 °C, (b) C 1s and (c) N 1s spectra of nitrogen doped graphene prepared by thermal annealing of graphite oxide in the presence of melamine at 800 °C, and (d) schematic crystal structure of nitrogen doped graphene. Reprinted with permission from (Ref.[60]). Copyright (2011) American Chemical Society.*

XPS has been used to investigate surface functionalization of other 2D materials beyond graphene. Shi *et al.* [61] reported on the effective decoration of Au nanoparticles on 2D MoS_2, where the former exhibited a remarkable p-doping effect to the MoS_2-based transistors. Decorating the MoS_2 flakes with Au nanoparticles was performed by immersing the flakes in a $AuCl_3$ solution. The high-resolution XPS spectra of Mo 3d and S 2p regions (**Figures 2.a** and **b**, respectively) show no change in the binding energies of Mo or S after Au nanoparticle decoration. This indicates that doping of Au does not severely alter the crystallinity of MoS_2, in other words not many defects are produced due to the doping process. The high-resolution spectra of Au 4f and Cl 2p after $AuCl_3$ treatment confirm the doping of Au (Figure 2.c). The presence of a Cl signal in the Cl 2p region (Figure 2**.**d) confirmed that no physical adsorption of

AuCl4- on the MoS_2 surface took place. Elemental composition obtained from the XPS spectra show an arbitrary formula of $MoS_{1.9}Au_{0.044}$ for the MoS_2 decorated with Au particles.

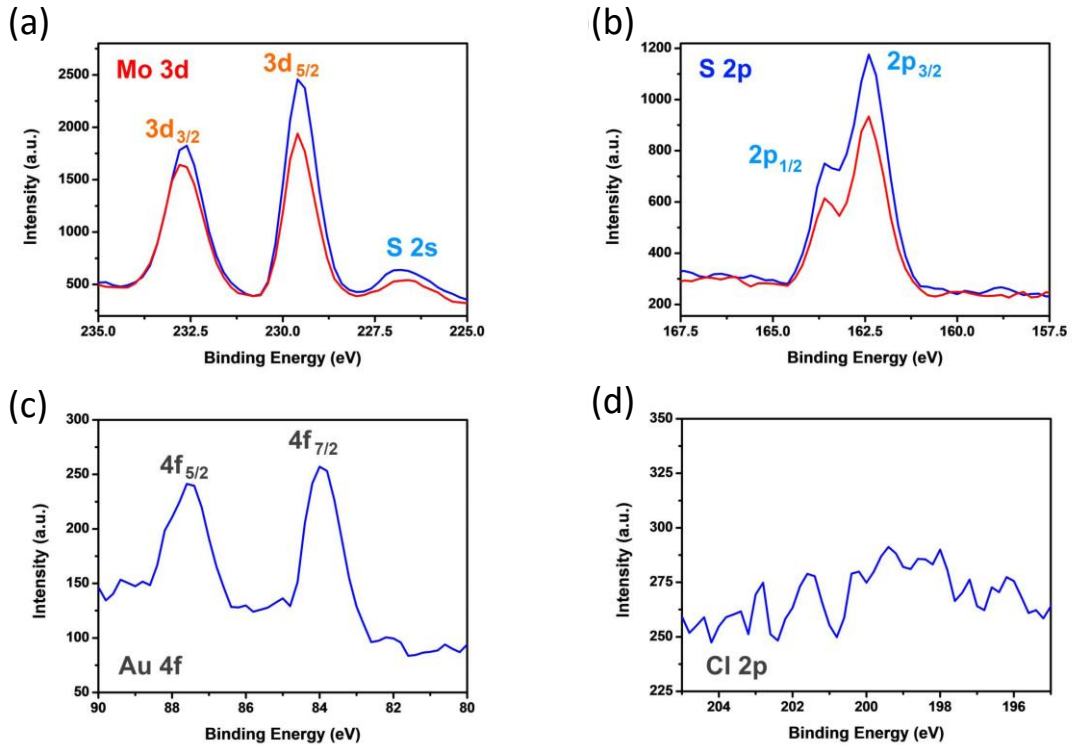

Figure 2. *High-resolution XPS spectra of (a) Mo 3d and (b) S 2p regions for MoS_2 before Au nanoparticle decoration (red curve) and after Au nanoparticles decoration (blue curve), (c) Au 4f and (d) Cl 2p regions for MoS_2 after Au nanoparticle decoration (Ref.[61]).*

Furthermore, Lei *et al*. [62] reported on the functionalization of InSe with Ti^{4+} based on Lewis acid-base chemistry using a solution of $TiCl_4$ to create $[Ti^{4+}{}_n(InSe)].Cl^-{}_{4n}$. The authors used XPS to confirm the formation of Ti-Se bonds after reacting n-type InSe by $TiCl_4$ forming p-type $[Ti^{4+}{}_n(InSe)]$ complexes. As shown in **Figure 3**, a new chemical species appeared in the Se 3d region at a higher binding energy after the $TiCl_4$ treatment due to the formation of Ti-Se bonds. The donation of lone pair electrons from the Se atoms reduces the electron density in the Se outer shells (4s and 4p orbitals), and a stronger attractive interaction is applied to the inner shells (3d) which results in the appearance of the higher binding energy peaks. Using the peak

area of the fitted components in **Figure 3**, it was deduced that 25% of the Se atoms are bonded to Ti, which is the same percentage of Se exposed to the $TiCl_4$. This functionalization method has led to the change of the electronic properties of InSe from n-type semiconductor to p-type semiconductor, allowing fabrication of n-p junctions without requiring heterostructure growth. Moreover, functionalization *via* Lewis acid-base reaction does not alter the structure of the host.

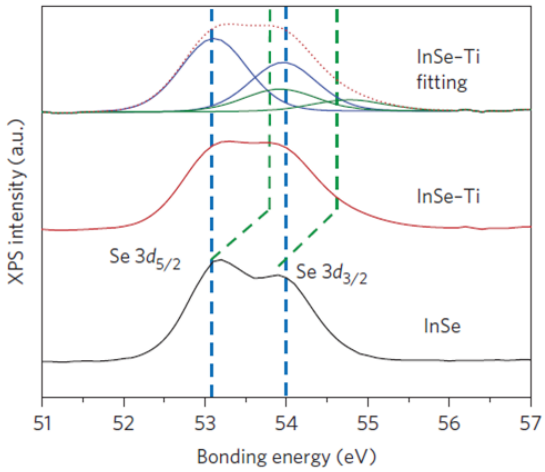

Figure 3. *High-resolution XPS spectra of Se 3d region for InSe before (black) and after (red) $TiCl_4$ treatment. The red dashed curve shows the fitting envelope of Se 3d region after treatment, showing two new components at a higher binding energy of 54.0 and 54.8 eV corresponding to the Se-Ti $3d_{5/2}$ and $3d_{3/2}$ respectively. (blue and green dashed lines correspond to the binding energies for Se in the pristine InSe and the Se-Ti after $TiCl_4$ treatment, respectively). Reprinted by permission from Nature Publishing Group, Nature Nanotechnology (Ref.[62]), copyright 2016.*

2.2 2D transition metal carbides and nitrides (MXenes)

MXenes are a recently reported new family of 2D metal carbides and carbonitrides [39,40,45,53]. They exhibit good electrical conductivity [63], hydrophilicity [53], can host different cations [43], and other compounds such as dimethylsulphoxide, urea, hydrazine monohydrate [64], and tetrabutylammonium hydroxide [65], and tunable surface terminations [54,57,66]. Owing to these unique combination of properties and in adding to the 2D morphology, MXenes were found to

be promising for energy storage applications such as Li-ion batteries [45,64,67-70], hybrid cells [71-73], electrochemical capacitors [42,43,74,75]. In addition to other applications such as sensors [52,76,77], actuators [49], photocatalysis [50], transparent conductive electrodes [51] and water purification [47,78]. Moreover, they were found to provide stability and durability for proton exchange membranes for fuel cells [79].

2.2.1. Synthesis of MXenes

MXenes are synthetized by selective etching of the "A" layers from a layered ternary transition metal carbides and nitrides family of more than 70 phases labeled MAX phases [41]. MAX phases have a general formula of $M_{n+1}AX_n$, where n = 1, 2, or 3, M is an early transition metal, A is an A-group element, and X is C and/or N as shown in **Figure 4**.

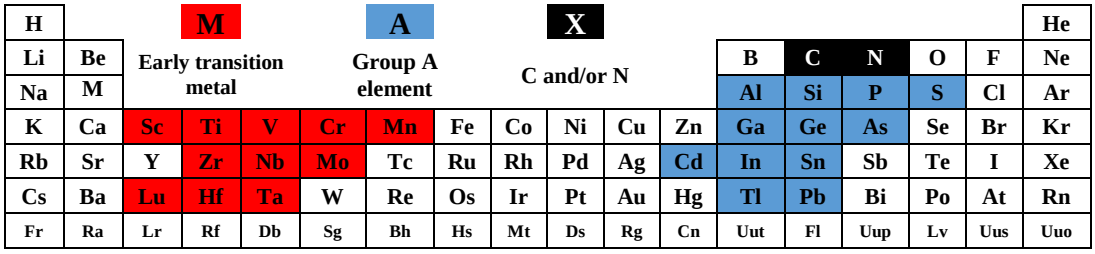

H																	He
Li	Be											B	C	N	O	F	Ne
Na	M											Al	Si	P	S	Cl	Ar
K	Ca	Sc	Ti	V	Cr	Mn	Fe	Co	Ni	Cu	Zn	Ga	Ge	As	Se	Br	Kr
Rb	Sr	Y	Zr	Nb	Mo	Tc	Ru	Rh	Pd	Ag	Cd	In	Sn	Sb	Te	I	Xe
Cs	Ba	Lu	Hf	Ta	W	Re	Os	Ir	Pt	Au	Hg	Tl	Pb	Bi	Po	At	Rn
Fr	Ra	Lr	Rf	Db	Sg	Bh	Hs	Mt	Ds	Rg	Cn	Uut	Fl	Uup	Lv	Uus	Uuo

Figure 4. *Periodic table showing elements from which MAX phases are composed, M: early transition metal (red), A: group A element (blue), and X: C and/or N (black) (Ref. [41,80,81]).*

MAX phases have a layered hexagonal crystal structure with MX blocks sandwiching layers of A-group elements (**Figure 5**). This particular arrangement of the M, A, and X atoms in the MAX phases leads to a significant difference between the M-X bonding compared to the M-A bonding. The M and X form a mixture of ionic, metallic and covalent bonds which are much stronger than the M and A metallic bond [82,83]. Taking advantage of this fact, Naguib *et al*. [39] were able to chemically etch the A element (Al) from Ti_3AlC_2 powders using hydrofluoric acid (HF) producing

exfoliated layers of Ti_3C_2, the first member of the MXene family. The operative reactions proposed are [39]:

$$Ti_3AlC_2 + 3HF = AlF_3 + 3/2H_2 + Ti_3C_2 \quad (1)$$

$$Ti_3C_2 + 2H_2O = Ti_3C_2(OH)_2 + H_2 \quad (2)$$

$$Ti_3C_2 + 2HF = Ti_3C_2F_2 + H_2 \quad (3)$$

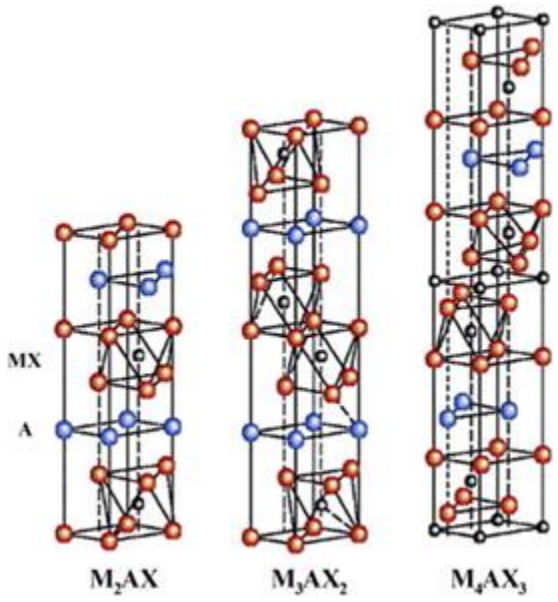

Figure 5. *MAX phases' unit cells: M_2AX (211), M_3AX_2 (312), and M_4AX_3 (413) (Ref.[84]).*

During etching, the Al in Ti_3AlC_2 is replaced with surface functional groups that are assumed to be a mixture of -OH, -O and/or -F [39]. Thus, as noted above, the correct general formula of MXene is $M_{n+1}X_nT_x$, where T stands for the surface termination groups. The as-produced MXenes were in the form of multilayers and cannot be easily delaminated into single flakes *via* sonication in water or isopropanol. This is mainly due to the interaction of the surface terminating groups with each other, keeping the flakes bonded together. Mashtalir *el al*. [64] introduced a method to delaminate $Ti_3C_2T_x$ using dimethylsulfoxide (DMSO). $Ti_3C_2T_x$ powders were intercalated first with DMSO, weakening the bonding between the layers, followed by sonication in water, resulting in a high yield of delaminated MXene (*d*-$Ti_3C_2T_x$) in the

form of colloidal suspensions. Other compounds such as tetrabutylammonium hydroxide [65] and isopropylamine [46] have been used to delaminate other MXenes such as Nb_2CT_x, Ti_3CNT_x and V_2CT_x. A schematic showing the entire synthesis procedure is shown in **Figure 6**.

Other etching systems were also used to convert Ti_3AlC_2 to $Ti_3C_2T_x$ including NH_4HF_2 [51] and HF + LiCl [85]. Interestingly, Ghidiu *et al.* [42] demonstrated that etching Ti_3AlC_2 using a mixture of LiF and HCl led to spontaneous delamination of the $Ti_3C_2T_x$ multilayers, MLs, without the need of the intercalation step.

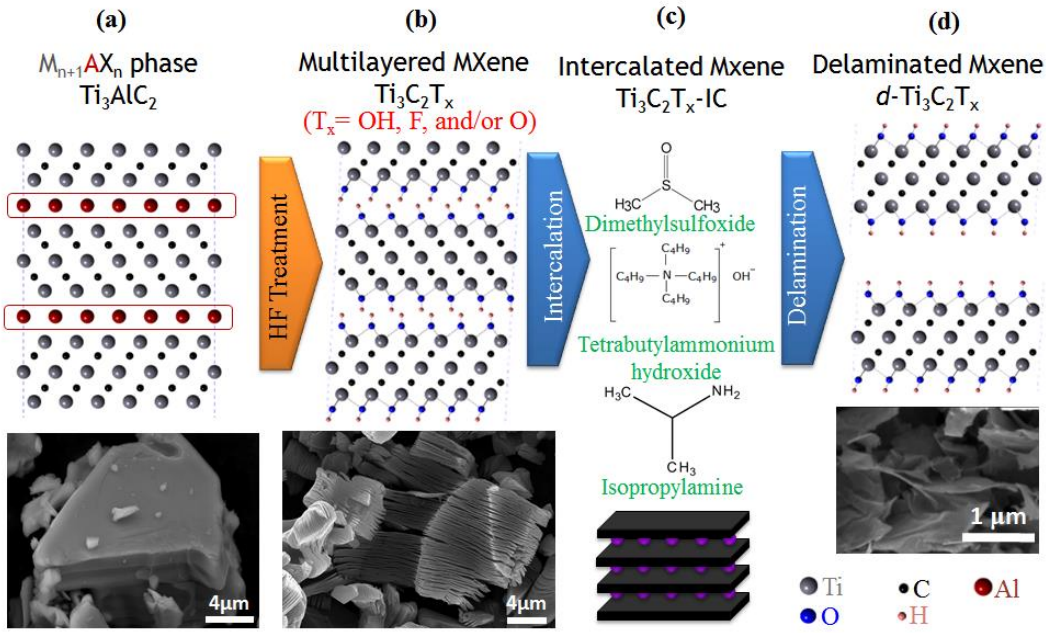

Figure 6. *Synthesis of MXenes from MAX phase, taking $Ti_3C_2T_x$ as an example: (a) Ti_3AlC_2 MAX phase powder immersed in HF acid, this results in (b) selective etching of Al and formation of multilayered $Ti_3C_2T_x$, (c) intercalation of the multilayered $Ti_3C_2T_x$ using various compounds: dimethylsulfoxide, tetrabutylammonium hydroxide or isopropylamine, which, (d) can be delaminated by sonication in water into separate flakes. Figure was adapted with permission from American Chemical Society (Ref. [39]) Copyright 2012. ACS Nano, and from Nature Publishing Group (Ref. [64]) Copyright 2013. Nature Communications.*

To date there have been 17 MXene compounds reported, including Ti_2CT_x, Nb_2CT_x, V_2CT_x, $(Ti_{0.5},Nb_{0.5})_2CT_x$, Mo_2CT_x $Ti_3C_2T_x$, $(V_{0.5},Cr_{0.5})_3C_2T_x$ Ti_3CNT_x Ti_3CN, $Ta_4C_3T_x$, $Nb_4C_3T_x$ [40,53,86], $Zr_3C_2T_x$ [87], $(Nb_{0.8}Ti_{0.2})_4C_3T_x$, $(Nb_{0.8},Zr_{0.2})_4C_3T_x$ [88], $Mo_2TiC_2T_x$, $Mo_2Ti_2C_3T_x$, and (where Mo and Ti form an ordered layer structure, with

Mo occupying the outer M layers and Ti occupying the inner M layers) and similarly $Cr_2TiC_2T_x$ where Cr occupies the outer layers [89]. All of these MXenes were synthetized by HF etching of their MAX phases at room temperature or at a slightly higher temperature ≈ 55 °C.

2.2.2. Surface termination of MXenes

As stated previously, the chemical etching of the MAX phases to produce MXenes results in the replacement of the Al layers with surface terminating groups that are assumed to be -O, -OH, and/or -F. Much theoretical work has been dedicated to investigating the most favorable positions for these surface terminations and how changes in the surface terminations would affect the properties of MXenes [39,90-94].

Regarding the position of the surface terminations, Enyashin et al. studied three different configurations (I, II, and III) for the OH terminations on Ti_3C_2 layer (**Figure 7**). In configuration I, the OH groups are positioned in the empty space between the three carbon atoms on the two sides of the MXene layer (**Figure 7.b, e**). For configuration II, the OH groups are located directly above the C atoms on both sides of the MXene layer (**Figure 7.c, f**), while configuration III is a combination of both I and II, where one OH group would occupy one of the positions on one side of the MXene layer and vice versa. By comparing the relative total energies for the three configurations, configuration II was the least stable, while configuration I was the most stable. The same results were also obtained for $Ti_3C_2F_2$ [91].

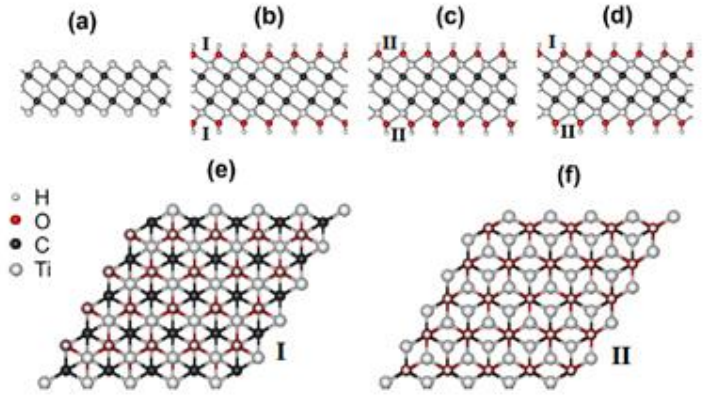

Figure 7. Atomic structures of Ti_3C_2 layer: (a) with no terminations (side view), (b) with OH terminations in *configuration I (side view), (c) with OH terminations in configuration II (side view), (d) with OH terminations in configuration III (side view), (e) with OH terminations in configuration I (top view), and (f) with OH terminations in configuration II (top view). Reprinted by permission from Elsevier (Ref.[95]), Computational and Theoretical Chemistry, Copyright 2012.*

Before discussing the change in the MXene properties upon changing the surface terminations, it is important to show the differences in the electronic structure between the MAX and MXene and what the effect of removal of the A element from the crystal lattice on the electron density of states (DOS) is.

In general, DFT calculations predict that MXene monolayers with no surface terminations are metallic and their DOS near the Fermi level, E_f, is higher than that of their parent MAX phases [39,90-94]. Taking Ti_2CT_x as an example, the valence states below the E_f are divided into two sub-bands; one of them **Figure 8**, which is the nearest to E_f, is mainly composed of a hybridization between Ti 3d and Al 3p orbitals; this sub-band *is* called sub-band *A*. the other sub-band, B, is located further from E_f between -10 and -3 eV and is formed from the hybridization between Ti 3d and C 2p orbitals. In MXenes, the removal of the A element leads to the reformation of sub-band A due to the removal of Al 3p orbitals. Sub-band A is composed of only Ti 3d orbitals. The resulting Ti-Ti bonds in turn increase in the electron DOS near the E_f of Ti_2C compared to Ti_2AlC_2 [56].

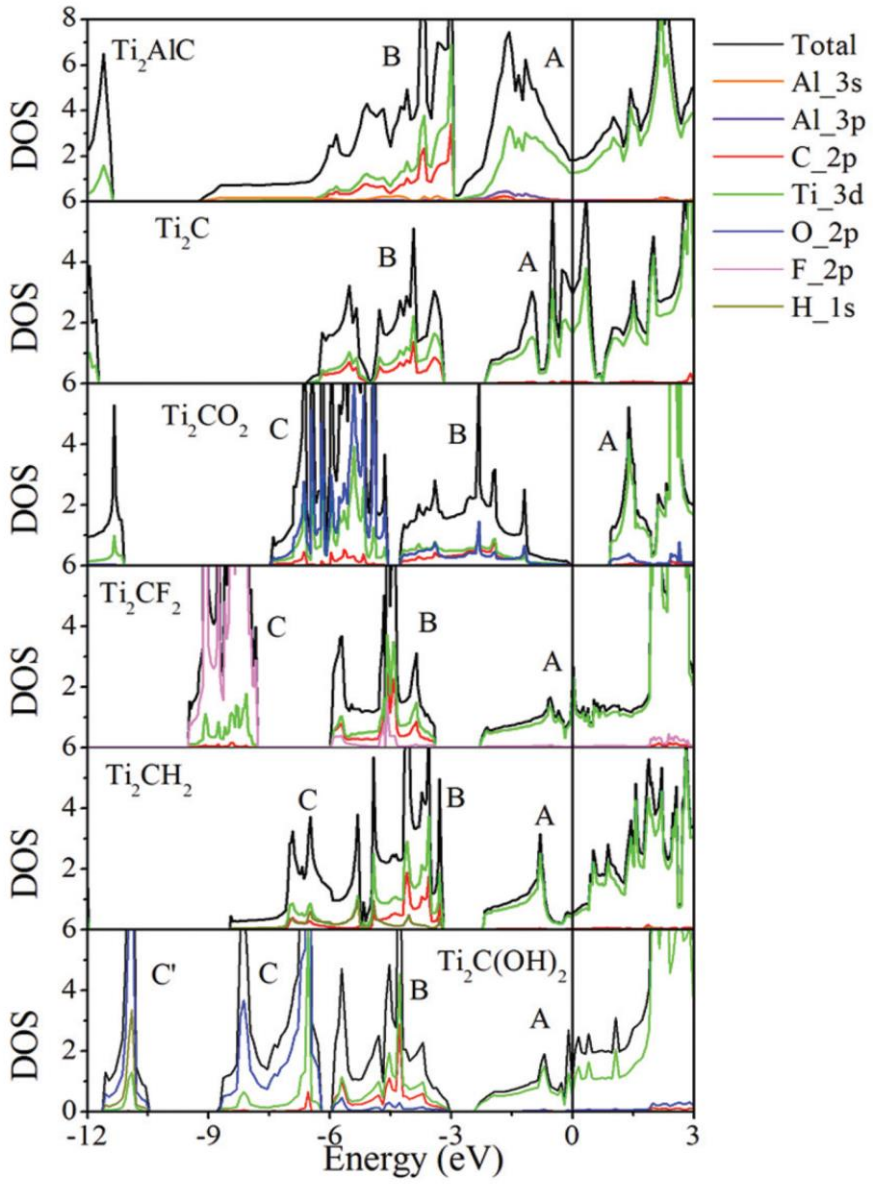

Figure 8. *Partial and total DOS for Ti_2AlC and Ti_2CT_x, where T is either O, F, H or OH and x is 2. Reprinted by permission from American Physical Society, Physical Review B (Ref.[56]), copyright 2013.*

According to DFT calculations, surface terminations can vary the electronic properties of MXenes from being semiconductors with a small band gap to a large direct or indirect band gap as shown in **Table 1**. The reason behind the changes in the band gap is manifested in how the electron DOS near the E_f changes when MXenes are terminated as shown in **Figure 8**. Surface termination groups result in the formation of

a third sub-band, C, located below sub-band B. The former is formed due to M-T bonding moving the gap between sub-bands A and B to lower energies.

Khazaei *et al.* [54] have predicted, through DFT calculations, that MXenes with *n* higher than 1 such as Ti_3C_2, and Nb_4C_3 remain metallic irrespective of the functionalized group whether it is -O, -OH or -F. Furthermore, in the same study, it was shown that the electronic structures of isolated single flakes and multilayered MXenes have no apparent differences in their electronic structure near the fermi level.

Changing T can also affect other properties such as the elastic and optical properties, and also the performance of MXenes in certain applications. For instance, Bai *et al*. [96] showed through DFT calculations that the elastic stiffness and optical response show a strong dependence on T in Ti_2CT_x and $Ti_3C_2T_x$. Ti_2CO_2 and $Ti_3C_2O_2$ were predicted to have the highest elastic constants compared to the -F and -OH terminated Ti_2CT_x and $Ti_3C_2T_x$. Interestingly, Ti_2CF_2 and $Ti_2C(OH)_2$ are predicted to exhibit a white color when subject to light, i.e. none transparent (opaque), while Ti_2CO_2 is predicted to have a high optical transmittance and an optical bandgap originating from its semiconductor-like electronic structure. This makes Ti_2CO_2 a potential candidate for optoelectronic devices.

Table 1. *Band gap values calculated theoretically for select MXenes with different surface terminations.*

Compound	Band gap, eV	Ref.
Ti_2CO_2	1.03*	[92]
Mo_2CF_2	0.25	[55]
$Mo_2C(OH)_2$	0.1	[55]

*indirect band gap. **directed band gap

Eames *et al.* [70] have shown through DFT calculations how the nature of the surface termination group can significantly affect the capacity of a MXene when used

as an electrode for Lithium ion batteries. Oxygen-terminated MXenes were predicted to show the highest capacity compared to the hydroxyl- and F-terminated MXenes.

As stated above, MXenes contain mixed surface termination groups of -O, -OH and -F. So far most of the theoretical calculation studies focused on studying fully terminated MXenes with only one surface termination group either -O -OH or -F. However, most recently theoreticians came up with models to accommodate more two surface termination groups. For example, Babak *et al.* [97] have predicted that -OH and -F and terminated Mo_2TiC_2 and $Mo_2Ti_2C_3$ MXenes should be semiconductors with a small band gap of ≈ 0.05 eV, while also mixing -OH and -F terminations should show a semiconducting behavior. In contrast, -O terminated Mo_2TiC_2 and $Mo_2Ti_2C_3$ MXenes should show metallic behavior. While a mixed termination of -O and -F should show metallic behavior at high -O amounts. It is worth noting that these results are only valid when considering spin-polarized DFT calculations otherwise for non-spin-polarized simulations all the Mo-Ti MXenes regardless of their terminations were predicted to be metallic. Experimental results for both $Mo_2TiC_2T_x$ and $Mo_2Ti_2C_3T_x$ MXenes show a decrease in resistivity with an increase in temperature indicating a semiconducting-like behavior. However, an Arrhenius model does not fit the results indicating that the evidence for a band gap is weak.

Despite the body of literature regarding theoretical studies of the surface terminations of MXenes, there have been few experimental reports of the same. Prior to the initiation of the current study, several trials were made to identify the surface termination groups. One of the first was the use of X-ray diffraction (XRD) patterns of $Ti_3C_2T_x$ etched with HF to compare to theoretical XRD patterns generated from DFT calculations for $Ti_3C_2F_2$ and $Ti_3C_2(OH)_2$ as shown in **Figure 9**.

The simulated XRD pattern of $Ti_3C_2(OH)_2$ appeared to be closest to the experimental pattern; however, there is not enough evidence that OH is the only termination since the elemental analysis performed in the same study showed the presence of F. Furthermore, there was no information about the bonding between the MXene surfaces and the surface termination groups.

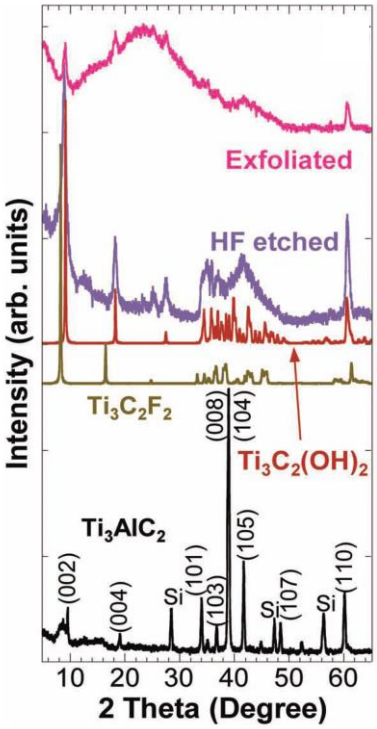

***Figure 9**. XRD patterns for Ti_3AlC_2 before and after HF treatment, $Ti_3C_2T_x$ after sonication in water and simulated XRD patterns of $Ti_3C_2F_2$ and $Ti_3C_2(OH)_2$. Reprinted by permission from John Wiley and Sons, Advanced Materials (Ref.[39]), copyright 2011.*

A few XPS characterization studies were reported, before the start of this study, for only a $Ti_3C_2T_x$-HF etched MXene [39] and a $Ti_3C_2T_x$-HF etched intercalated with hydrazine monohydrate and dimethylformamide [64]. In the first study, only the XPS spectra of the Ti 2p region for $Ti_3C_2T_x$ was shown in comparison with that of Ti_3AlC_2, while in the second, XPS spectra of Ti 2p, O1s, and N1s were shown to confirm the existence of a N-containing species belonging to the intercalated compounds to confirm their intercalation.

Other techniques including transmission electron microscopy (TEM) [51,98], X-ray absorption spectroscopy (XAS) [99], X-ray atomic pair distribution function (PDF) analysis [86,97,100], and multilevel structural modeling of atomic PDF obtained by high-quality neutron scattering [101], were used to investigate the structure and chemistry of MXenes and the nature of their surface terminations. Combining high resolution TEM and STEM with EDX [50] or EELS [94], showed that the surface terminations of -O and -F were randomly distributed between the $Ti_3C_2T_x$ layers and on the surface of single $Ti_3C_2T_x$ sheets. However it was not possible to differentiate between -O and -OH terminations due to the insensitivity of both EDX and EELS to hydrogen.

Lukatskaya *et al.* [99] reported a change in the oxidation state in $Ti_3C_2T_x$ from 2.33 to 2.43 when cycled in an electrochemical cell in 1M H_2SO_4 electrolyte between potentials of -0.35 and 0.35 V, respectively. This result is essential, not only because it is the first to determine the average oxidation state of Ti in $Ti_3C_2T_x$ but also shows that Ti in $Ti_3C_2T_x$ is closer in chemical nature to TiO (oxidation state +2) rather than to TiO_2 (oxidation state +4). This point is discussed in more details in Chapter 4.

Several studies of X-ray atomic PDF analysis for several MXenes were reported [86,100]. Shi *et al.* [100] studied the structures of pristine, potassium hydroxide and sodium acetate intercalated $Ti_3C_2T_,$ while Ghidiu *et al.* [86] studied the structure of $Nb_4C_3T_x$ and Anasori *et al.* [98] investigated the structure of delaminated $Mo_2TiC_2T_x$ and $Mo_2Ti_2C_3T_x$. However since X-rays are insensitive towards hydrogen, again this technique was not able to differentiate between -O and -OH. To solve this issue Wang *et al.* [99] used high-quality neutron scattering technique to detect both H and F in $Ti_3C_2T_x$, and through multilevel structural modeling of atomic PDF quantification of -O, -OH and -F terminations was possible. However, this technique is incapable of

differentiation between hydroxyl groups that form water and hydroxyl groups that act as surface terminations so differentiation between adsorbed water and -OH terminations was not possible. In addition, this technique provides an indirect method for the quantification of the chemical species based on the modeling of the bond length between various atoms. Therefore, XPS technique is needed since it is one of the few techniques that can differentiate between different chemical species and directly quantify elemental and chemical species near the surface. Thus, the goal of this work was to study the chemistry of this new family of 2D transition metal carbides and carbonitrides (MXenes) by identifying and quantifying the surface termination groups found in these materials using X-ray photoelectron spectroscopy (XPS).

2.3 XPS analysis of water on metal oxides and metal carbides

When synthesized in aqueous media interactions with water are unavoidable, and therefore MXene surfaces tend to behave like transition metal oxides surfaces since also are terminated in -O and –OH; their core, however, tends to be have more like transition metal carbides. Therefore, using XPS studies of the interaction of water with metal oxides and metal carbides as models and references for the chemical species in MXenes seems a reasonable approach. In this section, several XPS studies of metal carbides and oxides and their interaction with water are discussed with a special focus on titanium oxides.

The interaction of water with TiO_2 in UHV has been studied extensively [102-105]. Several studies investigated, using XPS, the various oxygen chemical species created upon the interaction of water with TiO_2 and assigned and identified the binding energy for each chemical species present [106,107]. Among these species, found in the XPS spectra for O 1s region, are: i) lattice oxygen in TiO_2 at BE of 530.5 eV, **Figure**

10.**a**, ii) O atoms next to vacanct sites at BE of 531.5 eV, **Figure 10**.**a**, iii) OH group at bridging sites at BE of ≈ 531.8 eV **Figure 10**.**a** and **b**, and iv) adsorbed water at BE of ≈ 533.5 eV, **Figure 10.b** [105].

The defectiveness of the TiO_2 (110) surface affects the dissociation of water on its surface in UHV. Defect-free TiO_2 surfaces were shown not to dissociate water [102,103]. However, oxygen vacancies play an important role in water dissociation on TiO (110) surfaces [108-110]. Yamamoto *et al*. [105], suggested a mechanism for water adsorption on the TiO_2 (110) surface from in-situ hydration and annealing of single crystal TiO_2 (110) surfaces. Initially, water molecules dissociate at O-vacancies in bridge sites, producing a stoichiometric amount of OH bridge groups equal to twice the initial vacancy concentration. Then the OH_{bridge} groups act as nucleation sites that attract water molecules to form strongly bound OH-H_2O complexes that then act as nucleation centers for further water adsorption.

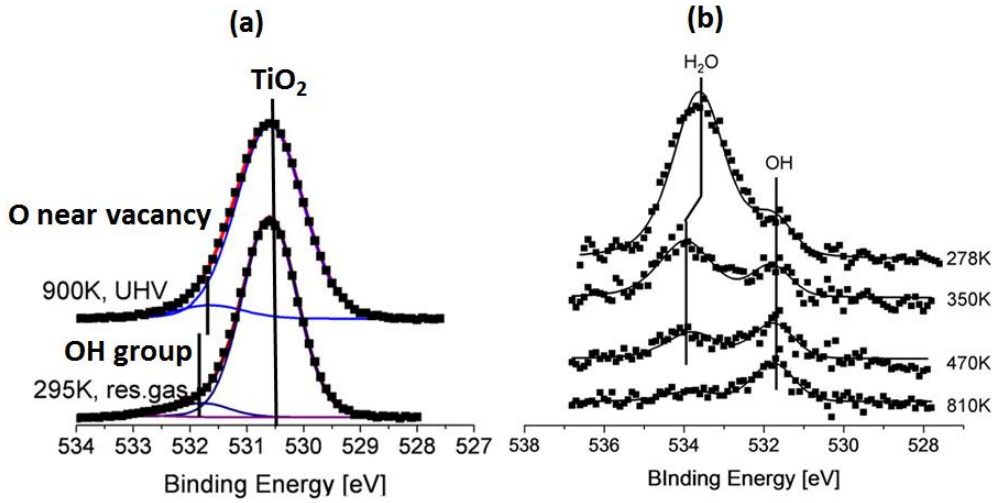

Figure 10. *O 1s XPS spectra of TiO_2 (110): (a) measured at 900 K in vacuum (top curve) and measured after cooling down to 295 K in a residual gas atmosphere (mainly water) of 10^{-8} Torr (bottom curve) and, (b) measured at sample temperatures of 810, 470, 350, and 278 K in the presence of 0.4 Torr water vapor. The dots are the experimental data, solid curves are the fitted curves, and the vertical solid straight lines represent different chemical species (Ref. [105]).*

Similar studies were performed to study the interaction of water with metal carbides surfaces such as TiC and VC [111-113]. According to Didziulis et al.[113], the adsorption of H_2O (D_2O) on TiC (100) surface at 158 K leads to the formation of several species detected by HREELS which are: OH species from decomposed water, and a surface hydride species at low exposure of H_2O (0.1 L). At moderate exposure (0.5 L), the amounts of OH and surface hydride species increase and a surface water species was observed. XPS analysis of the O 1s spectra region for TiC (100) surface after the adsorption of approximately one monolayer of water at 133 K showed three peaks at BE of 533.5, 531.7 and 530.6 eV belonging to the following species: i) molecular water, ii) hydroxyl and iii) chemisorbed oxygen of peak area percentages of 60, 30 and 10 %, respectively. The C atoms in TiC were found to interact with the water molecules forming C-H species on TiC (100), leaving behind a hydroxyl group which tended to migrate to an electron rich C forming CO or CO_2 gas which were observed as desorption products using Temperature Programmed Desorption (TPD).

In the case of VC (100) surfaces, the C-H species is absent and a multi-coordinated hydride species was identified by HREELS but there is no knowledge regarding its actual location on the surface. This hydride species would leave out as a hydroxyl group that would seek out an electron rich site, similar to the TiC case. But in this case, due to the availability of the d-electrons on VC, this could cause the hydroxyl group to remain on the V site instead of reacting with C forming CO and CO_2. This was confirmed by TPD as no peaks related to CO or CO_2 were observed.

The assigned species for the various peaks in the discussed work has been used to identify the various chemical species in MXenes in this study. Since MXenes can be considered as metal carbides with oxide-like surface.

CHAPTER 3: MATERIALS AND METHODS

This chapter provides detailed information on the synthesis of the MXenes multiplayers, ML, and cation intercalation into the same. Experimental details on the XPS characterization techniques and detailed information on the peak fitting procedures of the XPS spectra are discussed.

3.1 MXene synthesis

The MXenes studied herein are in the form of multilayered, ML, powders compressed into discs. The MXenes studied are: $Ti_3C_2T_x$, Ti_2CT_x, Ti_3CNT_x, Nb_2CT_x, $Nb_4C_3T_x$, V_2CT_x, Mo_2CT_x, $Mo_2TiC_2T_x$ and $Mo_2Ti_2C_3T_x$.

3.1.1 Synthesis of the MAX phases

This section provides the experimental details regarding the synthesis of the MAX phases used to produce the MXenes studied in this study.

Synthesis of Ti_3AlC_2

Ti_3AlC_2 powders was prepared by mixing commercial Ti_2AlC powders (Kanthal, Sweden, -325 mesh) with TiC (Alfa Aesar, Ward Hill, USA, 99.5 wt.% purity, -325 mesh) in a 1:1 molar ratio, respectively, (after adjusting for the ~ 12 wt.% Ti_3AlC_2 already present in the commercial powder), followed by ball milling for 18 h to ensure mixing of the powders. The mixture was then heated in a tube furnace to 1350 °C with a rate of 10 °C min^{-1} for 2 h under flowing argon (Ar). The resulting material was in the form of a lightly sintered brick that was ground using a TiN-coated milling bit and sieved through a 400 mesh sieve, producing Ti_3AlC_2 powder with particle size less than 38 µm.

Synthesis of Ti_2AlC

Ti_2AlC powders were prepared by mixing elemental powders of Ti (Alfa Aesar, Ward Hill, USA, 99.5 wt.% purity, -325 mesh) Al (Alfa Aesar, Ward Hill, USA, 99.5 wt% purity, -325 mesh) and graphite (Alfa Aesar, Ward Hill, USA, 99 wt.% purity, -300 mesh) in a molar ratio of 2:1.1:1, respectively. The mixture was ball milled for 18 h then heated at a rate of 10 °C min^{-1} in a tube furnace to 1400 °C for 4 h in Ar atmosphere. After cooling to room temperature, the lightly sintered Ti_2AlC product was processed as described above for the lightly sintered Ti_3AlC_2 brick.

Synthesis of Ti_3AlCN

Ti_3AlCN powders were prepared by mixing powders of Ti, AlN (Sigma Aldrich, St. Louis, USA, 99 wt.% purity, particle size < 10 μm) and graphite, as described above, in a molar ratio of 3:1:1. The mixture was ball milled for 18 h then heated at a rate of 10 °C min^{-1} in a tube furnace to 1500 °C for 2 h in Ar atmosphere. After cooling to room temperature, the lightly sintered Ti_3AlCN product was processed as described for the lightly sintered Ti_3AlC_2 brick.

Synthesis of Nb_2AlC

Nb_2AlC powders were prepared by mixing powders of Nb (Atlantic Equipment Engineers, Bergenfield, USA, 99.8 wt.% purity, -325 mesh), Al, and graphite in a molar ratio of 2:1.1:1, respectively. The mixture was ball milled for 18 h then heated at a rate of 5 °C min^{-1} in a tube furnace at 1600 °C for 4 h in Ar atmosphere. After cooling to room temperature, the lightly sintered Nb_2AlC product was processed as described for the lightly sintered Ti_3AlC_2 brick.

Synthesis of Nb_4AlC_3

Nb_4AlC_3 powders were provided by Dr. Jian Yang, Nanjing Tech University, China. They were prepared by *in situ* hot pressing of commercially available powders of Nb (Beijing Xinrongyuan Science and Tech. Co., Ltd, China, 99.5 wt.% purity, ≤ 94

μm), Al (General Research Institute for Nonferrous Metals, Beijing, China, 99.9 wt.% purity, ≤ 74 μm), and graphite (Qingdao Tianhe Graphite Co., Ltd, China, 99 wt.% purity, ≤ 94 μm). The elemental powders were mixed in a molar ratio of Nb:Al:C of 4:1.1:2.7 by ball milling for 24 h in a polyethylene jar filled with Ar. The mixed powders were placed in a graphite die that was pre-sprayed with a layer of BN and compacted with a load corresponding to a stress of 3 MPa. The compacted body was then heated at a rate of 20 °C min^{-1} up to 1700 °C and held for 1 h under a load corresponding to a pressure of 30 MPa in Ar atmosphere, then cooled to room temperature. The resulting Nb_4AlC_3 billet was crushed into fine powder using a crusher (QE-100 pulveriser, Yili Tools Co., China) followed by sieving through a 400-mesh sieve producing powders with particle size less than 38 μm.

Synthesis of V_2AlC

V_2AlC powders were produced by mixing powders of V (Alfa Aesar, Ward Hill, USA, 99 wt.% purity, -325 mesh), Al and graphite in a molar ratio of 2:1.3:1, respectively. The mixture was ball milled for 18 h then heated at a rate of 5 °C min^{-1} in a tube furnace at 1500 °C for 4 h in Ar atmosphere. After cooling to room temperature, the lightly sintered V_2AlC product was processed as described for the lightly sintered Ti_3AlC_2 brick.

Synthesis of Mo_2TiAlC_2 and $Mo_2Ti_2AlC_3$

Elemental powders of Mo (Alfa Aesar, Ward Hill, USA, 99.5 wt.% purity, -20 mesh, Ti, Al and graphite were mixed in the molar ratios of 2.2Mo:0.8Ti:1.1Al:2C, and 2Mo:2Ti:1.1Al:2.7C to produce Mo_2TiAlC_2 and $Mo_2Ti_2AlC_3$, respectively. In both cases, the powders were ball milled for 18 h then heated at a rate of 5 °C min^{-1} in a tube furnace at 1600 °C for 4 h in Ar atmosphere. After cooling to room temperature, the

lightly sintered Mo_2TiAlC_2 and $Mo_2Ti_2AlC_3$ products were processed as described for the lightly sintered Ti_3AlC_2 brick.

Synthesis of Mo_2Ga_2C

Mo_2Ga_2C powders were produced by a solid-liquid reaction of Mo_2C and Ga. Mo_2C powders (Alfa Aeser, Ward Hill, USA, 99.5 wt.% purity, -300 mesh) and elemental Ga (Alfa Aesar, Ward Hill, 99.5 wt.% purity) were mixed in a molar ratio of 1:8 and placed in a quartz tube that was evacuated using a mechanical pump and sealed. The quartz tube was placed in a horizontal tube furnace that was heated at a rate of 10 °C min^{-1} to 850 °C and held at that temperature for 48 h. After furnace cooling, the lightly sintered material was crushed, using mortar and pestle, and returned back to the quartz tube. The latter was evacuated, and re-heated at the same rate as previously done and held at 850 °C for another 16 h.

After cooling, the product of the lightly sintered Mo_2Ga_2C and the excess, unreacted Ga were added to a solution of 12 M HCl (Fisher Scientific, Fair Lawn, NJ, USA, technical grade) of a ratio of 1 gm to 20 ml for 2 d at room temperature, while being stirred using a Teflon coated magnet on a stir plate. This was done to dissolve the excess Ga. The powders were then washed with deionized (DI) water of a ratio 1 gm to 20 ml several times until a pH of ~ 6 was reached. The wet washed powder was then dried by filtration using a nanoporous polypropylene (3501 Coated P, 0.064 µm pore size, Celgard, USA). The dried powder was then sieved through a 400 mesh sieve producing Mo_2Ga_2C powders with particle size < 38 µm.

3.1.2 Synthesis of multilayered MXene (HF method)

As discussed above, MXenes are synthetized by selective etching of the "A" layers from their corresponding MAX phase. The MAX phases powders, with particle size less than 38 µm, were treated with aqueous HF solution (Fisher Scientific, Fair

Lawn, NJ) of ratio 1 gm of MAX to 10 ml of HF, except for Mo_2Ga_2C a volume of 20 mL of HF was used. The exact conditions used for producing each ML-MXene compound are shown in **Table 2**. The resulting suspensions were washed with DI water and separated from the remaining HF by centrifuging until the pH of the liquid reached a pH of about 5 to 6.

Table 2. *HF etching conditions of MAX phases to produce their corresponding MXenes.*

Sample name	MAX phase	MXene produced	HF concentration (wt. %)	Etching duration (h)	Temp. (°C)
$Ti_3C_2T_x$-50HF	Ti_3AlC_2	$Ti_3C_2T_x$	50	18	RT
$Ti_3C_2T_x$-10HF	Ti_3AlC_2	$Ti_3C_2T_x$	10	24	25
Ti_2CT_x-10HF	Ti_2AlC	Ti_2CT_x	10	10	RT
Ti_3CN-30HF	Ti_3AlCN	Ti_3CNT_x	30	18	RT
Nb_2CT_x-50HF	Nb_2AlC	Nb_2CT_x	50	48	55
$Nb_4C_3T_x$-50HF	Nb_4AlC_3	$Nb_4C_3T_x$	50	96	55
V_2CT_x-50HF	V_2AlC	V_2CT_x	50	48	55
Mo_2CT_x-25HF	Mo_2Ga_2C	Mo_2CT_x	25	159	55
$Mo_2TiC_2T_x$-50HF	Mo_2TiAlC_2	$Mo_2TiC_2T_x$	50	72	55
$Mo_2Ti_2C_3T_x$-50HF	$Mo_2Ti_2AlC_3$	$Mo_2Ti_2C_3T_x$	50	96	55

In order to separate the MXene from any un-etched MAX powder, the wet sediment was re-dispersed in 40 ml of DI water and centrifuged at 300 rpm for 5 min. The supernatant was filtered using a nanoporous polypropylene membrane (3501 Coated P, 0.064 µm pore size, Celgard, USA). The powder was collected and processed for the XPS measurements.

3.1.3 Synthesis of ML-$Ti_3C_2T_x$ MXene (LiCl+HF method)

One gram of Ti_3AlC_2 powders, of particle size < 38 µm, was slowly added to a premixed 10 mL mixture of 10 wt.% aqueous HF and LiCl solution containing 1.1 gms

of LiCl. The molar LiCl to Ti_3AlC_2 ratio was 5:1. The reaction mixture was stirred for 24 h at 25 °C, after which the powders were washed 3 times with 6 M HCl, in a ratio of 0.5 g powders to 40 mL HCl. This step was performed to remove any traces of LiF that may have precipitated during etching. The powders were then immersed in 1 M LiCl (Alfa Aeser, Ward Hill, USA, 99.0 wt.% purity) for 24 h to ensure that Li remained in the structure. Afterwards the mixture was washed with 40 mL of DI water for 3 times and dried by filtration as previously described. The produced powder is henceforth denoted as Li-$Ti_3C_2T_x$-HF/LiCl.

3.1.4 Synthesis of ML-$Ti_3C_2T_x$ MXene (LiF+HCl method)

One gram of Ti_3AlC_2 powders, of particle size < 38 µm, were slowly added to a mixture of 10 mL of a premixed solution of 1.2 gms of LiF (Alfa Aesar, Ward Hill, USA, 90 wt.% purity) and 12 M HCl. The mixture was stirred for 24 h at 35 °C. Afterwards HCl washing was performed as described previously to remove any LiF leftover. This was followed by 3 cycles of 1 M of aqueous LiCl washings. Finally, the mixture was washed with DI water for 3 times each time 40 mL were used and dried by filtration as previously described. The produced powder is henceforth denoted as Li-$Ti_3C_2T_x$-HCl/LiF.

3.1.5 Cation exchange of Li-$Ti_3C_2T_x$-HF/LiCl

Powders of Li-$Ti_3C_2T_x$-HF/LiCl were HCl pre-washed, as described above, while they are still in a wet state. Salt solutions of 1 M NaCl or RbCl (Alfa Aesar, Ward Hill, USA, 90 wt.% purity) in DI water were added in a ratio of 0.5 g Li-$Ti_3C_2T_x$-HF/LiCl to 40 mL solution. After shaking for 2 min, the mixtures were allowed to sit for 1 h, then the solution was washed by the centrifugation method, decanted and a fresh solution was added was replaced by a fresh one using the centrifugation method.

The samples were again shaken and allowed to sit for 24 h followed by washing with 5 mL of DI water twice. Finally, the samples were dried by filtration as previously described. The produced powder resulting from the NaCl and RbCl treatments are henceforth denoted as Na-$Ti_3C_2T_x$-HCl/LiF and Rb-$Ti_3C_2T_x$-HCl/LiF, respectively.

3.1.6 Alkali treatments of $Ti_3C_2T_x$-50HF

Solutions of 25 wt.% NaOH or KOH (Sigma Aldrich, St. Louise, USA, 99 wt.% purity) were added to a $Ti_3C_2T_x$-50HF powder in the ratio of 10 mL of solution to 0.5 gm of powders. The powder used was filter dried, allowed to sit on the filter for 10 min after all the visible water was filtered. The mixtures were allowed to settle for 24 h before being washed with DI 5 times, each time with 40 mL of DI water followed by filtration drying as described previously. The produced powder resulting from the NaOH and KOH treatments will henceforth be denoted as Na-$Ti_3C_2T_x$-50HF and Rb-$Ti_3C_2T_x$-50HF, respectively.

3.1.7 Sample preparation for XPS measurements

Since XPS is a surface sensitive technique, extreme care must be taken when preparing the samples for the measurements. Most of sample for XPS measurements were prepared within < 0.5 h after the powders were filter dried. The powders were collected from the filter and cold pressed in a steel die, using a load corresponding to a stress of 1 GPa, to produce free-standing discs. To confirm that the cold-pressing of samples did not contaminate the XPS results, we compared survey spectra of these samples with powdered samples that were not cold pressed and saw no difference in the spectra, this is shown in Ref. [114].

The advantages of using cold pressed samples is that they provided a smooth surface allowing for more accurate results. The cold pressed discs were mounted on the sample holder *via* double sided tape and grounded using a copper wire.

3.2 XPS characterization

3.2.1 Basic principle of XPS technique

XPS is a surface technique used for compositional and chemical state analysis of the surfaces of materials [115]. XPS spectra are obtained by bombarding the surface of the sample with X-ray photons of a specific energy which excites the core level electrons of the various elements found in that sample as shown in **Figure 11**.

Since these core level electrons are quantized, they can be detected by the hemispherical analyser (HSA) that is adjusted to a certain voltage, V, to allow the passage of core electrons of a given kinetic energy belonging to a given element as shown in **Figure 12**. This kinetic energy is converted to a binding energy (BE) using the following equation [115]:

$$BE = h\nu - KE - \Phi \qquad (4)$$

where hν is the energy of the X-ray photon and Φ is the work function of the spectrometer.

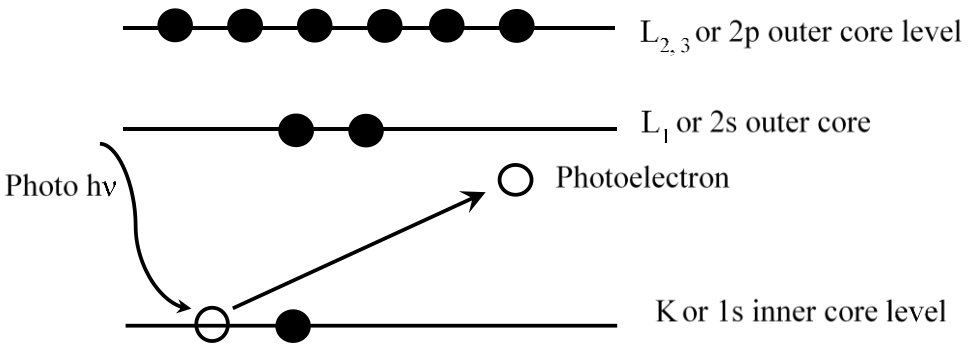

Figure 11. *Schematic showing the basic principle of the XPS.*

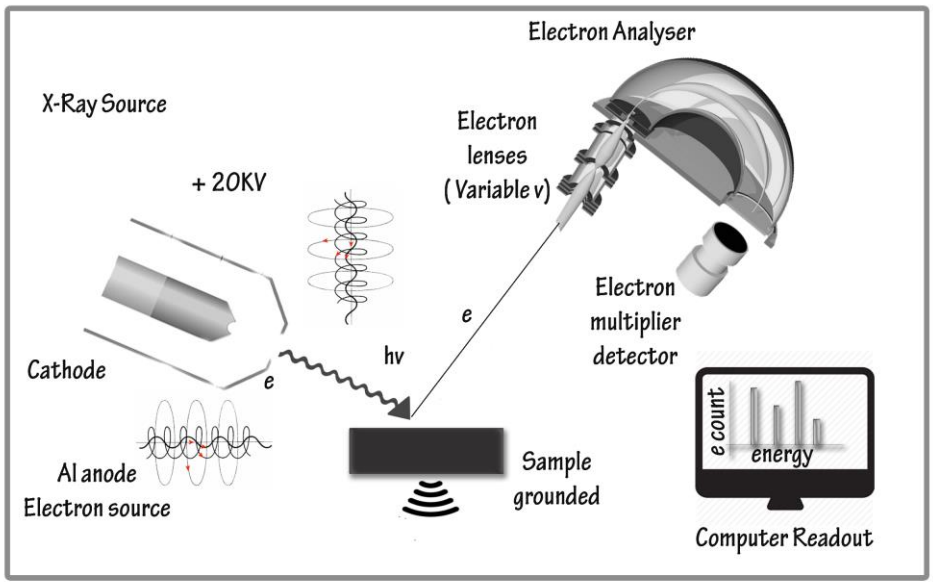

Figure 12. *Schematic showing the different parts of the XPS machine*

The HSA also counts the number of these core level electrons which is reflected in the intensity of the photoelectron peaks at a specific BE. Only the electrons that preserve their kinetic energy contribute to the XPS spectra peaks. These are mostly electrons ejected only from the sample's surface since electrons buried deeper in the sample suffer from inelastic scattering that results in a reduction of their kinetic energy before they reach the detector. For this reason, XPS analysis is typically limited to measuring depths of 8 to 10 nm.

3.2.2 Details of the XPS machine used in this study

Samples were analyzed using a Physical Electronics VersaProbe 5000 instrument shown in **Figure 13**. A 100 µm monochromatic Al-Kα X-ray beam irradiated the sample surface. Photoelectrons were collected by a 180° hemispherical electron energy analyzer. Samples were analyzed at a 45° takeoff angle between the sample surface and the path to the analyzer. The charge was neutralized using a dual beam charge neutralizer irradiating low-energy electrons and ion beams to avoid shifts in the recorded BE. High-resolution spectra for F 1s, O 1s, C 1s, Na 1s, Al 2p, Ti 2p,

Cl 2p, Ga 2p, K 2p, Nb 3d, Mo 3d, and Rb 3d regions were taken at a pass energy of 23.5 eV with a step size of 0.05 eV with time per step of 300 ms for 10 repeats. While high-resolution spectra for Li 1s region was taken at a pass energy of 11.7 eV with the same step size and time per step for 15 repeats.

In some instances, the samples were sputtered before testing. The sputtering was carried out with an Ar beam operating at 3.8 kV at a current of 150 µA for 0.5 h. The BE scale of all XPS spectra was referenced to the Fermi-edge (E_f), which was set to a BE of zero eV.

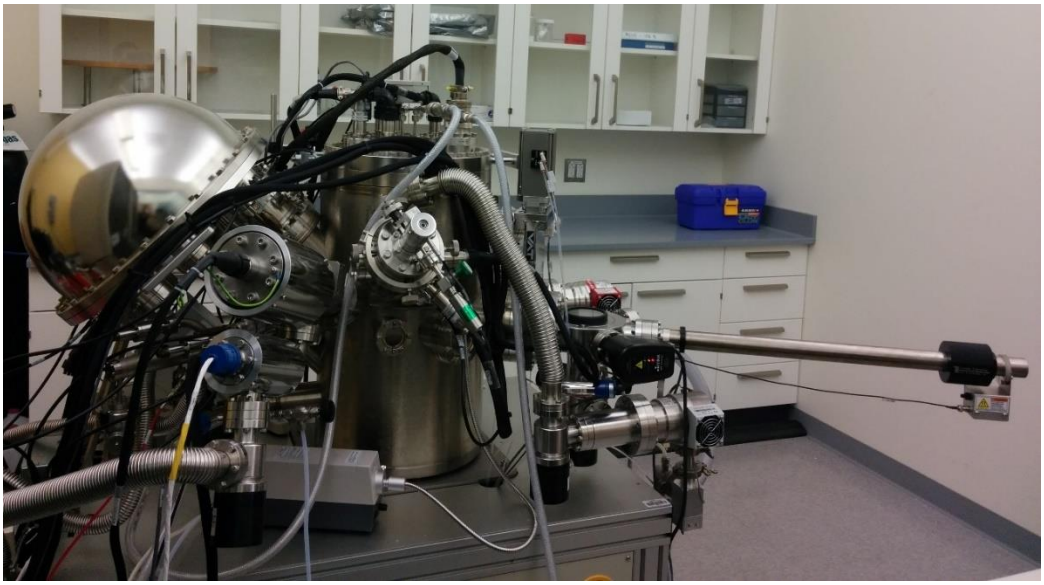

Figure 13. *Picture of Physical Electronics VersaProbe 5000 XPS machine.*

3.2.3 Elemental quantification

The global atomic percentage of the various elements was calculated using the following equation:

$$X_i = 100 \frac{A_i}{\sum_{j=1}^{m} A_j} \quad (5)$$

where X_i is the atomic concentration of the element (i),

A_i is the adjusted intensity of element (i),

and A_j is the total adjusted intensity of all elements.

The adjusted intensity is defined as follows:

$$A_i = \frac{I_i}{R_i} \quad (6)$$

where I_i is the integrated peak area obtained from the high-resolution spectra and, R_i is the relative sensitivity factor for each element.

The relative sensitivity factor (R) in most cases is expressed with F 1s or C 1s as unity, and it can be calculated from the following equation [116]:

$$R = \sigma\phi AT\lambda \quad (7)$$

Where: σ is photoelectric cross-section for the particular transition in cm^2 per atom,

ϕ is the angular efficiency factor for the instrumental arrangement (angle between photon path and emitted photoelectron that is detected),

A is the area of the sample from which photoelectrons can be detected

T is the efficiency of detection of the photoelectrons emerging from the sample

λ is the mean free path of the photoelectrons in the sample.

Practically, the relative sensitivity factors are obtained from measuring the XPS spectra of stoichiometric compounds containing the element having an R of unity. For example, to measure R for Li, taking F 1 as the element with R = 1, the high-resolution Li 1s region and F 1s region XPS spectra are measured. The ratio of the area of the peaks in both regions is calculated and equated to 1, which is the atomic ratio of Li to F in LiF, then the R of Li 1s can be obtained from the following equation:

$$R_{Li\ 1s} = \frac{I_{Li\ 1s}.n_{F\ 1s}.R_{F\ 1s}}{n_{Li\ 1s}.I_{F\ 1s}} \quad (8)$$

where n is the atomic ratio of the element.

The XPS peak area in a region of a certain element depends on the instrument, therefore for each instrument a list of R values exists for that instrument. In this study, I used the sensitivity factors for Physical Electronics VersaProbe 5000 instrument by

the manufacturer, the relative sensitivity factors for all the elements used in this study are tabulated in **Table 3**.

Table 3. *Relative sensitivity factors, R, for all elements used in this study.*

Element	Relative sensitivity factor [R]
Ti 2p	2.077
C 1s	0.314
O 1s	0.733
F 1s	1
Al 2p	0.256
Ga 3d	0.535
Nb 3d	3.127
V 2p	2.184
Mo 3d	3.544
Li 1s	0.028
Rb 3d	1.673
Na 1s	1.102
K 2p	1.552
N 1s	0.499
Cl 2p	3.544

3.2.4 Peak fitting of the XPS spectra

In order to precisely identify and quantify the various species in the XPS spectra region for a certain element, peak fitting must be performed. In this study, peak fitting was performed using CasaXPS Version 2.3.16 RP 1.6 software. Prior to peak fitting, the background contributions were subtracted using a Shirely function.

Peak fitting of the high-resolution XPS spectra was performed with some constrains in order to obtain reasonable and self-consistent curve fitting results. The first constraint was the choice of the lineshape used for fitting the different species. For non-conductive species such as metal oxides, oxyfluorides, hydroxides, and, organic contaminations, a symmetric Gaussian Lorentzian (GL) lineshape given by the following equation [117]:

$$GL\ (m) = GL(x{:}\ e, f, m) = G(x{:}\ e, f, m)L(x{:}\ e, f, m)\mathrm{G} \qquad (9)$$

$$G(x: e, f, m) = \exp\left(-4ln2\left(1 - \frac{m}{100}\right)\left(\frac{x-e}{f}\right)^2\right) \quad (10)$$

$$L(x: e, f, m) = \frac{1}{1+4\frac{m}{100}\left(\frac{x-e}{f}\right)^2} \quad (11)$$

Where *e* is the starting BE,

f is the ending BE,

and *m* is the mixing ratio.

However metallic species tend have an asymmetric lineshape showing an extended tail in the low kinetic energy side of the spectrum, i.e. at high BEs. The extended tail can be explained in terms of the interaction of the photoelectrons with valence band electrons [118]. Therefore, a Lorentzian Asymmetric (LA) lineshape was used to fit species such as metals, most notably the M-X species in MXenes in the M and X XPS regions and carbides assuming the following equation [117]:

$$LA(x: \alpha, \beta, f, e) = \begin{cases} [L(x: f, e, 100)]^{\alpha} & x \leq e \\ [L(x: f, e, 100)]^{\beta} & x > e \end{cases} \quad (12)$$

$$L(x: e, f, 100) = \frac{1}{1+4\frac{100}{100}\left(\frac{x-e}{f}\right)^2} \quad (13)$$

where α and β define the spread of the tail on either side of the Lorentzian component.

The second constraint is related to the spin orbit splitting of core levels higher than the s core level. All orbitals except the s levels (l = 0) give rise to a doublet with the two possible states having different BEs. This is known as spin-orbit splitting (or j-j coupling) [119]. The number of electrons in each of the spin states for a given core level follows the formula: $j = (l \pm s)$, the ratio of the number of electrons in the two split states is equal to the ratio of the area of their corresponding peaks. For example, for the 2p spectra, where n is 2 and l is 1, j will be 3/2 and ½ and the ratio of the number of electrons will be 4:2, therefore the peak area ratio will be 2:1. For the d and f spectra

the area ratios are 3:2 and 4:3, respectively. Also the peak separation is fixed for each chemical species.

The third was to constrain the BE shifts for each component. The BEs were allowed to shift ±0.5 eV from their initial values in steps of 0.02 eV between each curve-fitting iteration.

The forth constraint was to restrict the full width at half maximum (FWHM) of each component. The FWHM is determined by the lifetime of the core-hole and instrumental broadening [117]. Shorter core-hole lifetimes result in broader XPS peaks; instrumental broadening is determined by detector settings and limitations. Often there were peaks that appeared broader than expected. For example, the FWHM of the Ti 2p peaks of the component we labeled TiO_2 is larger than that of pure TiO_2 [120] Such broadening can be ascribed to the presence of defects such as oxygen vacancies, and/or dopants near some Ti atoms and not others. The separation between the various BEs of these Ti atoms, however, was below the resolution of our XPS. It follows that they were fit to only one peak that was broader than that of pure, well crystallized, defect-free TiO_2 [120]. The FWHM of different components that are included in the fit of an XPS spectrum, *e.g.* Ti 2p, can be different, but the same component present in two, or several, samples, e.g. Ti_2CT_x and $Ti_3C_2T_x$, is expected to show small, if any, variations in the FWHM. Additionally, following sputter cleaning, many of the broadened, which can again be due to sputtering induced defects. As a result, the spin-orbit doublets of these peaks was allowed to shift further apart to accommodate the broadening.

The fifth, and last constraint, was that each curve fitting procedure started with a minimum number of components that are well-established. For the Ti-MXenes, the Ti 2p region, the starting components were TiO_2 [105,120,121], $TiO_{2-x}F_x$ [122], as well as, peaks corresponding to Ti of +1, +2 and +3 oxidation states in (OH and/or O)-Ti-C.

For the Nb-MXenes, in the Nb 3d region, the starting components where NbO, Nb^{+4}-O and Nb_2O_5, as well as (OH and/or O)-Nb-C. However, since > 2 eV separated the NbO and NbO_2 peaks these components were insufficient to bridge the gap in $Nb_4C_3T_x$. A peak assumed to be due to a Nb^{+4}-O component was thus added. Peak-fits of all other regions were all performed using the same constraints.

CHAPTER 4: RESULTS AND DISCUSSION

4.1 XPS analysis of various multilayered HF etched MXenes

4.1.1. XPS analysis of multilayered $Ti_3C_2T_x$-50HF

Figures 14-17 plot the spectra for the Ti, C, O and F regions, respectively, for un-sputtered $Ti_3C_2T_x$-50HF multi-layered, ML, cold pressed disk, together with their peak-fits. The peak positions, Full Width Half Maximum (FWHM), and the fraction of each peak obtained from the fits are summarized in **Table 4**. Each region is discussed in detail below.

Ti 2p region

The Ti 2p region for the un-sputtered $Ti_3C_2T_x$-50HF sample (**Figure 14**) was fit by the components listed in column 5 in **Table 4**. The majority of the species are: a Ti atoms bonded to C and surface terminations of O and/or OH: (OH and/or O-Ti-C), and (OH and/or O-Ti^{+2}-C), and (OH and/or O-Ti^{+3}-C) that belong to $Ti_3C_2O_x$, $Ti_3C_2(OH)_x$ and, b) Ti atoms bonded to C and F surface terminations (F-Ti-C), which belongs to $Ti_3C_2F_x$. These comprise 95% of the photoemission in the Ti 2p region. The rest belongs to TiO_2 and $TiO_{2-x}F_x$ species present as a result of surface oxidation. It is worth noting that similar oxidation states for Ti reported here, *viz.* Ti^{2+} and Ti^{3+}, were reported for TiC [123].

The binding energy (BE) for the Ti $2p_{3/2}$ peak of the $Ti_3C_2T_x$ sample ($\approx$ 455 eV), is higher than the 454.6 eV value in the parent MAX phase, Ti_3AlC_2 [124]. This shift is due to the replacement of the Al layers by more electronegative surface terminations such as O, OH and F.

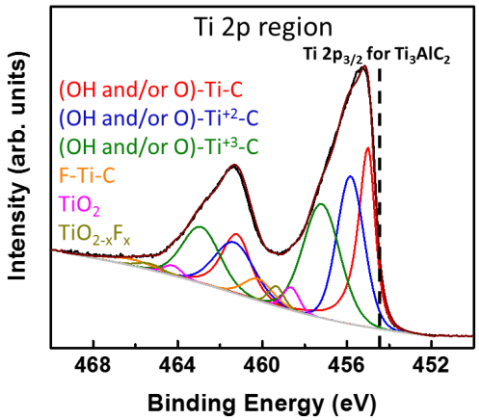

Figure 14. *Component peak fitting of XPS spectra of Ti 2p region for un-sputtered ML $Ti_3C_2T_x$-50HF cold pressed disk. Various peaks shown represent various species assumed to exist. Labels and peak colors are coordinated. The results are summarized in* ***Table 4****. Dashed vertical line denotes the position of the same peak in the parent MAX phase.*

C 1s region

The C 1s region (**Figure 15** and **Table 4**) of the un-sputtered $Ti_3C_2T_x$-50HF sample was fit by three peaks. The largest (≈ 54% of the C 1s region), at a BE of 282.0 eV, corresponds to C-Ti-T_x (where T_x is O, OH and/or F). Its binding energy is slightly higher than that of C in Ti_3AlC_2 (281.5-281.8 eV) [124]. The small shift can possibly be attributed to defects introduced in the Ti-C layers due to the etching procedure.

The other two peaks correspond to graphitic C-C and CH_x or C-O. The former could be due to selective dissolution of Ti during etching, which can result in graphitic C-C formation or could simply be surface contamination [125]. The CH_x, and C-O species, on the other hand, likely result from the solvents used in the separation and drying processes and/or the exposure of the high surface area material to the ambient atmosphere.

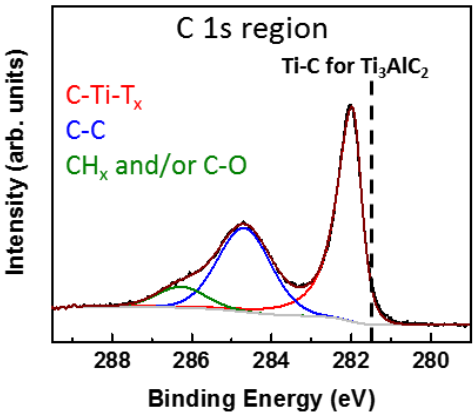

Figure 15. *Component peak fitting of XPS spectra of C 1s region for un-sputtered ML $Ti_3C_2T_x$-50HF cold pressed disk. Various peaks shown represent various species assumed to exist. Labels and peak colors are coordinated. The results are summarized in* ***Table 4****. Dashed vertical line denotes the position of the same peak in the parent MAX phase.*

O 1s region

The O 1s region for this sample (**Figure 16** and **Table 4**) was fit by components corresponding to C-Ti-O, C-Ti-$(OH)_x$ and H_2O_{ads}, represent the majority fraction (53%) of that region. The differences between these species are explained below. The balance is in the form of TiO_2, $TiO_{2-x}F_x$ and Al_2O_3 (Column 5 in **Table 4**). Surface organic contaminations of C-O contribute to this region, and overlap and obscure many other peaks. However, the amount of these organic contaminations in this case is < 2.5 at.%.

The BE of C-Ti-O in this sample is 531.2 eV. This value is close to that of an O atom near to vacant site in TiO_2, *i.e.* a defective TiO_2 (531.5 eV) [105]. The peak for C-Ti-$(OH)_x$ is located at a BE of 532.0 eV, which is quite close to that of OH groups at bridging sites on TiO_2 [105].

The H_2O_{ads} component is that of water species being strongly adsorbed on the surface of MXene. At 533.8 eV, the BE of this species is quite close to that of a water molecule adsorbed to an OH group at bridging sites on titania (533.5 eV) [105]. The $Al(OF)_x$ species, present in the pre-sputtered $Ti_3C_2T_x$ is a by-product of the synthesis procedure.

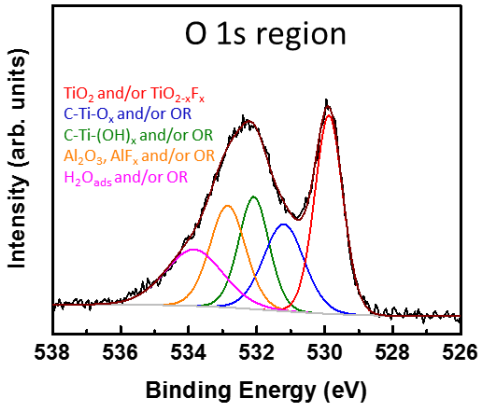

Figure 16. *Component peak fitting of XPS spectra of O 1s region for un-sputtered ML $Ti_3C_2T_x$-50HF cold pressed disk. Various peaks shown represent various species assumed to exist. Labels and peak colors are coordinated. The results are summarized in* ***Table 4****.*

F 1s region

The largest component in the F 1s region (**Figure 17** and **Table 4**) for this sample is C-Ti-F_x, at a BE of 685.0 eV. This BE is 0.1 eV higher than that of TiF_4 [126], a similar compound that should have a value close to that of the Ti-F bond in $Ti_3C_2F_x$.

Smaller fractions of $TiO_{2-x}F_x$, AlF_x and $Al(OF)_x$ are also found in the F 1s region. The first one is due to surface oxidation, while the latter two are byproducts of the synthesis procedure. Their presence was confirmed by high-resolution XPS spectra in the Al 2p region [114].

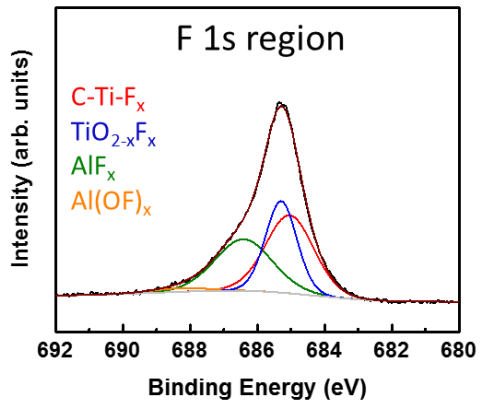

Figure 17. *Component peak fitting of XPS spectra of F 1s region for un-sputtered ML $Ti_3C_2T_x$-50HF cold pressed disk. Various peaks shown represent various species assumed to exist. Labels and peak colors are coordinated. The results are summarized in* ***Table 4****.*

Table 4. *Summary of XPS peak fitting results for un-sputtered ML $Ti_3C_2T_x$-50HF cold pressed disk. The numbers in parenthesis in column 2 for the Ti 2p region are peak locations of* Ti $2p_{1/2}$*; their respective FWHMs are listed in column 3 in parenthesis.*

Region	BE [eV][a]	FWHM [eV][a]	Fraction	Assigned to	Reference
Ti $2p_{3/2}$ ($2p_{1/2}$)	455.0 (461.2)	0.8 (1.5)	0.28	(OH, or O)-Ti-C	[123,124]
	455.8 (461.3)	1.5 (2.2)	0.30	(OH, or O)-Ti^{2+}-C	[123]
	457.2 (462.9)	2.1 (2.1)	0.32	(OH, or O)-Ti^{3+}-C	[123]
	458.6 (464.2)	0.9 (1.0)	0.02	TiO_2	[120,121]
	459.3 (465.3)	0.9 (1.4)	0.03	$TiO_{2-x}F_x$	[122]
	460.2 (466.2)	1.6 (2.7)	0.05	C-Ti-F_x	[126]
C 1s	282.0	0.6	0.54	C-Ti-T_x	[123,124]
	284.7	1.6	0.38	C-C	[127]
	286.3	1.4	0.08	CH_x /C-O	[127]
O 1s	529.9	1.0	0.29	TiO_2	[105,120]
	531.2	1.4	0.18	C-Ti-O_x and/or OR[b]	[105,128]
	532.0	1.1	0.18	C-Ti- $(OH)_x$ and/or OR[b]	[105,128]
	532.8	1.2	0.19	Al_2O_3 and/or OR[b]	[128-130]
	533.8	2.0	0.17	H_2O_{ads} and/or OR[b]	[105,128]
F 1s	685.0	1.7	0.38	C-Ti-F_x	[126]
	685.3	1.1	0.29	$TiO_{2-x}F_x$	[122]
	686.4	2.0	0.30	AlF_x	[122]
	688.3	2.0	0.02	$Al(OF)_x$	[129]

[a] Values in parenthesis correspond to the $2p_{1/2}$ component.
[b] OR stands for organic compounds due to atmospheric surface contaminations.

4.1.2. XPS analysis of multilayered Ti_2CT_x-10HF

Figures 18-21 plot the spectra for Ti, C, O and F regions, respectively, for un-sputtered Ti_2CT_x-10HF, ML, cold pressed disk together with their peak-fits. The peak positions, FWHM, and the fraction of each peak obtained from the fits are summarized in **Table 5**. Each region is discussed in detail below.

Ti 2p region

The Ti 2p region this sample (**Figure 18**), was fit by the same components (listed in **Table 5**) as for the Ti 2p region for the un-sputtered $Ti_3C_2T_x$-50HF sample. The ratio of fractions of the three oxidation states of $Ti:Ti^{+2}:Ti^{+3}$ in Ti_2CT_x is 1:0.5:1.3, respectively, showing that the highest oxidation state has the highest amount. While for $Ti_3C_2T_x$ the ratio is 1:1.1:1.1, indicating that the three oxidation states are almost equal

in amounts. Thus, the average oxidation state of Ti in Ti_2CT_x is higher than $Ti_3C_2T_x$. The reason for this might be the absence of the core Ti-C layer in Ti_2CT_x leaving only Ti-C layers that are bonded to surface terminations. Another interesting difference is the amount of surface oxidation; for Ti_2CT_x the fraction of surface oxidations (TiO_2 and $TiO_{2-x}F_x$) is 0.12 which is higher than for $Ti_3C_2T_x$ at 0.05. Thus, everything else being equal it is reasonable to assume Ti_2CT_x oxidizes more quickly than $Ti_3C_2T_x$, meaning the former is less stable.

The binding energy (BE) for the Ti $2p_{3/2}$ peak of the Ti_2CT_x sample (≈ 454.9 eV), is higher than the 454.7 eV value in the parent MAX phase, Ti_3AlC_2[124]. This shift is due to the replacement of the Al layers by more electronegative surface terminations such as O, OH and F, similar to $Ti_3C_2T_x$, as explained previously.

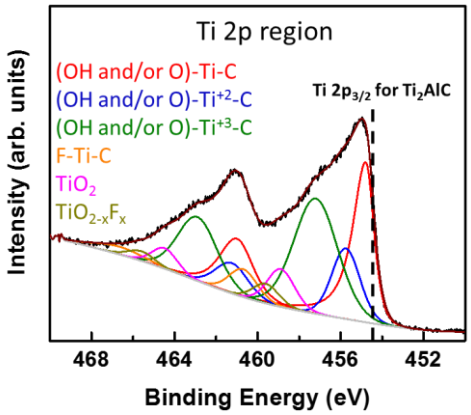

Figure 18. *Component peak fitting of XPS spectra of Ti 2p region for un-sputtered ML Ti_2CT_x-10HF cold pressed disk. Various peaks shown represent various species assumed to exist. Labels and peak colors are coordinated. The results are summarized in* ***Table 5****. Dashed vertical line denotes the position of the same peak in the parent MAX phase.*

C 1s region

Before sputtering, this region (**Figure 19**) was fit by components corresponding to C-Ti-T_x, graphitic carbon (C-C), CH_x, C-O, and a component arising from adsorbed carboxyl groups (COO) (**Table 5**). The most prevalent component, at an atomic fraction of 0.28, corresponds to C-Ti-T_x, at almost the same BE (281.9 eV) as C-Ti-T_x for $Ti_3C_2T_x$ and C-Ti for Ti_2AlC [114].

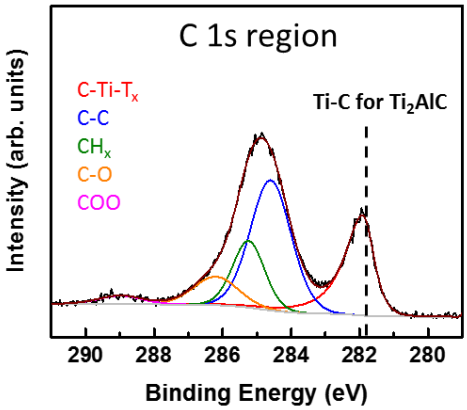

Figure 19. *Component peak fitting of XPS spectra of C 1s region for un-sputtered ML Ti_2CT_x-10HF cold pressed disk. Various peaks shown represent various species assumed to exist. Labels and peak colors are coordinated. The results are summarized in* ***Table 5****. Dashed vertical line denotes the position of the same peak in the parent MAX phase.*

O 1s region

The O 1s region (**Figure 20**) of the pre-sputtered Ti_2CT_x sample was fit by components corresponding to C-Ti-O_x, C-Ti-$(OH)_x$, and H_2O_{ads} in addition to oxides and oxyfluorides of TiO_2 and $TiO_{2-x}F_x$, (**Table 5**) similar to the O 1s region of $Ti_3C_2T_x$. Surface organic contamination in the form C-O contribute to this region, which overlaps with, and obscures, many other peaks. However, the amount of these organic contaminations is ≈ 5.1 at.%.

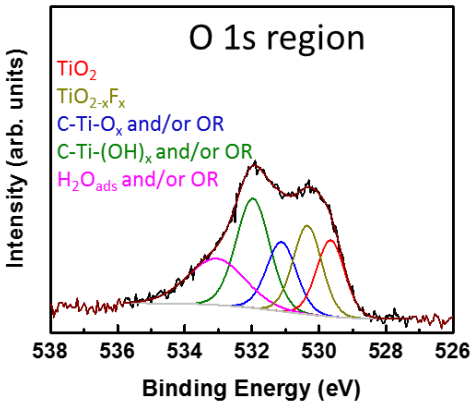

Figure 20. *Component peak fitting of XPS spectra of O 1s region for un-sputtered ML Ti_2CT_x-10HF cold pressed disk. Various peaks shown represent various species assumed to exist. Labels and peak colors are coordinated. The results are summarized in* ***Table 5****.*

F 1s region

The F 1s region (**Figure 21**) of the pre-sputtered Ti_2CT_x sample was fit by components corresponding to C-Ti-F_x, $TiO_{2-x}F_x$, and $Al(OF)_x$ (**Table 5**). The dominant F-containing component – at a fraction of 0.63 of the F 1s region – was C-Ti-F_x, at a BE of 685.2 eV, which is quite close to that of C-Ti-F_x for $Ti_3C_2T_x$ of 685.2 eV.

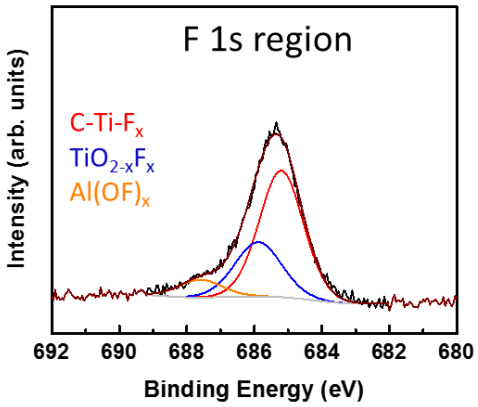

Figure 21. *Component peak fitting of XPS spectra of F 1s region for un-sputtered ML Ti_2CT_x-10HF cold pressed disk. Various peaks shown represent various species assumed to exist. Labels and peak colors are coordinated. The results are summarized in* ***Table 5****.*

***Table 5**. Summary of XPS peak fitting results for un-sputtered ML Ti_2CT_x-10HF cold pressed disk. The numbers in parenthesis in column 2 for the Ti 2p region are peak locations of* Ti $2p_{1/2}$*; their respective FWHMs are listed in column 3 in parenthesis.*

Region	BE [eV][a]	FWHM [eV][a]	Fraction	Assigned to	Reference
Ti $2p_{3/2}$ ($2p_{1/2}$)	454.8 (461.0)	0.9 (1.8)	0.30	(OH, or O)-Ti-C	[123,124]
	455.7 (461.2)	1.6 (1.9)	0.15	(OH, or O)-Ti^{2+}-C	[123]
	457.2 (462.9)	2.5 (2.2)	0.38	(OH, or O)-Ti^{3+}-C	[123]
	458.9 (464.5)	1.6 (1.4)	0.08	TiO_2	[120,121]
	459.6 (465.6)	1.5 (1.5)	0.04	$TiO_{2-x}F_x$	[122]
	460.7 (466.7)	1.6 (2.9)	0.05	C-Ti-F_x	[126]
C 1s	281.9	0.8	0.28	C-Ti-T_x	[123,124]
	284.6	1.4	0.42	C-C	[127]
	285.2	1.1	0.17	CH_x	[127]
	286.2	1.5	0.10	C-O	[127]
	289.0	1.5	0.03	COO	[127]
O 1s	529.7	0.9	0.16	TiO_2	[105,120]
	530.3	1.0	0.19	$TiO_{2-x}F_x$	[122]
	531.1	1.0	0.16	C-Ti-O_x and/or OR[b]	[105,128]
	532.0	1.1	0.28	C-Ti- $(OH)_x$ and/or OR[b]	[105]
	533.1	2.0	0.21	H_2O_{ads} and/or OR[b]	[105,128]
F 1s	685.2	1.5	0.63	C-Ti-F_x	[126]
	685.9	1.6	0.29	$TiO_{2-x}F_x$	[122]
	687.6	1.5	0.08	$Al(OF)_x$	[129]

[a] Values in parenthesis correspond to the $2p_{1/2}$ component.
[b] OR stands for organic compounds due to atmospheric surface contaminations.

4.1.3. XPS analysis of multilayered Ti3CNT$_x$-30HF

Figures 22-26 plot the spectra for Ti, C, O and F regions, respectively, for un-sputtered Ti_2CT_x-30HF, ML, cold pressed disk, together with their peak-fits. The peak positions, FWHM, and the fraction of each peak obtained from the fits are summarized in **Table 6.** Each region is discussed in detail below.

Ti 2p region

The Ti 2p region (**Figure 22**) of the un-sputtered Ti_3CNT_x sample was fit by the components listed in column 5 in **Table 6**. The majority of the species are: a) Ti atoms bonded to C and a surface termination of O and/or OH: (OH and/or O-Ti-CN), (OH and/or O-Ti^{+2}-CN), and (OH and/or O-Ti^{+3}-CN) that belong to $Ti_3C_2O_x$, $Ti_3CN(OH)_x$

and, b) Ti atoms bonded to C and F surface terminations (F-Ti-CN), which belong to Ti_3CNF_x. These comprise 86% of the photoemission in the Ti 2p region; the rest belongs to TiO_2 and $TiO_{2-x}F_x$ species arising from surface oxidation.

The binding energy (BE) for the Ti $2p_{3/2}$ peak of the Ti_3CNT_x sample (≈ 455.1 eV) is very close to that for $Ti_3C_2T_x$ and Ti_2CT_x, at 455.0 and 454.9 eV, respectively. This indicates that replacing half of the C atoms with N atoms has almost no effect on the chemical nature of the Ti atoms. In addition, the ratio of the three Ti oxidation states in Ti_3CNT_x is similar to that for $Ti_3C_2T_x$ (1:0.8:1.1 vs. 1:1.1:1.1, respectively).

Similar to $Ti_3C_2T_x$ and Ti_2CT_x, the BE for the Ti $2p_{3/2}$ peak of Ti_3CNT_x (455.1 eV) is higher than the 454.5 eV value in the parent MAX phase, Ti_3AlCN [114]. This shift is due to the replacement of the Al layers by more electronegative surface terminations such as O, OH and F.

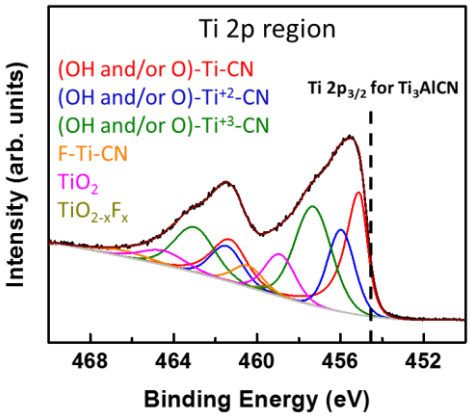

Figure 22. *Component peak fitting of XPS spectra of Ti 2p region for un-sputtered ML Ti_3CNT_x-30HF cold pressed disk. Various peaks shown represent various species assumed to exist. Labels and peak colors are coordinated. The results are summarized in* ***Table 7****. Dashed vertical line denotes the position of the same peak in the parent MAX phase.*

C 1s region

Before sputtering, this region (**Figure 22**) was fit by components corresponding to TiCN, NC-Ti-T_x, graphitic carbon (C-C), CH_x, C-O, and COO (**Table 6**). The TiCN component is highly likely to arise from a titanium carbonitride secondary phase

already in the starting material before etching; however, the percentage of that component in the C 1 s region is not more than 1.1 at. %. It is worth noting that the same component was not distinguished in the Ti 2p region.

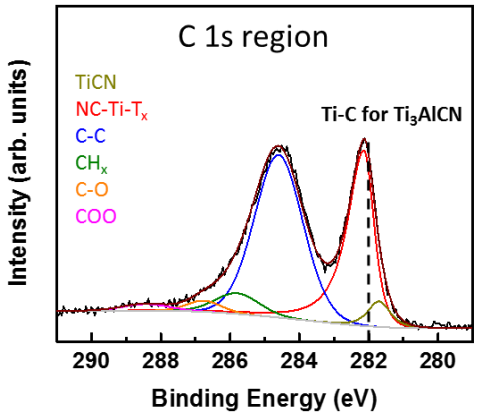

Figure 23. *Component peak fitting of XPS spectra of C 1s region for un-sputtered ML Ti_3CNT_x-30HF cold pressed disk. Various peaks shown represent various species assumed to exist. Labels and peak colors are coordinated. The results are summarized in* ***Table 6****. Dashed vertical line denotes the position of the same peak in the parent MAX phase.*

N 1s region

The N 1s region (**Figure 24**) of the pre-sputtered Ti_3CNT_x samples was fit by components corresponding to NC-Ti-T_x, TiCN (secondary phase of titanium carbonitride initially present in starting MAX powder [40]), CH_3CN and NH_4NO_3. The latter two most likely arise from surface contamination (**Table 6**).

The BE of NC-Ti-T_x (396.5 eV) is slightly higher than that of the Ti-N species in the parent MAX Ti_3AlCN (397.0 eV) [114]. The difference may be due to defects introduced in the N sites during the etching process.

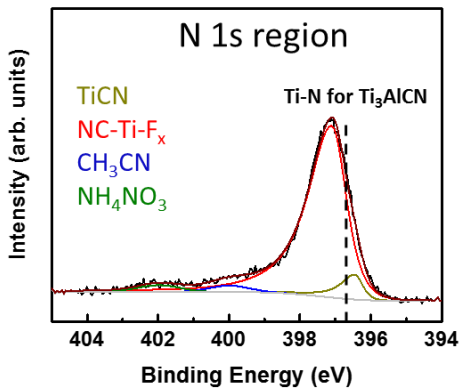

Figure 24. *Component peak fitting of XPS spectra of N 1s region for un-sputtered ML Ti_3CNT_x-30HF cold pressed disk. Various peaks shown represent various species assumed to exist. Labels and peak colors are coordinated. The results are summarized in* ***Figure 25****. Dashed vertical line denotes position of same peak in the parent MAX phase.*

O 1s region

Similar to $Ti_3C_2T_x$ and Ti_2CT_x, the O 1s region of Ti_3CNT_x (**Figure 25**) was fit by components corresponding to NC-Ti-O_x, NC-Ti-$(OH)_x$, and H_2O_{ads} (**Table 6**). In addition to TiO_2 and $TiO_{2-x}F_x$, which are due to surface oxidation. Surface C-O organic contaminants are also found in this region. These overlap with, and obscure, many other peaks. However, the amount of these organic contaminations is < 1.2 at.%.

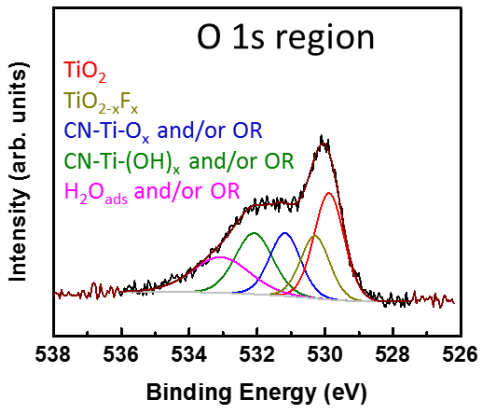

Figure 25. *Component peak fitting of XPS spectra of O 1s region for un-sputtered ML Ti_3CNT_x-30HF cold pressed disk. Various peaks shown represent various species assumed to exist. Labels and peak colors are coordinated. The results are summarized* ***Table 6****.*

F 1s region

The F 1s region for this sample (**Figure 26**) was fit by components corresponding to NC-Ti-F_x, $TiO_{2-x}F_x$, AlF_x, and/or $Al(OF)_x$ (**Table 6**). The two major

F-containing components were N/C-Ti-F_x and $TiO_{2-x}F_x$, at fractions of 0.40 and 0.54, respectively.

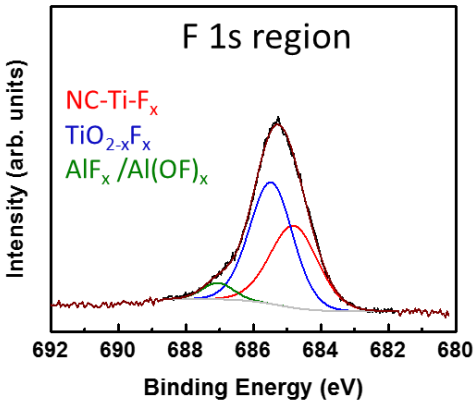

Figure 26. *Component peak fitting of XPS spectra of F 1s region for un-sputtered ML Ti_3CNT_x-30HF cold pressed disk. Various peaks shown represent various species assumed to exist. Labels and peak colors are coordinated. The results are summarized in* ***Table 6****.*

Table 6. *Summary of XPS peak fitting results for un-sputtered ML Ti_3CNT_x-30HF cold pressed disk. The numbers in parenthesis in column 2 for the Ti 2p region are peak locations of* Ti $2p_{1/2}$*; their respective FWHMs are listed in column 3 in parenthesis.*

Region	BE [eV][a]	FWHM [eV][a]	Fraction	Assigned to	Reference
Ti $2p_{3/2}$ ($2p_{1/2}$)	455.1 (461.3)	0.9 (1.9)	0.28	(OH, or O)-Ti-CN	[123]
	456.0 (461.5)	1.5 (1.8)	0.22	(OH, or O)-Ti^{2+}-CN	[123]
	457.3 (463.0)	2.1 (2.3)	0.32	(OH, or O)-Ti^{3+}-CN	[120,121]
	458.9 (464.5)	1.7 (2.5)	0.11	TiO_2	[122]
	459.6 (465.6)	1.1 (2.0)	0.01	$TiO_{2-x}F_x$	[126]
	460.4 (466.4)	1.7 (3.0)	0.06	NC-Ti-F_x	[126]
C 1s	281.7	0.8	0.05	TiCN	[131,132]
	282.1	0.7	0.35	NC-Ti-T_x	[123,124]
	284.6	1.6	0.50	C-C	[127]
	285.8	1.5	0.06	CH_x	[127]
	286.8	1.2	0.02	C-O	[127]
	288.4	1.6	0.02	COO	[127]
O 1s	529.9	1.1	0.31	TiO_2	[105,120]
	530.3	1.0	0.13	$TiO_{2-x}F_x$	[122]
	531.1	1.1	0.13	NC-Ti-O_x and/or OR[b]	[105,128]
	531.9	1.4	0.23	NC-Ti-$(OH)_x$ and/or OR[b]	[105,128]
	533.0	2.0	0.20	H_2O_{ad} and/or OR[b]	[105,128]
F 1s	684.8	1.7	0.40	NC-Ti-F_x	[126]
	685.5	1.5	0.54	$TiO_{2-x}F_x$	[122]
	687.0	2.1	0.05	AlF_x and/or $Al(OF)_x$	[129]
N 1s	396.5	0.6	0.08	TiCN	[131,132]
	397.1	1.0	0.86	NC-Ti-T_x	[131,132]
	400.0	1.3	0.03	CH_3CN	[133]
	402.0	1.4	0.03	NH_4NO_3	[134]

[a] Values in parenthesis corresponds to the $2p_{1/2}$ component.
[b] OR stands for organic compounds due to atmospheric surface contaminations.

4.1.4. XPS analysis of multilayered Nb_2CT_x-50HF and $Nb_4C_3T_x$-50HF

Figures 27.a-30.a plot the spectra for Nb, C, O, and F regions, respectively, for un-sputtered Nb_2CT_x-50HF, ML, cold pressed disk, together with their peak-fits. Similarly, **Figures 27.b-30.b** plot the spectra for Nb, C, O, and F regions, respectively, for un-sputtered $Nb_4C_3T_x$-50HF, ML, cold pressed disk, together with their peak-fits. The peak positions, FWHM, and the fraction of each peak obtained from the fits for Nb_2CT_x-50HF and $Nb_4C_3T_x$-50HF are summarized in **Tables 7 and 8,** respectively.

Nb 3d region

The Nb 3d region of the un-sputtered Nb_2CT_x sample (**Figure 27.a)** was fit by the components listed in column 5 in **Table 7**. The components are Nb atoms bonded to C and a surface termination of O and/or OH [(OH and/or O)-Nb-C], and Nb atoms bonded to C and F surface termination (C-Nb-F_x). These species comprised 75% of the photoemission in the region; the rest is assigned to various oxides and oxyfluorides including NbO, Nb_2O, $NbO_{1-x}F_x$ and Nb_2O_5 [135]. The binding energy of the Nb $3d_{5/2}$ [(OH and/or O)-Nb-C] species for the Nb_2CT_x sample (204.2 eV) is 0.2 eV higher than its counterpart in Nb_2AlC_2 [114]. This increase in BE is due to the replacement of the Al layers by more electronegative surface terminations.

The Nb 3d region of un-sputtered $Nb_4C_3T_x$ sample (**Figure 27.b**) was fit by the same components (**Table 8**) as for Nb_2CT_x. In addition, an extra component attributed to the two inner metal carbide atom layers (Nb-C) with a BE of 203.3 eV, which is 0.9 eV lower than the BE of (OH and/or O)-Nb-C components and is very close to the same component found in Nb_4AlC_3 (203.0 eV) [114]. Moreover, the ratio of the peak areas of Nb-C and (OH and/or O)-Nb-C components is 1:1, which is the same ratio as that for the outer Nb layers to the inner ones. This result is expected because the Nb-C component in the $Nb_4C_3T_x$ has no surface terminations, thus it would be less electronegative than the (OH and/or O)-Nb-C. The slight increase in BE compared to the same component in Nb_4AlC_3 might be due to the formation of defects during the etching process. It is worth noting that the component belonging to the inner metal carbide (no terminations) were able to be fitted and identified for the $M_4C_3T_x$ phases where two layers of non-terminated metal carbides exist. However, it was not possible to identify and fit for the same component in the $M_3X_2T_x$ phases, where one non-terminated inner metal carbide exists.

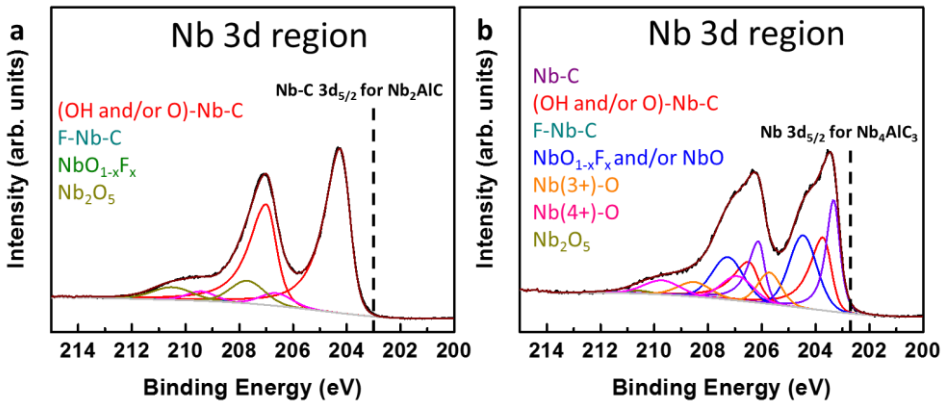

Figure 27. *Component peak fitting of XPS spectra of Nd 3d region for un-sputtered, a) ML Nb_2CT_x-50HF and, b) ML Nb_3CT_x-50HF cold pressed disks. Various peaks shown represent various species assumed to exist. Labels and peak colors are coordinated. The results are summarized in* ***Tables 7*** *and* ***8****. Dashed vertical line denotes the position of the same peak – immediately to its left - in the parent MAX phase.*

C 1s region

The C 1s region of un-sputtered Nb_2CT_x sample (**Figure 28.a**) was fit by components, listed in **Table 7**, corresponding to C-Nb-T_x, C-C and CH_x, C-O, and COO. The peak corresponding to C-Nb-T_x has a BE of 282.4 eV, which is slightly higher than that of Nb_2AlC (282.7 eV) [114].

The C 1s region of un-sputtered $Nb_4C_3T_x$ sample (**Figure 28.b**) was fit by the same components (**Table 8**) as for Nb_2CT_x. In addition, an extra component attributed to C atoms bonded to the two inner Nb layers was found. At 282.1 eV, the BE of this component is lower than that of the C-Nb-T_x component (282.7 eV). It is important to note that ratio of the areas of the Nb-C peak to C-Nb-T_x peaks is 1:2, which is the same as the ratio of the inner C layers to the outer C layers. As expected the BE of the Nb-C component in $Nb_4C_3T_x$ is the same as that for the Nb-C component in Nb_4AlC_3 [114]. These results are gratifying since they indirectly confirm the validity of our analysis.

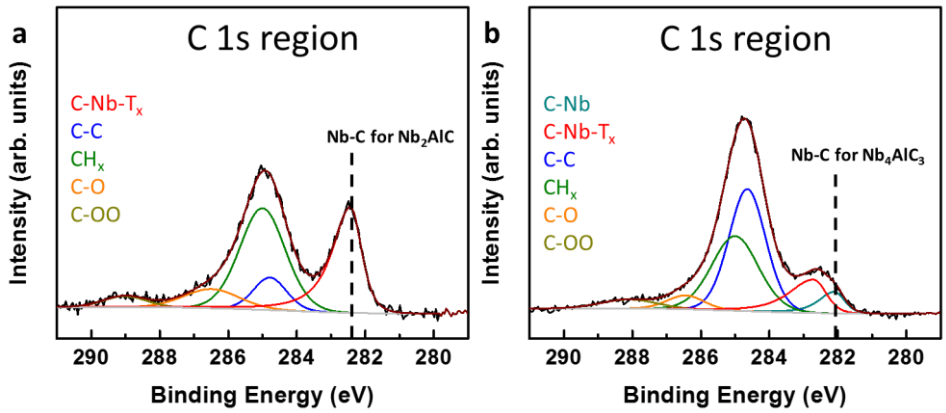

Figure 28. *Component peak fitting of XPS spectra of C 1s region for un-sputtered, a) ML Nb_2CT_x-50HF and, b) ML Nb_3CT_x-50HF cold pressed disks. Various peaks shown represent various species assumed to exist. Labels and peak colors are coordinated. The results are summarized in* ***Tables 7*** *and* ***8****. Dashed vertical line denotes the position of the same peak – immediately to its left - in the parent MAX phase.*

O 1s region

The O 1s regions of un-sputtered Nb_2CT_x (**Figure 29.a**) and $Nb_4C_3T_x$ (**Figure 29.b**) samples were fit by the same components, listed in **Tables 7 and 8**, respectively. These components correspond to C-Nb-O_x, C-Nb-$(OH)_x$ and H_2O_{ads}. These species comprise ≈ 65% of the O 1s region photoemission for Nb_2CT_x and ≈ 71% for $Nb_4C_3T_x$ (Table 5). Note that the H_2O_{ads} peak position is located quite close to the same species discussed above for $Ti_3C_2T_x$, lending credence to its assignment. The remainder of the spectra is fit by components corresponding to oxides of Nb_2O_5 [129,130,136-138]. These species are a result of surface oxidation. Surface organic contaminations of C-O contribute to this region, which overlaps with, and obscures, many other peaks. The amounts of these organic contaminants for Nb_2CT_x and $Nb_4C_3T_x$ samples are 5.2 and 4.4 at. %, respectively.

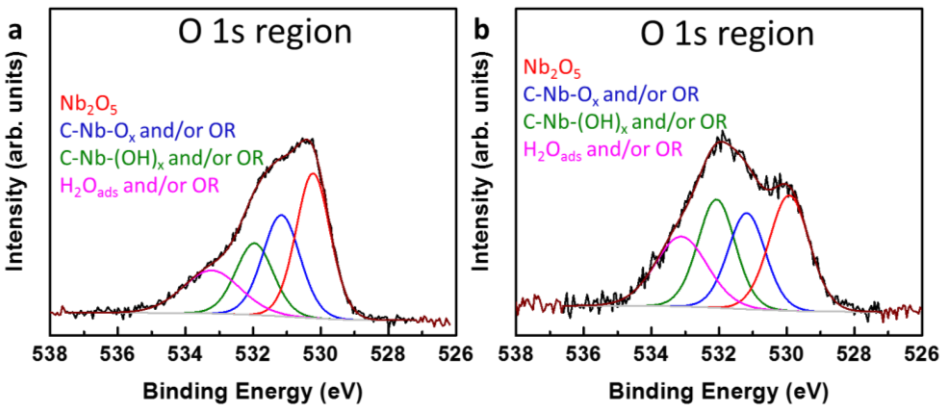

Figure 29. *Component peak fitting of XPS spectra of O 1s region for un-sputtered, a) ML Nb_2CT_x-50HF and, b) ML Nb_3CT_x-50HF cold pressed disks. Various peaks shown represent various species assumed to exist. Labels and peak colors are coordinated. The results are summarized in* ***Tables 7*** *and* ***8****.*

F 1s region

The F 1s regions of un-sputtered Nb_2CT_x (**Figure 30.a**) and $Nb_4C_3T_x$ (**Figure 30.b**) samples were fit by the same components, listed in **Tables 7 and 8**, respectively. These components correspond to C-Nb-F_x and $NbO_{1-x}F_x$. The peak assigned to C-Nb-F_x sits at a BE of 684.7 and 684.6 eV for Nb_2CT_x and $Nb_4C_3CT_x$, respectively, which is slightly higher than the F 1s peak value for NbF_5 [139]. $NbO_{1-x}F_x$ is due to surface oxidation.

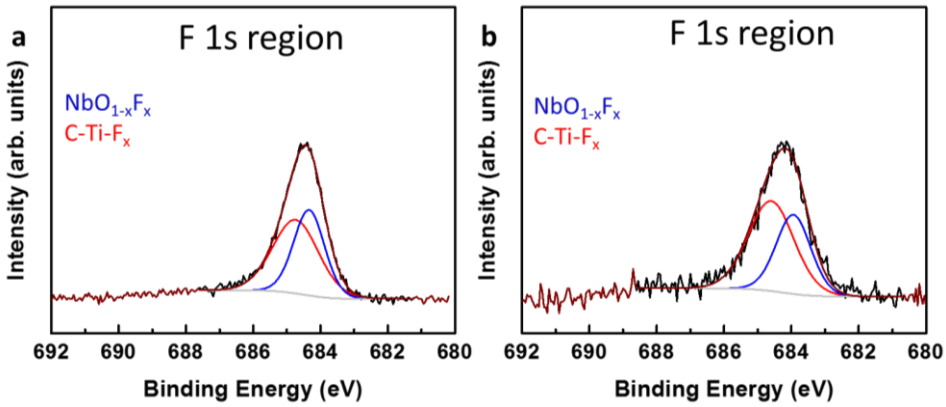

Figure 30. *Component peak fitting of XPS spectra of F 1s region for un-sputtered, a) ML Nb_2CT_x-50HF and, b) ML Nb_3CT_x-50HF cold pressed disks. Various peaks shown represent various species assumed to exist. Labels and peak colors are coordinated. The results are summarized in* ***Tables 7*** *and* ***8****.*

Table 7. *XPS peak fitting results for un-sputtered ML Nb_2CT_x-50HF cold pressed disk. The numbers in parenthesis in column 2 for the Nb 3d region are peak locations of* Nb $3d_{3/2}$; *their respective FWHMs are listed in column 3 in parenthesis.*

Region	BE [eV][a]	FWHM [eV][a]	Fraction	Assigned to	Reference
Nb $3d_{5/2}$ ($3d_{3/2}$)	204.2 (207.0)	0.9 (0.9)	0.81	(OH and/or O)-Nb-C	[135,140]
	206.6 (209.4)	1.4 (1.3)	0.07	$NbO_{1-x}F_x$	
	207.7 (210.5)	1.2 (1.6)	0.10	Nb_2O_5	[135,141,142]
	208.6 (211.4)	0.9 (1.0)	0.02	C-Nb-F_x (III)	[139]
C 1s	282.4	0.8	0.34	C-Nb-Tx	[143]
	284.8	1.1	0.10	C-C	[127]
	285.0	1.6	0.42	CHx	[127]
	286.5	1.9	0.10	C-O	[127]
	289.0	1.5	0.04	COO	[127]
O 1s	530.2	1.2	0.36	Nb_2O_5	[128,136-138]
	531.2	1.3	0.27	C-Nb-O_x[b]	[128]
	532.0	1.3	0.19	C-Nb-$(OH)_x$ and/or OR[b]	[128]
	533.2	2.0	0.18	H_2O_{ads} (IV) and/or OR[b]	[128]
F 1s	684.3	1.1	0.44	$NbO_{1-x}F_x$	
	684.7	1.6	0.56	C-Nb-F_x (III)	[139]

[a] Values in parenthesis corresponds to the $3d_{3/2}$ component.
[b] OR stands for organic compounds due to atmospheric surface contaminations.

Table 8. *XPS peak fitting results for un-sputtered ML $Nb_4C_3T_x$-50HF cold pressed disk. The numbers in parenthesis in column 2 for the Nb 3d region are peak locations of* Nb $3d_{3/2}$; *their respective FWHMs are listed in column 3 in parenthesis.*

Region	BE [eV][a]	FWHM [eV][a]	Fraction	Assigned to	Reference
Nb $3d_{5/2}$ ($3d_{3/2}$)	203.3 (206.1)	0.6 (0.6)	0.26	Nb-C	
	203.9 (206.7)	0.7 (0.9)	0.26	(OH and/or O)-Nb-C	[135,140]
	204.5 (207.3)	1.2 (1.4)	0.25	NbO and/or $NbO_{1-x}F_x$	[135,141,142]
	205.7 (208.5)	1.0 (1.4)	0.10	Nb^{+3}-O	[135,141,142]
	206.9 (209.7)	1.4 (1.6)	0.10	Nb^{+4}-O	[135,141,142]
	207.8 (210.6)	1.0 (1.0)	0.01	Nb_2O_5	[139,142]
	208.6 (211.4)	1.4 (1.4)	0.02	C-Nb-F_x (III)	
C 1s	282.1	0.7	0.06	Nb-C	[143]
	282.7	0.9	0.12	C-Nb-T_x	[143]
	284.7	1.3	0.41	C-C	[127]
	285.0	1.6	0.33	CH_x	[127]
	286.4	1.2	0.04	C-O	[127]
	288.1	2.0	0.04	COO	[127]
O 1s	530.0	1.4	0.29	Nb_2O_5	[136-138]
	531.2	1.3	0.23	C-Nb-O_x and/or OR[b]	
	532.0	1.3	0.25	C-Nb-$(OH)_x$ and/or OR[b]	[128]
	533.1	1.9	0.23	H_2O_{ads} (IV) and/or OR[b]	[128]
F 1s	683.8	1.2	0.40	$NbO_{1-x}F_x$	
	684.6	1.6	0.60	C-Nb-F_x (III)	[139]

[a] Values in parenthesis corresponds to the $3d_{3/2}$ component.
[b] OR stands for organic compounds due to atmospheric surface contaminations.

4.1.5. XPS analysis of multilayered V_2CT_x-50HF

Figures 31-34 plot the spectra for V, C, O and F regions, respectively, for un-sputtered V_2CT_x-50HF, ML, cold pressed disk, together with their peak-fits. The peak positions, FWHM, and the fraction of each peak obtained from the fitting are summarized in **Table 9**.

V 2p region

The V 2p region of the un-sputtered V_2CT_x sample (**Figure 31**) was fit by two components listed in column 5 in **Table 9**. The first species is assigned to V atoms bonded to C and a surface termination (T_x) of O, OH and/or F (C-V-T_x). This species

comprises 77% of the photoemission in this region. The second is a species related to mixed vanadium oxides (VO_x) present presumably due to surface oxidation. The BE of the V $2p_{3/2}$ C-V-T_x peak (513.0 eV) is 0.5 eV higher than its counterpart in V_2AlC (**Figure 67.a**). This increase in BE is due to the replacement of the Al layers by more electronegative surface terminations, as described previously [45].

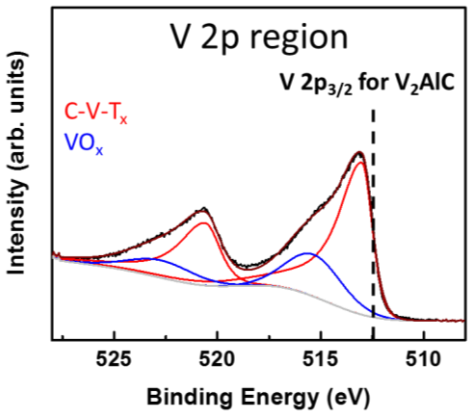

Figure 31. *Component peak fitting of XPS spectra of V 2p region for un-sputtered ML V_2CT_x-50HF cold pressed. Various peaks shown represent various species assumed to exist. Labels and peak colors are coordinated. The results are summarized in* ***Table 9****. Dashed vertical line denotes the position of the same peak in the parent MAX phase.*

C 1s region

The C 1s region (**Figure 32** and **Table 9**) of the un-sputtered V_2CT_x sample was fit by C-V-T_x, a species assigned to C atoms bonded to V atoms. The BE of this species (282.0 eV) is identical to its counterpart species in V_2AlC (**Figure 67.b**) indicating that the chemical environment of the C atoms is not altered by the replacement of Al atoms with surface terminations through HF etching. This confirms what has been observed previously for other MXenes. The rest of the region was fit by C-C, CH_x, C-O, and COO components belonging to surface contaminations.

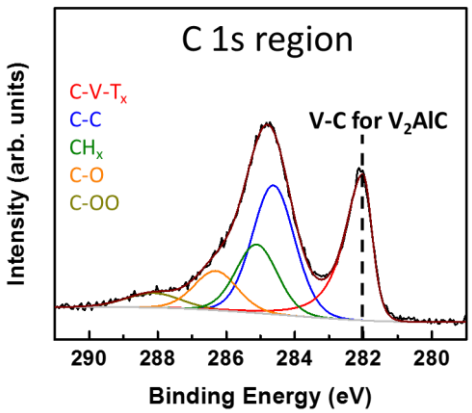

Figure 32: *Component peak fitting of XPS spectra of C 1s region for un-sputtered ML V_2CT_x-50HF cold pressed disk. Various peaks shown represent various species assumed to exist. Labels and peak colors are coordinated. The results are summarized in* ***Table 9****. Dashed vertical line denotes the position of the same peak in the parent MAX phase.*

O 1s region

The O 1s region for un-sputtered V_2CT_x sample (**Figure 33** and **Table 9**) was fit by components corresponding to C-V-O_x, C-V-$(OH)_x$, and H_2O_{ads}. These species comprise the majority fraction (74%) of that region. The balance is in the form of mixed vanadium oxides (VO_x) resulting from surface oxidation [144]. Surface organic contaminations of C-O and COO contribute to this region, which overlap and obscure many other peaks. The amount of these organic contaminations is 6.2 at. %.

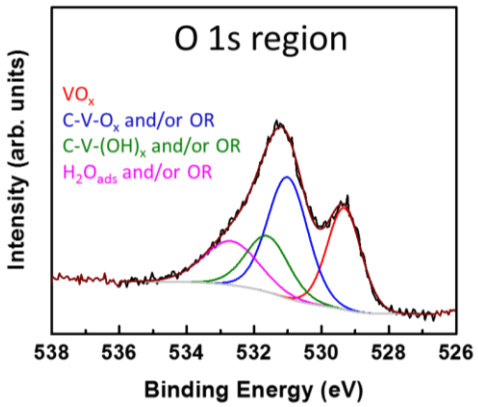

Figure 33: *Component peak fitting of XPS spectra of O 1s region for un-sputtered ML V_2CT_x-50HF. Various peaks shown represent various species assumed to exist. Labels and peak colors are coordinated. The results are summarized in* ***Table 9****.*

F 1s region

The F 1s region (**Figure 34** and **Table 9**) for this sample was fit by a major component – 85 % of the region – and assigned to F atoms bonded to V atoms in the MXene, viz. C-V-F_x. The BE of this species (684.3 eV) is higher than that of the V-F bond in $C_{16}(VOF_3)F$ by 1.7 eV [145], this difference can be attributed to the effect of introducing O atoms in $C_{16}(VOF_3)F$ and the interaction of these O atoms with the F atoms. The rest of the region was fit by a species attributed to F bonded to C atoms arising from the fluorination of the latter. Like in all other MXenes, the C results from the dissolution of some V atoms during etching [145].

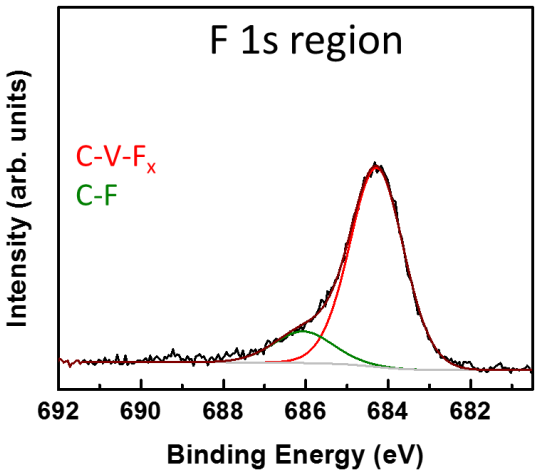

Figure 34. *Component peak fitting of XPS spectra of F 1s region for un-sputtered ML V_2CT_x-50HF. Various peaks shown represent various species assumed to exist. Labels and peak colors are coordinated. The results are summarized in* ***Table 9****.*

Table 9. *XPS peak fitting results for un-sputtered ML V_2CT_x-50HF cold pressed disk. The numbers in parenthesis in column 2 for the V 2p region are peak locations of* V $2p_{1/2}$*; their respective FWHMs are listed in column 3 in parenthesis.*

Region	BE [eV][a]	FWHM [eV][a]	Fraction	Assigned to	Reference
V $2p_{3/2}$	513.0 (520.6)	1.2 (1.7)	0.75	C-V-T_x	
($2p_{1/2}$)	515.3 (522.7)	3.1 (3.8)	0.25	VO_x	[144]
C 1s	282.0	0.7	0.30	C-V-Tx	
	284.6	1.4	0.35	C-C	[127]
	285.1	1.4	0.18	CHx	[127]
	286.3	1.5	0.11	C-O	[127]
	288.1	1.9	0.05	COO	[127]
O 1s	530.2	1.2	0.36	VO_x	[144]
	531.2	1.3	0.27	C-V-O_x[b]	[113,128]
	532.0	1.3	0.19	C-V-$(OH)_x$ and/or OR[b]	[128 113]
	533.2	2.0	0.18	H_2O_{ads} (IV) and/or OR[b]	[128 113]
F 1s	684.3	1.1	0.44	C-Nb-F_x	[145]
	684.7	1.6	0.56	C-F	[145]

[a] Values in parenthesis corresponds to the $2p_{1/2}$ component.
[b] OR stands for organic compounds due to atmospheric surface contaminations.

4.1.6. XPS analysis of multilayered Mo_2CT_x-25HF

Unlike the rest of MXenes which are produced by selective etching of Al from their MAX phases as described previously (see literature background section), Mo_2CT_x is produced by etching of Ga from a newly discovered phase. This phase is similar to the MAX phases, but instead of one "A" layer such as Mo_2GaC [146] – the only known Ga-containing MAX phase known to date - two "A" layers are found between the Mo_2C layers [147]. The crystal structures of Mo_2GaC and Mo_2Ga_2C are compared in **Figures 35.a** and **b**, respectively.

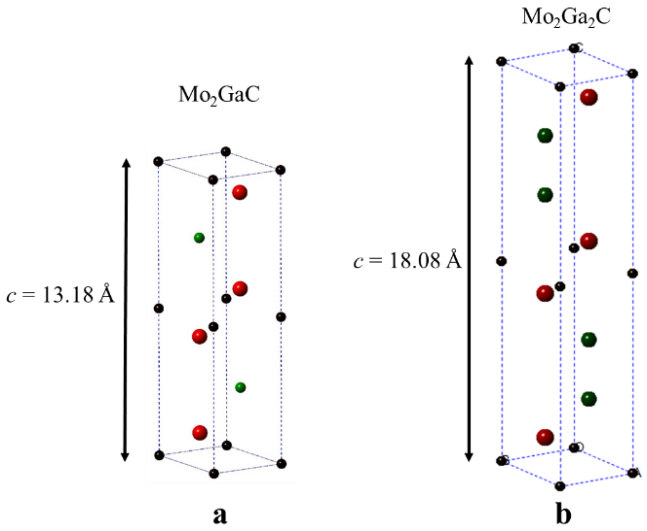

Figure 35. *Unit cells of a) Mo_2GaC and, b) Mo_2Ga_2C.*

Figures 36-39 plot the spectra for Mo, C, O, and F regions, respectively, for un-sputtered Mo_2CT_x-25HF, ML, cold pressed disk, together with their peak fits. The peak positions, FWHM, and the fraction of each peak obtained from the fits are summarized in **Table 10**.

Mo 3d region

The Mo 3d region of the un-sputtered Mo_2CT_x samples (**Figure 36**) was fit by four components listed in column 5 in **Table 10**. The major species occupying ≈ 71 % of the photoemission spectra is attributed to Mo atoms bonded to C atoms and surface terminations, T_x, labelled "C-Mo-T_x". This species belongs to the Mo_2CT_x MXene. The BE of the Mo $3d_{5/2}$ C-Mo-T_x peak (228.5 eV) is 0.4 eV higher than its counterpart in Mo_2Ga_2C [148]. Similar to the other MXenes, this increase is due to the replacement of the Ga layers by more electronegative surface terminations.

The rest of the 3d Mo region was fit by components belonging to mixed molybdenum oxides: Mo^{+6} and Mo^{+5} resulting from surface oxidation, and a component belonging to the binary carbide Mo_2C. The amount of this secondary phase is less than 1 at.%.

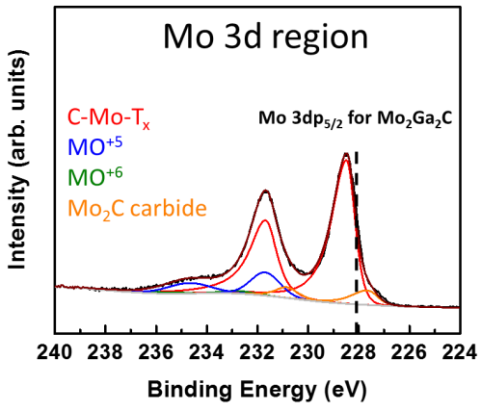

Figure 36. *Component peak fitting of XPS spectra of Mo 3d region for un-sputtered ML Mo_2CT_x-25HF cold pressed disk. Various peaks shown represent various species assumed to exist. Labels and peak colors are coordinated. The results are summarized in* ***Table 10****. Dashed vertical line denotes the position of the same peak in the parent MAX phase.*

C 1s region

The C 1s region (**Figure 37** and **Table 10**) of the un-sputtered Mo_2CT_x sample was fit by a species corresponding to C atoms bonded to Mo atoms in Mo_2CT_x, C-Mo-T_x while the rest of the species of C-C, CH_x, C-O, and COO belong to surface contaminants. The area of the C-Mo-T_x species occupy only 14% of the XPS spectra for C 1s region, while the rest belongs to the surface contamination carbon based species.

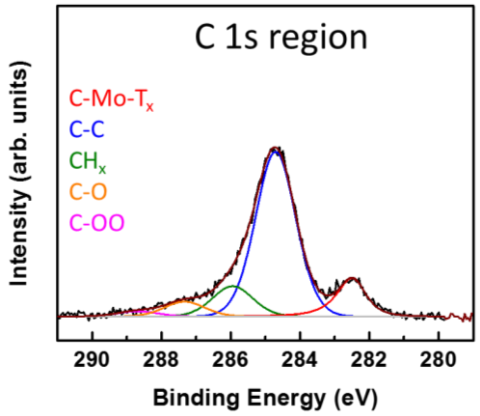

Figure 37. *Component peak fitting of XPS spectra of C 1s region for un-sputtered ML Mo_2CT_x-25HF cold pressed disk. Various peaks shown represent various species assumed to exist. Labels and peak colors are coordinated. The results are summarized in* ***Table 10.***

O 1s region

The O 1s region for un-sputtered Mo_2CT_x sample (**Figure 38** and **Table 10**) was fit by components corresponding to C-Mo-O_x, C-Mo-$(OH)_x$ and H_2O_{ads}. These species form the majority fraction (≈ 60%) of that region. The balance is in the form of mixed molybdenum oxides (MoO_x) resulting from surface oxidation [149]. Surface organic contaminations of C-O and COO contribute to this region, which overlap and obscure many other peaks. The amount of these organic contaminations is ≈ 5.0 at. %.

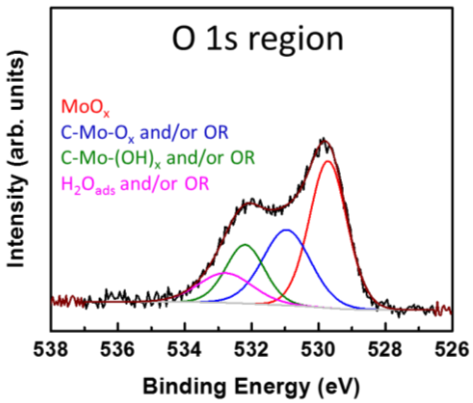

Figure 38. *Component peak fitting of XPS spectra of O 1s region for un-sputtered ML Mo_2CT_x-25HF cold pressed disk. Various peaks shown represent various species assumed to exist. Labels and peak colors are coordinated. The results are summarized in* ***Table 10****.*

F 1s region

The F 1s region (**Figure 39** and **Table 10**) for un-sputtered Mo_2CT_x samples was fit by one component corresponding to F atoms bonded to Mo atoms in the MXenes viz. Mo-F. The BE of this peak is 683.8 eV and was given that assignment because it is quite close to that made by Park *el al*. [150] who assigned a BE of 685.0 eV to F atoms bonded to Mo.

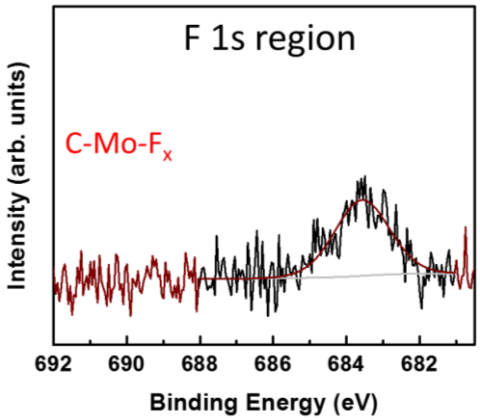

Figure 39: *Component peak fitting of XPS spectra of O 1s region for un-sputtered ML Mo_2CT_x-25HF cold pressed disk. Various peaks shown represent various species assumed to exist. Labels and peak colors are coordinated. The results are summarized in* ***Table 10****.*

Table 10. *XPS peak fitting results for un-sputtered ML Mo2CTx-25HF cold pressed disk. The numbers in parenthesis in column 2 for the Mo 3d region are peak locations of Mo $3d_{3/2}$; their respective FWHMs are listed in column 3 in parenthesis.*

Region	BE [eV][a]	FWHM [eV][a]	Fraction	Assigned to	Reference
Mo $3d_{5/2}$ ($3d_{3/2}$)	227.6 (230.8)	1.0 (1.1)	0.07	Mo_2C bulk carbide	[151]
	228.5 (231.7)	0.8 (1.0)	0.77	C-Mo-T_x	[148]
	231.7 (234.7)	1.4 (2.0)	0.13	Mo^{+5}	[149]
	232.8 (235.8)	1.5 (2.0)	0.02	Mo^{+6}	[149]
C 1s	282.6	1.0	0.14	C-Mo-Tx	[148]
	284.7	1.3	0.66	C-C	[127]
	285.9	1.3	0.12	CHx	[127]
	287.4	1.3	0.06	C-O	[127]
	288.8	1.3	0.02	COO	[127]
O 1s	529.7	1.3	0.42	MoO_x	[149]
	531.0	1.7	0.28	C-Mo-O_x[b]	[114]
	532.1	1.4	0.17	C-Mo-$(OH)_x$ and/or OR[b]	[114]
	532.8	1.9	0.12	H_2O_{ads} (IV) and/or OR[b]	[114]
F 1s	683.8	1.8	1.0	C-Mo-F_x	[150]

[a] Values in parenthesis corresponds to the $3d_{3/2}$ component.
[b] OR stands for organic compounds due to atmospheric surface contaminations.

4.1.7. XPS analysis of multilayered $Mo_2TiC_2T_x$-50HF and $Mo_2Ti_2C_3T_x$-50HF

As discussed in the section 2.2.1, $Mo_2TiC_2T_x$ and $Mo_2Ti_2C_3T_x$ are ordered MXenes [89,152,153]. For the most part, the Mo atoms occupy the outer layers while the Ti atoms occupy the inner layer(s). A cross-sectional schematic of fully ordered $Mo_2TiC_2T_x$ and $Mo_2Ti_2C_3T_x$ are shown in **Figures 40.a** and **b**, respectively.

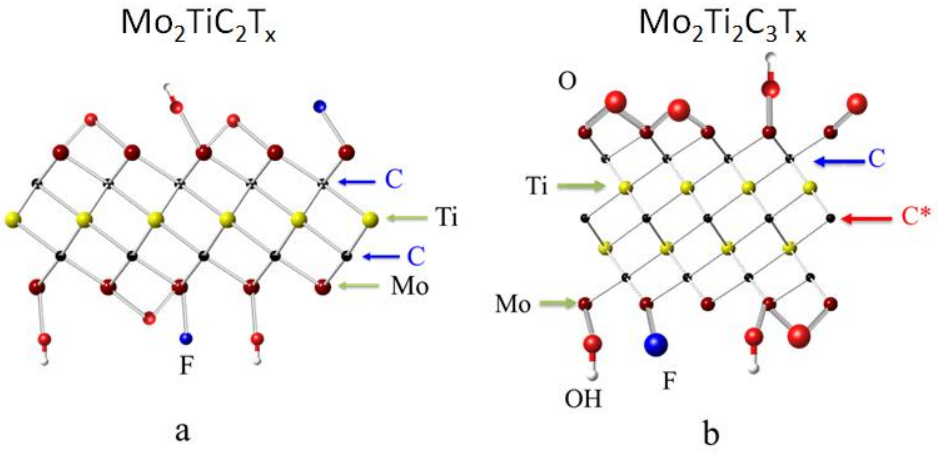

Figure 40. *Side view schematic of a) $Mo_2TiC_2T_x$ and, b) $Mo_2Ti_2C_3T_x$ structures showing various M atoms and their terminations. Here the Mo atoms are colored dark red, Ti, yellow, C, black, O, red, H white and F, blue (not to scale). C atoms bonded to core M atoms are designated C*.*

Figures 41.a-44.a plot the spectra for Mo, Ti, C, O, and F regions, respectively, for un-sputtered $Mo_2TiC_2T_x$-50HF, ML, cold pressed disk, together with their peak-fits. Similarly, **Figures 41.b-44.b** plot the spectra for Mo, Ti, C, O, and F regions, respectively, for un-sputtered and $Mo_2Ti_2C_3T_x$-50HF ML, cold pressed disk, together with their peak-fits. The peak positions, FWHM, and the fraction of each peak obtained from the fits for $Mo_2TiC_2T_x$-50HF and $Mo_2Ti_2C_3T_x$-50HF are summarized in **Tables 11 and 12,** respectively.

Mo 3d region

The Mo 3d region of the un-sputtered $Mo_2TiC_2T_x$ and $Mo_2Ti_2C_3T_x$ sample shown in **Figures 41.a** and **b**, respectively, was fit by the components listed in column 5 in **Tables 11** and **12,** respectively. These components are attributed to the same species discussed above for the Mo 3d region in Mo_2CT_x which are mainly C-Mo-T_x, and two species belonging to mixed molybdenum oxides: Mo^{+6} and Mo^{+5}. Moreover, an extra species was fit in the Mo 3d region of $Mo_2TiC_2T_x$ which belongs to the binary carbide Mo_2C; the amount of this secondary phase is ≈ 1.2 at. %.

The BE of the Mo $3d_{5/3}$ C-Mo-T_x peak is equal to 229.3 and 229.0 eV for $Mo_2TiC_2T_x$ and $Mo_2Ti_2C_3T_x$, respectively, which are higher than the BEs of their counterparts in Mo_2TiAlC_2 (227.8 eV) and $Mo_2Ti_2AlC_3$ (227.9 eV) [152]. This increase in the BE is due to the replacement of Al layer by more electronegative surface terminations similar to the other MXenes. Moreover, the BE of this species in both phases is higher than the same species in Mo_2CT_x. The reason for this state of affairs might be a slight intermixing between the Mo and Ti in the outer layers of the $Mo_2TiC_2T_x$ and $Mo_2Ti_2C_3T_x$. This comment notwithstanding more work is needed to confirm this conjecture.

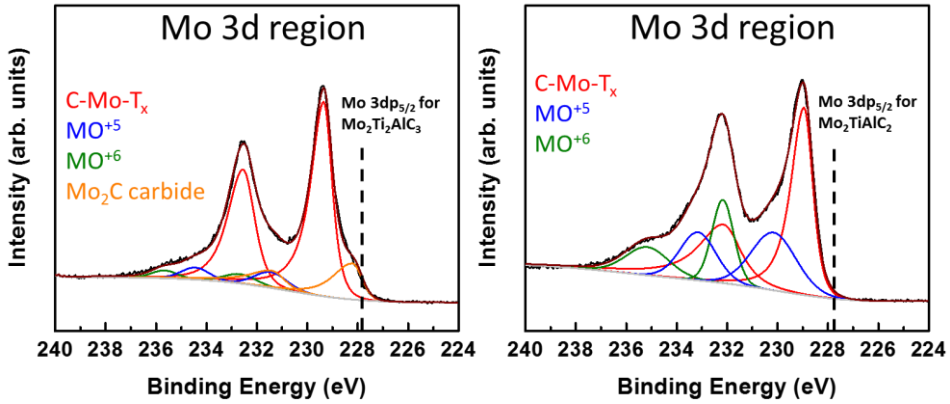

Figure 41. *Component peak fitting of XPS spectra of Mo 3d region for un-sputtered, a) ML $Mo_2TiC_2T_x$-50HF and b) ML $Mo_2Ti_2C_3T_x$-50HF cold pressed disks. The various peaks under the spectra represent various species assumed to exist. The results are summarized in* ***Tables 11*** *and* ***12****, respectively. Dashed vertical line denotes the position of the same peak in the parent MAX phase.*

Ti 2p region

The Ti 2p region of the un-sputtered $Mo_2TiC_2T_x$ and $Mo_2Ti_2C_3T_x$ (**Figures 42.a** and **b**, respectively) was fit by the corresponding components listed in column 5 in **Tables 11** and **12**, respectively. These components are attributed to the same species discussed above for the Ti 2p region in the Ti-based MXenes which are mainly Ti atoms bonded to C (Ti-C), (Ti^{+2}-C), and (Ti^{+3}-C), in addition to a minor species of titanium oxide. The ratio of fraction of the three oxidation states of Ti: Ti, Ti^{+2}, and Ti^{+3} in $Mo_2TiC_2T_x$ is 1:1.2:0.5, respectively, while that ratio in $Mo_2Ti_2C_3T_x$ is 1:0.7:0.2. This

shows that the total oxidation state of Ti in $Mo_2TiC_2T_x$ is higher in $Mo_2Ti_2C_3T_x$, this can be attributed to the extra core layer of Ti-C found in $Mo_2Ti_2C_3T_x$ which would contribute to decreasing the oxidation state of Ti.

The BE of the Ti $2p_{3/2}$ Ti-C peak is equal to 454.8 eV for both $Mo_2TiC_2T_x$ and $Mo_2Ti_2C_3T_x$, respectively, which are lower than the BEs of the same carbide species for $Ti_3C_2T_x$, Ti_2CT_x and Ti_3CNT_x (455.0 eV) but higher than the BEs of their counterparts in Mo_2TiAlC_2 (454.4 eV) and $Mo_2Ti_2AlC_3$ (454.4 eV) [152]. Since, in both compounds, the Ti atoms occupy the core layers, they are expected have no surface terminations. Therefore, their BEs will be lower than Ti atoms bonded to surface terminations as in $Ti_3C_2T_x$, Ti_2CT_x and Ti_3CNT_x and almost similar to the BE of the Ti-C species in their counterpart MAX phases. However, the increase in their BEs compared to the corresponding parent MAX phases might be attributed to defects in the Ti layers during etching, given that Ti-based MAX phases are less stable in HF compared to Mo-based MAX phases. Ti-based MAX phases take less than 24 hrs in HF at room temperature to be converted to MXene, while Mo-based MAX phases take more than 3 days in HF at 55 ^oC to be converted to MXene [53,89].

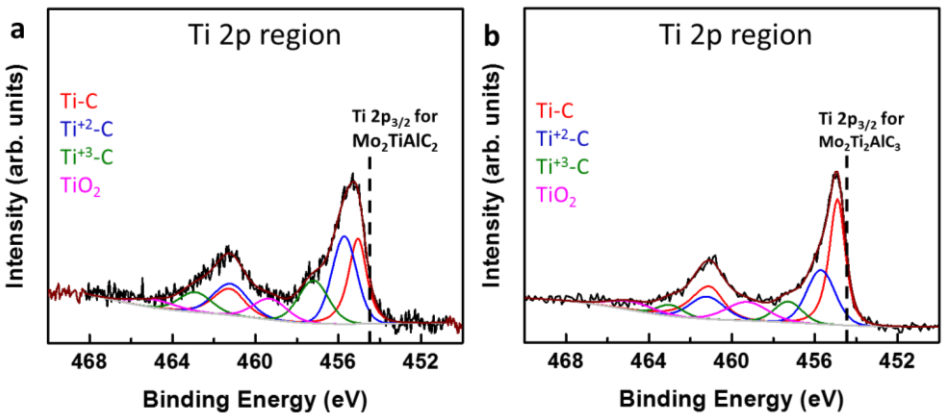

Figure 42. *Component peak fitting of XPS spectra of Ti 2p region for un-sputtered, a) ML $Mo_2TiC_2T_x$-50HF and b) ML $Mo_2Ti_2C_3T_x$-50HF cold pressed disks. The various peaks under the spectra represent various species assumed to exist. The results are summarized in* ***Tables 11*** *and* ***12****, respectively. Dashed vertical line denotes the position of the same peak in the parent MAX phase.*

C 1s region

The C 1s region of un-sputtered Mo_2TiAlC_2 sample (**Figure 43.a**) was fit by components listed in **Table 11**. The main component corresponds to carbon atoms bonded to Mo and Ti atoms, which are the metal carbide species in Mo_2TiAlC_2 MXene (labelled as "C-Mo/Ti-T_x"). The binding energy of this component is at 282.5 eV and is the same BE as that of its counterpart in Mo_2TiAlC_2. The BE value of "C-Mo/Ti-T_x" falls between the BEs of "C-Ti-T_x" for $Ti_3C_2T_x$ and C-Mo-T_x" for Mo_2CT_x, 282.0 and 282.6 eV, respectively. This is predictable since the carbon atoms are bonded to both Ti and Mo atoms, as shown in **Figure 40.a**. The rest of this region's spectra was fit by C-C CH_x, C-O, and COO, which arise from surface contamination.

The C 1s region of un-sputtered $Mo_2Ti_2C_3T_x$ sample (**Figure 43.b**) was fit by components, listed in **Table 12**, corresponding to C-Ti, C-Mo-T_x, C-C, CH_x, C-O and COO. The C-Ti component of BE of 281.9 eV is attributed to the carbon atoms bonded to the Ti inner layer as shown in **Figure 40.b.** The BE of this component is very close to that of C-Ti-T_x component in $Ti_3C_2T_x$. The C-Mo/Ti-T_x component is the same component and has the same BE (282.5 eV) as in $Mo_2TiC_2T_x$ which is attributed to the carbon atoms bonded to both Ti and Mo atoms. The rest of the components of C-C, CH_x, C-O and COO are attributed to surface contamination.

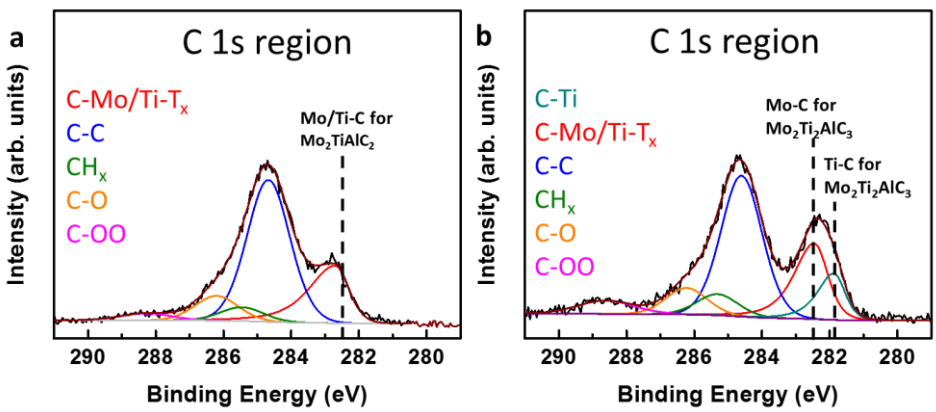

Figure 43. *Component peak fitting of XPS spectra of C 1s region for un-sputtered, a) ML $Mo_2TiC_2T_x$-50HF and b) ML $Mo_2Ti_2C_3T_x$-50HF cold pressed disks. The various peaks under the spectra represent various species assumed to exist. The results are summarized in* ***Tables 11*** *and* ***12****, respectively. Dashed vertical line denotes the position of the same peak in the parent MAX phase.*

O 1s region

The O 1s regions of un-sputtered $Mo_2TiC_2T_x$ (***Figure 44.*****a**) and $Mo_2Ti_2C_3T_x$ (**Figure 44.b**) samples were fit by the same components, listed in **Tables 11** and **12**, respectively. These components correspond to C-Mo-O_x, C-Mo-$(OH)_x$ and H_2O_{ads}. These species comprise ≈ 60% of the O 1s region photoemission for $Mo_2TiC_2T_x$ and ≈ 50.2% for $Mo_2Ti_2C_3T_x$. The remainder of the spectra is fit by a component corresponding to molybdenum and/or titanium oxides arising from surface oxidation [105,120,149]. Surface organic contaminations of C-O, and COO contributions to this region, which overlaps with, and obscures, many other peaks. The amounts of these organic contaminations for $Mo_2TiC_2T_x$ and $Mo_2Ti_2C_3T_x$ samples are 6.4 and 5.8 at. %, respectively.

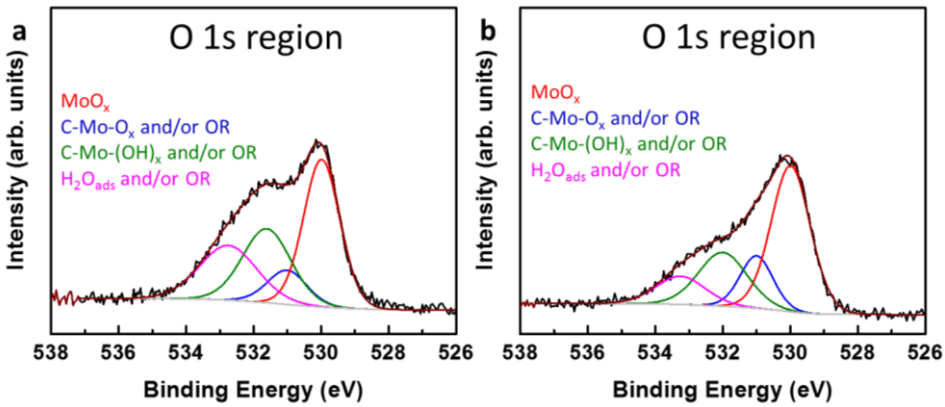

Figure 44. *Component peak fitting of XPS spectra of O 1s region for un-sputtered, a) ML $Mo_2TiC_2T_x$-50HF and b) ML $Mo_2Ti_2C_3T_x$-50HF cold pressed disks. The various peaks under the spectra represent various species assumed to exist. The results are summarized in* ***Tables 11*** *and* ***12****, respectively.*

F 1s region

The F 1s regions of pre-sputtered $Mo_2TiC_2T_x$ (**Figure 45.a**) and $Mo_2Ti_2C_3T_x$ (**Figure 45.b**) samples were fit by the same component, listed in **Tables 11** and **12**, respectively. This component corresponds to C-Mo-F_x. The peak assigned to C-Mo-F_x sits at a BE of 685.3 and 684.0 eV for $Mo_2TiC_2T_x$ and $Mo_2Ti_2C_3T_x$, respectively.

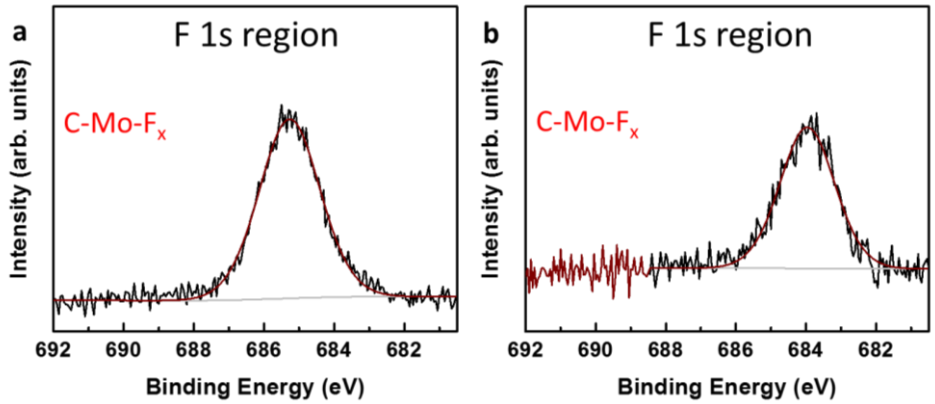

Figure 45. *Component peak fitting of XPS spectra of F 1s region for un-sputtered, a) ML $Mo_2TiC_2T_x$-50HF and b) ML $Mo_2Ti_2C_3T_x$-50HF cold pressed disks. The various peaks under the spectra represent various species assumed to exist. The results are summarized in* ***Tables 11*** *and* ***12****, respectively.*

Table 11. *XPS peak fitting results for un-sputtered ML $Mo_2TiC_2T_x$-50HF cold pressed disk. The numbers in parenthesis in column 2 for the Mo 3d and Ti 2pregions are peak locations of* $Mo3d_{3/2}$ and Ti $2p_{1/2}$, respectively; *their respective FWHMs are listed in column 3 in parenthesis.*

Region	BE [eV][a]	FWHM [eV][a]	Fraction	Assigned to	Reference
Mo $3d_{5/2}$ ($3d_{3/2}$)	228.2 (231.4)	0.9 (1.2)	0.16	Mo_2C bulk carbide	[151]
	229.3 (232.5)	0.8 (1.1)	0.72	C-Mo-T_x	[148]
	231.5 (234.5)	1.5 (1.3)	0.08	Mo^{+5}	[149]
	232.7 (235.7)	1.5 (1.2)	0.04	Mo^{+6}	[149]
Ti $2p_{3/2}$ ($2p_{1/2}$)	454.8 (459.9)	1.0 (1.7)	0.30	Ti-C	[123]
	455.7 (461.2)	1.4 (2.0)	0.37	Ti^{+2}-C	[123]
	457.2 (462.9)	1.7 (1.8)	0.22	Ti^{+3}-C	[120,121]
	459.3 (464.9)	1.9 (2.5)	0.11	TiO_2	[122]
C 1s	282.5	1.0	0.24	C-Mo/Ti-T_x	[123,124,148]
	284.7	1.4	0.57	C-C	[127]
	285.4	1.4	0.06	CH_x	[127]
	286.2	1.4	0.10	C-O	[127]
	288.8	1.8	0.03	COO	[127]
O 1s	530.0	1.3	0.39	MoO_x and/or TiO_2	[149]
	531.0	1.4	0.20	C-Mo-O_x[b]	[114]
	531.6	1.7	0.14	C-Mo-$(OH)_x$ and/or OR[b]	[114]
	532.8	2.0	0.27	H_2O_{ads} (IV) and/or OR[b]	[114]
F 1s	685.3	2.0	1.0	C-Mo-F_x	[150]

[a] Values in parenthesis corresponds to the $3d_{3/2}$ and $2p_{1/2}$ components.
[b] OR stands for organic compounds due to atmospheric surface contaminations.

Table 12. *XPS peak fitting results for un-sputtered ML $Mo_2Ti_2C_3T_x$-50HF cold pressed disk. The numbers in parenthesis in column 2 for the Mo 3d and Ti 2pregions are peak locations of* $Mo3d_{3/2}$ and Ti $2p_{1/2}$, respectively; *their respective FWHMs are listed in column 3 in parenthesis.*

Region	BE [eV][a]	FWHM [eV][a]	Fraction	Assigned to	Reference
Mo $3d_{5/2}$ ($3d_{3/2}$)	229.0 (232.1)	0.8 (1.6)	0.52	C-Mo-T_x	[148]
	230.2 (233.2)	2.1 (1.7)	0.28	Mo^{+5}	[149]
	232.2 (235.7)	1.0 (2.0)	0.02	Mo^{+6}	[149]
Ti 2p	454.8 (461.0)	0.9 (1.6)	0.45	Ti-C	[123]
	455.7 (461.2)	1.6 (2.0)	0.29	Ti^{+2}-C	[123]
	457.3 (463.0)	1.5 (1.5)	0.11	Ti^{+3}-C	[120,121]
	459.3 (464.9)	2.3 (2.5)	0.15	TiO_2	[122]
C 1s	281.9	0.8	0.11	C-Ti	[123,124]
	282.5	0.9	0.22	C-Ti/Mo-T_x	[123,124,148]
	284.6	1.0	0.46	C-C	[127]
	285.3	1.4	0.07	CHx	[127]
	286.2	1.4	0.09	C-O	[127]
	288.6	2.0	0.06	COO	[127]
O 1s	530.0	1.2	0.50	MoO_x and/or TiO_2	[149,105,120]
	531.0	1.2	0.15	C-Mo-O_x[b]	[105,128,114]
	532.0	1.7	0.23	C-Mo-$(OH)_x$ and/or OR[b]	[105,128,114
	533.3	1.8	0.12	H_2O_{ads} (IV) and/or OR[b]	[105,128,114
F 1s	684.0	1.8	1.0	C-Mo-F_x	[150]

[a] Values in parenthesis corresponds to the $2p_{1/2}$ component.
[b] OR stands for organic compounds due to atmospheric surface contaminations.

4.2 Obtaining the chemical formulae for MXenes

In order to obtain the chemical formulae for MXenes, first the various species in MXene have to be identified and quantified through peak fitting of the high-resolution spectra the regions. **Table 13** summarizes the species in each region that belong to each MXene. The atomic % of each species is determined by multiplying that species' areal fraction of the photoemission in the high-resolution region of an element by the overall atomic percentage of the same element. The global atomic percentages can be found in **Table 14**. To illustrate: the atomic percentage of the species C-Ti-T_x in the C 1s region for $Ti_3C_2T_x$ should give the total atomic percentage of C in $Ti_3C_2T_x$. The area fraction of that species in the C 1s region, is 0.54 (row 2 in **Table 4**), and the

total atomic percentage of C in that sample is 29.4 at.%. Thus the atomic percentage of the C-Ti-T_x species in $Ti_3C_2T_x$ is ≈ 15.9 at.%. The error range in the atomic percentage for all species is less than 10%. The chemical formulae of all MXenes discussed in Section 4.1 are listed found in **Table 15**. It is important to note that most of the MXenes' chemical formulae were normalized assuming full occupancy of the M-sites. In case of $Mo_2TiC_2T_x$ and $Mo_2Ti_2C_3T_x$, the formulae were normalized to stoichiometry of the Mo element. It is important to appreciate that theoretically if every surface M atoms is bonded to an OH and/or and F then x should be 2. Therefore, if the number of M atoms is < 2, then x would be > 2. Values of x > 2 are difficult to rationalize. For that reason, cases where M:X ratio is lower the stoichiometric value, the compound was normalized to the stoichiometry of the C element to show deficiency in the M element.

Table 13. Summary of elemental global at .% - including non-MXene entities – before sputtering.

	Ti 2p	Nb 3d	V 2p	Mo 3d	C 1s	O 1s	F 1s	N 1s
$Ti_3C_2T_x$	(OH and/or O-Ti-C) (OH and/or O-Ti^{+2}-C) (OH and/or O-Ti^{+3}-C)				C-Ti-T_x	C-Ti-O_x C-Ti-$(OH)_x$ H_2O_{ads}	C-Ti-F_x	
Ti_2CT_x	(OH and/or O-Ti-C) (OH and/or O-Ti^{+2}-C) (OH and/or O-Ti^{+3}-C)				C-Ti-T_x	C-Ti-O_x C-Ti-$(OH)_x$ H_2O_{ads}	C-Ti-F_x	
Ti_3CNT_x	(OH and/or O-Ti-CN) (OH and/or O-Ti^{+2}-CN) (OH and/or O-Ti^{+3}-CN)				C-Ti-T_x	CN-Ti-O_x CN-Ti-$(OH)_x$ H_2O_{ads}	CN-Ti-F_x	NC-Ti-T_x
Nb_2CT_x		(OH and/or O)-Nb-C F-Nb-C			C-Nb-T_x	C-Nb-O_x C-Nb-$(OH)_x$ H_2O_{ads}	C-Nb-F_x	
$Nb_4C_3T_x$		Nb-C (OH and/or O)-Nb-C F-Nb-C			C-Nb C-Nb-T_x	C-Nb-O_x C-Nb-$(OH)_x$ H_2O_{ads}	C-Nb-F_x	
V_2CT_x			C-V-T_x		C-V-T_x	C-V-O_x C-V-$(OH)_x$ H_2O_{ads}	C-V-F_x	
Mo_2CT_x			C-Mo-T_x		C-Mo-T_x	C-V-O_x C-V-$(OH)_x$ H_2O_{ads}	C-V-F_x	
$Mo_2TiC_2T_x$	(Ti-C) (Ti^{+2}-C) (Ti^{+3}-C)		C-Mo-T_x		C-Mo/Ti-T_x	C-Mo-O_x C-Mo -$(OH)_x$ H_2O_{ads}	C-Mo-F_x	
$Mo_2Ti_2C_3T_x$	(Ti-C) (Ti^{+2}-C) (Ti^{+3}-C)		C-Mo-T_x		C-Ti C-Mo/Ti-T_x	C-Mo-O_x C-Mo-$(OH)_x$ H_2O_{ads}	C-Mo-F_x	

Table 14. *Summary of elemental global at. % - including non-MXene entities – before sputtering.*

	Ti	Nb	V	Mo	C	F	O	Al	N	Ga
$Ti_3C_2T_x$	26.1±0.1				31.4±0.2	25.5±0.2	15.1±0.2	1.9±0.1	< 0.1	
Ti_2CT_x	27.2±0.9				39.4±0.9	13.4±0.6	20.0±0.7	< 0.1	< 0.1	
Ti_3CNT_x	30.6±1.8				29.4±1.1	16.1±0.8	12.1±0.7	< 0.1	11.8±0.6	
Nb_2CT_x		25.0±0.7			31.4±0.9	12.6± 0.6	31.0±0.8	< 0.1	< 0.1	
$Nb_4C_3T_x$		25.3±0.2			55.0±1.0	4.2±0.6	15.5±0.7	< 0.1	< 0.1	
V_2CT_x			30.7±0.4		40.9±0.5	14.1±0.7	21.5±0.3	< 0.1		
Mo_2CT_x				15.6±0.3	63.0±0.9	4.6±0.3	26.0±0.5			< 0.1
$Mo_2TiC_2T_x$	4.8±0.2			17.1±0.6	50.0±1.2	6.2±0.8	21.5±0.6	< 0.1		
$Mo_2Ti_2C_3T_x$	9.7±0.3			24.6±0.2	40.4±0.8	2.8±0.4	22.3±0.7	< 0.1		

Table 15. *Chemical formulae of various MXenes determined from XPS spectra before sputtering.*

M_2XT_x	$M_3X_2T_x$	$M_4X_3T_x$
$Ti_2C_{0.9}O_{0.3}(OH)_{0.5}F_{0.8}.0.4H_2O_{ads}$	$Ti_3C_2O_{0.3}(OH)_{0.32}F_{1.2}.0.3H_2O_{ads.}$	$Nb_4C_{2.6}O_{0.9}(OH)_{1.0}F_{0.7}.0.9H_2O_{ads.}$
$Nb_2CO_{0.8}(OH)_{0.5}F_{0.7}.0.5H_2O_{ads.}$	$Ti_3CNO_{0.23}(OH)_{0.33}F_{1.3}.0.33H_2O_{ads.}$	$Mo_2Ti_{1.5}C_{2.5}O_{0.6}(OH)_{1.0}F_{0.5}.0.5H_2O_{ads.}$
$V_2CO_{0.5}(OH)_{0.2}F_{1.1}.0.2H_2O_{ads.}$	$Mo_2Ti_{0.8}C_2O_{0.4}(OH)_{0.7}F_{1.0}0.5H_2O_{ads.}$	
$Mo_2CT_xO_{0.7}(OH)_{0.4}F_{0.7}.0.3H_2O_{ads.}$		

4.3 Surface terminations and their distributions in MXenes

This section deals with the influence of various parameters - such as MXene chemistry, number of layers (*n*), aging, Ar^+ sputtering and different etchants - on the surface terminations and their distributions. Furthermore, the use of XPS to obtain information regarding the effects of treating of MXenes with various chemicals - such as bases like NaOH and KOH and metal ion salts such as RbCl and NaCl – on the distribution of the surface termination groups is described and analyzed.

4.3.1 Effect of M, and X elements and n

Influence of M in M_2XT_x

The molar ratios of the various surface termination species (-O, -OH, and, -F) and $H_2O_{ads.}$ per M_2XT_x formula unit for Ti_2CT_x, V_2T_x, Nb_2CT_x and Mo_2T_x multilayered HF-etched MXenes are shown in **Figure 46**. As a primary observation, the total sum of molar ratios of all the surface terminations for the four MXenes is either less than or equal to 2. For Ti_2CT_x and Mo_2CT_x those numbers - 1.6 and 1.8, respectively - are < 2; for V_2CT_x and Nb_2CT_x that number is exactly 2. This suggests that in the cases of Ti_2CT_x and Mo_2CT_x, there might be some deficiency in the M sites. In the Ti_2CT_x case,

the deficiency is of the order of 20%, implying that the actual composition of this MXene is $Ti_{1.6}CT_x$ and not Ti_2CT_x. Similarly, the deficiency in Mo_2CT_x is of the order of 10 %, i.e. the actual composition is $Mo_{1.9}CT_x$. It is worth noting that for Mo_2CT_x the percentage of deficiency in the Mo atoms assumed is within the margin of error for the XPS fitting and analysis. However, for Ti_2CT_x, the reason for that the XPS results do not show deficiency is not understood and more work is needed regarding that matter.

Karlsson *et al*. [98] have shown, through HRSTEM, the existence of Ti vacancies in single flakes of $Ti_3C_2T_x$. Looking at the surface termination distribution of the M_2XT_x MXenes, Nb_2CT_x has the highest O:F surface termination ratio of 1.14, next is Mo_2CT_x where the ratio of is 1.0. For V_2CT_x, that ratio is 0.5. The lowest O:F ratio – 0.4 – is observed in Ti_2CT_x.

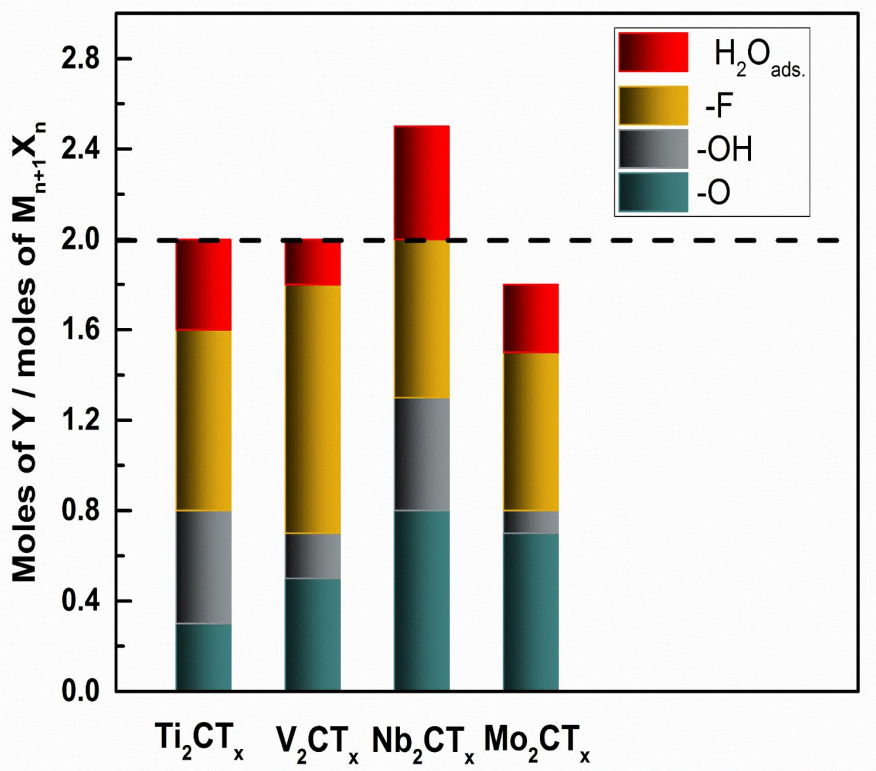

Figure 46. *Moles of Y per M_2XT_x formula unit for $Ti_2C_{0.9}O_{0.3}(OH)_{0.5}F_{0.8}.0.4H_2O_{ads.}$, $Nb_2CO_{0.8}(OH)_{0.5}F_{0.7}.0.5H_2O_{ads.}$, $V_2CO_{0.5}(OH)_{0.2}F_{1.1}.0.2H_2O_{ads.}$, and $Mo_2CT_xO_{0.7}(OH)_{0.4}F_{0.7}.0.3H_2O_{ads.}$. Y includes the terminations and adsorbed H_2O. Note that if one termination is assumed per surface M atom, then in all cases the theoretical T_x number per formula unit is 2 given by the horizontal dashed line. This is the case because only the sum of the moles of O, OH and F constitutes the terminations.*

Influence of the M in $M_3X_2T_x$

Figure 47 compares the molar ratios for the various surface terminations species (-O, -OH, and, -F) and $H_2O_{ads.}$ per $M_3X_2T_x$ formula unit for $Ti_3C_2T_x$ and $Mo_2TiC_2T_x$. The values of x for $Ti_3C_2T_x$ and $Mo_2TiC_2T_x$ are 1.8 and 1.9, respectively. Here again there may be a small deficiency in surface M sites. Note that the actual chemistry of $Mo_2TiC_2T_x$ is $Mo_2Ti_{0.8}C_2T_x$ (**Table 15**). Given that it is easier to convert Ti_3AlC_2 (18 h at RT) than to Its MXene than Mo_2TiAlC_2 (4 d at 55 °C) of etching, it is not unreasonable to assume that the harsher etching conditions resulted in the selective dissolution of Ti.

The O:F ratio decreases when the Ti outer layer is replaced with Mo ($Ti_3C_2T_x$ vs. $Mo_2TiC_2T_x$) from 0.25 to 0.18, and the number of moles of -OH termination per unit formula increases from 0.32 to 0.6.

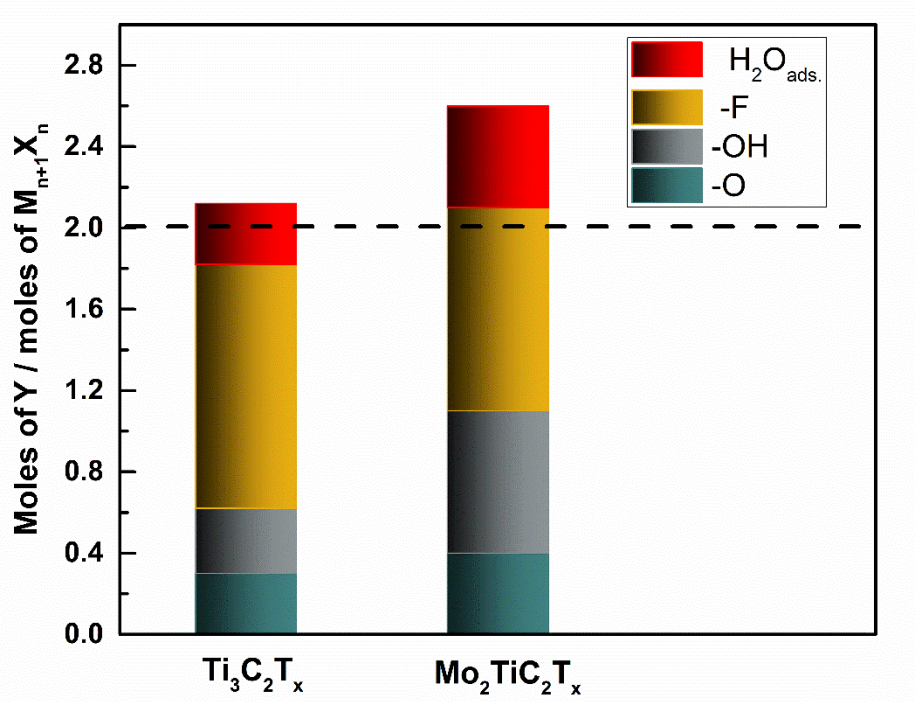

Figure 47. *Moles of Y per $M_3X_2T_x$ formula unit for $Ti_3C_2O_{0.3}(OH)_{0.32}F_{1.2}.0.3H_2O_{ads}$ and $Mo_2Ti_{0.8}C_2O_{0.2}(OH)_{0.6}F_{1.1}.0.5H_2O_{ads.}$. Y includes the terminations and adsorbed H_2O. Note that if one termination is assumed per surface M atom, then in all cases the theoretical T_x number per formula unit is 2 given by the horizontal dashed line. This is the case because only the sum of the moles of O, OH and F constitutes the terminations.*

Influence of the M in $M_4X_3T_x$

Figure 48 compares the molar ratios of the various surface terminations species (-O, -OH, and, -F) and H_2O_{ads} per $M_4X_3T_x$ formula unit for $Nb_4C_3T_x$ and $Mo_2Ti_2C_3T_x$. Both MXenes are C deficient (13 % for $Nb_4C_3T_x$ and 16% for $Mo_2Ti_2C_3T_x$), as shown in **Table 15** Note that deficiency was already present in the parent MAX phases [152, 154].

The total sum of molar ratio of all the surface terminations for $Nb_4C_3T_x$ and $Mo_2Ti_2C_3T_x$ is 2.6 and 2.1, respectively. Both these values exceed the theoretical x-value of 2. The simplest explanation for this unexpected result is that some of the surface termination groups might be occupying the C vacant sites. This comment notwithstanding, it is hereby acknowledged that more systematic work is needed to explain these results. It is important to note, however, that $x > 2$ was only observed when the C in the final MXene was less than stoichiometric.

The O:F ratio is almost the same for $Nb_4C_3T_x$ (1.3) and $Mo_2TiC_2T_x$ (1.2). Interestingly, in both cases the number of OH moles per formula unit is 1.0.

Note that the same arguments made for $Mo_2TiC_2T_x$, can be made for $Mo_2TiC_2T_x$. In the latter case, however, the Ti deficiency is 25% (**Table 15**).

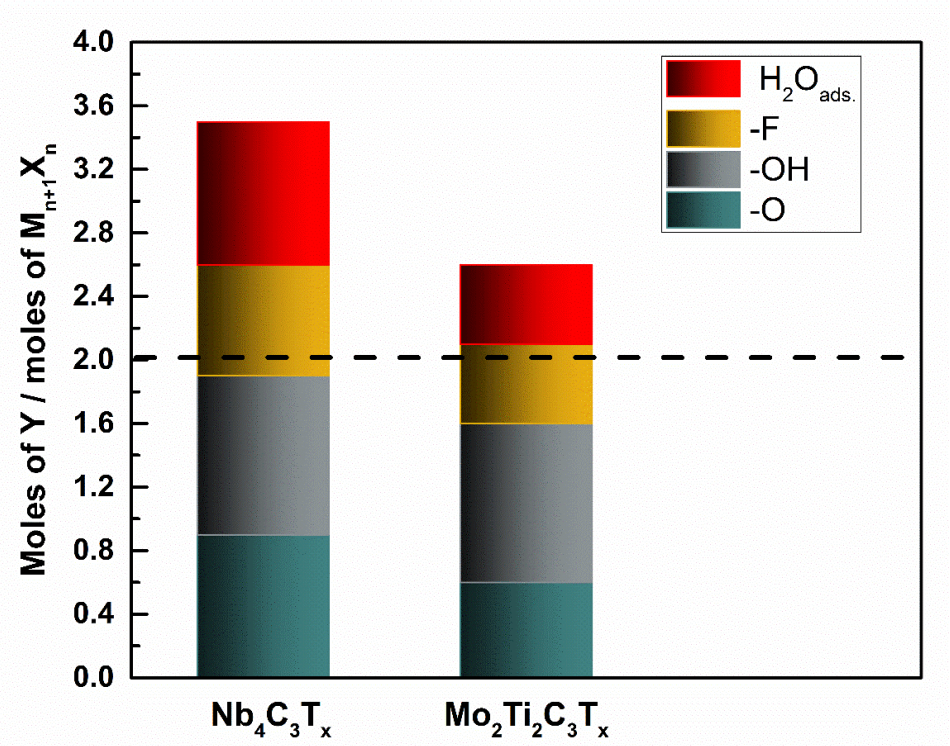

Figure 48. *Moles of Y per $M_4X_3T_x$ formula unit for $Nb_4C_{2.6}O_{0.9}(OH)_{1.0}F_{0.7}.0.9H_2O$ and $Mo_2Ti_{1.5}C_{2.5}O_{0.6}(OH)_{1.0}F_{0.5}.0.5H_2O_{ads}$. Note that if one termination is assumed per surface M atom, then in all cases the theoretical T_x number per formula unit is 2 given by the horizontal dashed line. This is the case because only the sum of the moles of O, OH and F constitutes the terminations.*

4.3.2 Influence of X element in $M_3X_2T_x$

The molar ratios of the various surface termination species (-O, -OH, and, -F) and H_2O_{ads} per $M_3X_2T_x$ formula unit for $Ti_3C_2T_x$ and Ti_3CNT_x multilayered HF-etched MXenes are compared in **Figure 49**. The total sum of molar ratios of all the surface terminations for the two MXenes is almost equal at 1.82 for $Ti_3C_2T_x$ and 1.86 for Ti_3CNT_x. Thus, both MXenes might be slightly M deficient.

The O:F ratio decreases when partially substituting the C atoms with N atoms from 0.25 for $Ti_3C_2T_x$ to 0.18 for Ti_3CNT_x and the number of moles of OH per unit formula is almost the same for for $Ti_3C_2T_x$ (0.32) and Ti_3CNT_x (0.33).

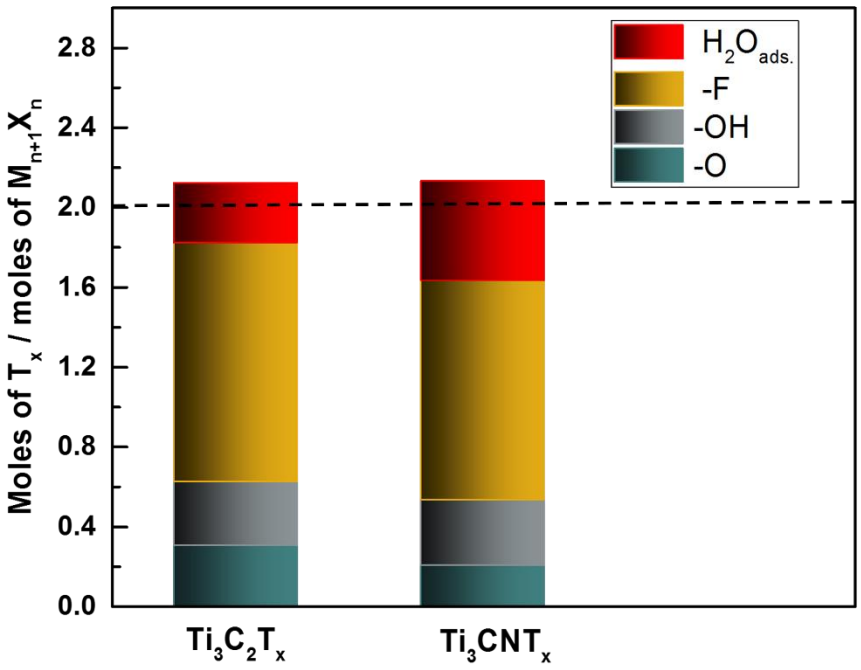

***Figure 49**. Moles of Y per $M_3X_2T_x$ formula unit for $Ti_3C_2O_{0.3}(OH)_{0.32}F_{1.2}.0.3H_2O_{ads}$ and $Ti_3CNO_{0.23}(OH)_{0.33}F_{1.3}.0.33H_2O_{ads}$. Y includes the terminations and adsorbed H_2O. Note that if one termination is assumed per surface M atom, then in all cases the theoretical T_x number per formula unit is 2 given by the horizontal dashed line. This is the case because only the sum of the moles of O, OH and F constitutes the terminations.*

4.3.3 The influence of n

Comparison between Ti_2CT_x and $Ti_3C_2T_x$

The number of moles of the various surface termination species (-O, -OH, and, -F) and H_2O_{ads} per $M_{n+1}X_nT_x$ formula unit as a function of the order of MAX phase, *n*, for Ti_2CT_x and $Ti_3C_2T_x$ multilayered HF-etched MXenes are compared in **Figure 50**. The total sum of molar ratios of all the surface terminations increase – from 1.6 to 1.82 - as n increases from 1 to 2. As discussed previously, that might indicate some deficiency on the Ti atoms sites. This conclusion is consistent with the fact that it is easier to etch Ti_2CT_x than $Ti_3C_2T_x$. In general, Ti_2C is less stable.

The O:F ratio decreases from 1:2.7 to 1.4 – as n increases from 1 to 2. The number of moles of the -OH termination is higher for Ti_2CT_x (0.5) compared to $Ti_3C_2T_x$ (0.32). It is worth noting that there is 10 % C-deficiency in Ti_2CT_x, as shown in **Table 15**, this

might be attributed to loss of C atoms – in the form of amorphous C - while etching. Needless to say the loss of both Ti and C complicates the analysis.

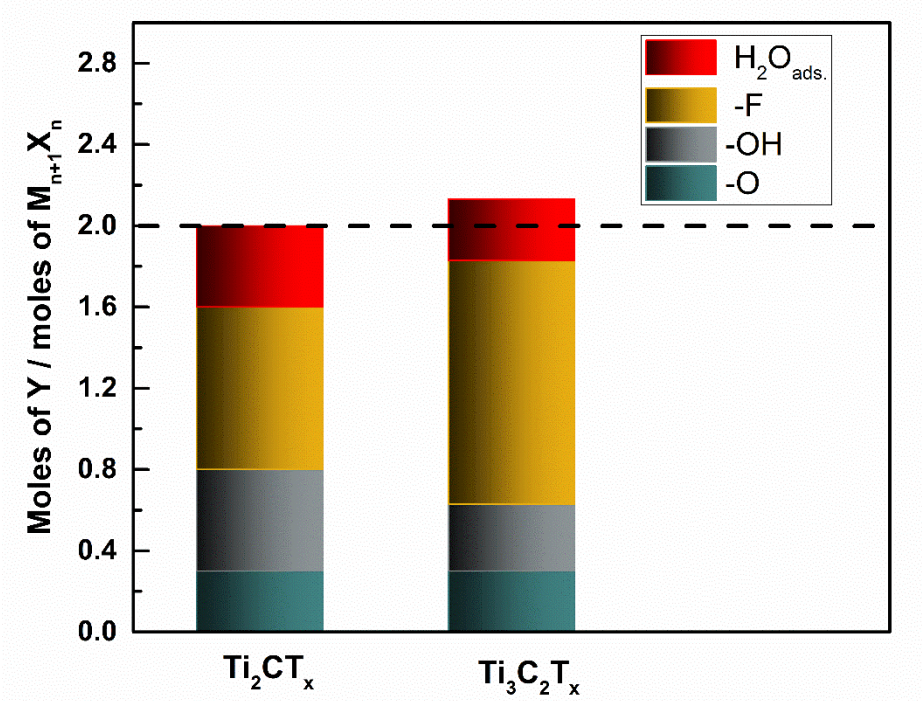

Figure 50. *Moles of Y H_2O per $M_{n+1}X_nT_x$ formula unit for $Ti_2C_{0.9}O_{0.3}(OH)_{0.5}F_{0.8}.0.4H_2O_{ads}$ and $Ti_3C_2O_{0.3}(OH)_{0.32}F_{1.2}.0.3H_2O_{ads}$. Y includes the terminations and adsorbed H_2O. Note that if one termination is assumed per surface M atom, then in all cases the theoretical T_x number per formula unit is 2 given by the horizontal dashed line. This is the case because only the sum of the moles of O, OH and F constitutes the terminations.*

Comparison between Nb_2CT_x and $Nb_4C_3T_x$.

The molar ratios of the various surface termination species (-O, -OH, and, -F) and H_2O_{ads} per $M_{n+1}X_nT_x$ formula unit as a function of *n*, for Nb_2CT_x and $Nb_4C_3T_x$ multilayered HF-etched MXenes are compared in **Figure 51**. The total sum of mole ratios of all the surface terminations increases as *n* increases from 1 to 3, for Nb_2CT_x, it is 2.0 and for $Nb_4C_3T_x$, it is 2.6.

The O:F ratio decreases when *n* increases from 1 to 3. For Nb_2CT_x, the O:F ratio is 1.1, and for $Nb_4C_3T_x$ the ratio is 1.3 in contrast to Ti_2CT_x and $Ti_3C_2T_x$. The number of moles of -OH termination per unit formula is lower for Nb_2CT_x (0.5) compared to $Nb_4C_3T_x$ (1.0) which is in contrast with Ti_2CT_x and $Ti_3C_2T_x$.

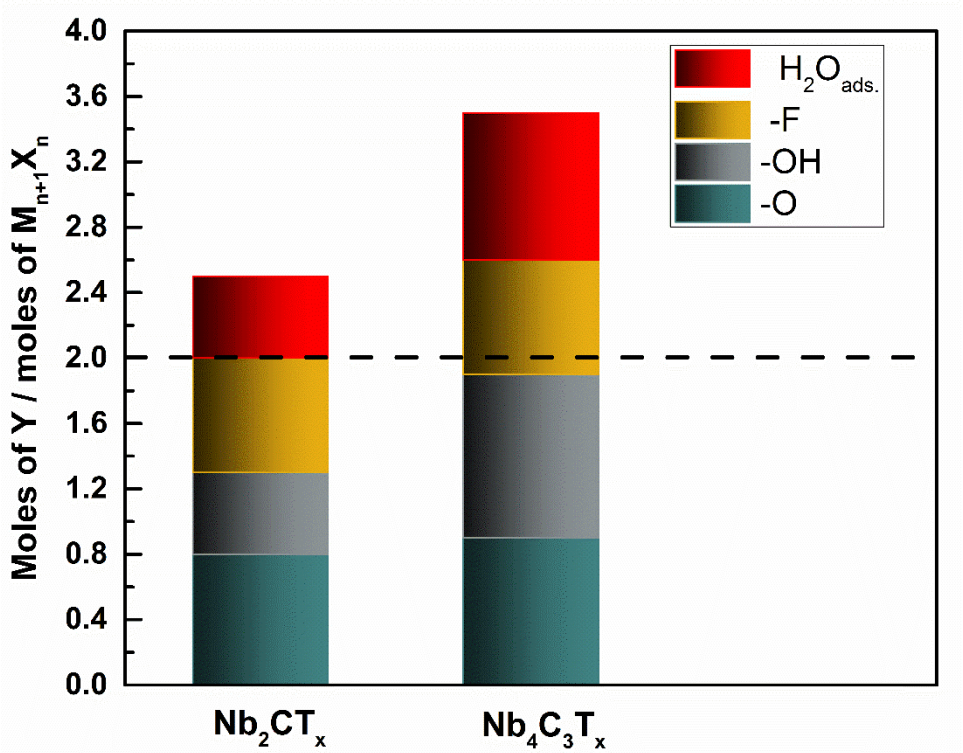

Figure 51. *Moles of Y per $M_{n+1}X_nT_x$ formula unit for $Nb_2CO_{0.8}(OH)_{0.5}F_{0.7}.0.5H_2O_{ads.}$ and $Nb_4C_{2.6}O_{0.9}(OH)_{1.0}F_{0.7}.0.9H_2O$. Y includes the terminations and adsorbed H_2O. Note that if one termination is assumed per surface M atom, then in all cases the theoretical T_x number per formula unit is 2 given by the horizontal dashed line. This is the case because only the sum of the moles of O, OH and F constitutes the terminations.*

Comparison between $Mo_2TiC_2T_x$ and $Mo_2Ti_2C_3T_x$

The molar ratios of the various surface terminations (-O, -OH, and, -F) and $H_2O_{ads.}$ per $M_{n+1}X_nT_x$ formula unit as a function of *n* for $Mo_2TiC_2T_x$ and $Mo_2Ti_2C_3T_x$ multilayered HF-etched MXenes are compared in **Figure 52**. The total sum of molar ratios of all the surface terminations increases as *n* increases from 2 to 3, for $Mo_2TiC_2T_x$, it is 1.9 and for $Mo_2Ti_2C_3T_x$, it is 2.1.

The O:F ratio increases significantly when *n* increases from 2 to 3, for $Mo_2TiC_2T_x$, the O:F ratio is 0.4 and for $Mo_2Ti_2C_3T_x$ the ratio is 1.2 similar to Nb_2CT_x and $Nb_4C_3T_x$ and in contrast to Ti_2CT_x and $Ti_3C_2T_x$, and. The number of moles of the -OH termination per unit formula is lower for $Mo_2TiC_2T_x$ (0.6) compared to $Mo_2Ti_2C_3T_x$

(1.0) which is in agreement with Nb_2CT_x and $Nb_4C_3T_x$ but in contrast with Ti_2CT_x and $Ti_3C_2T_x$.

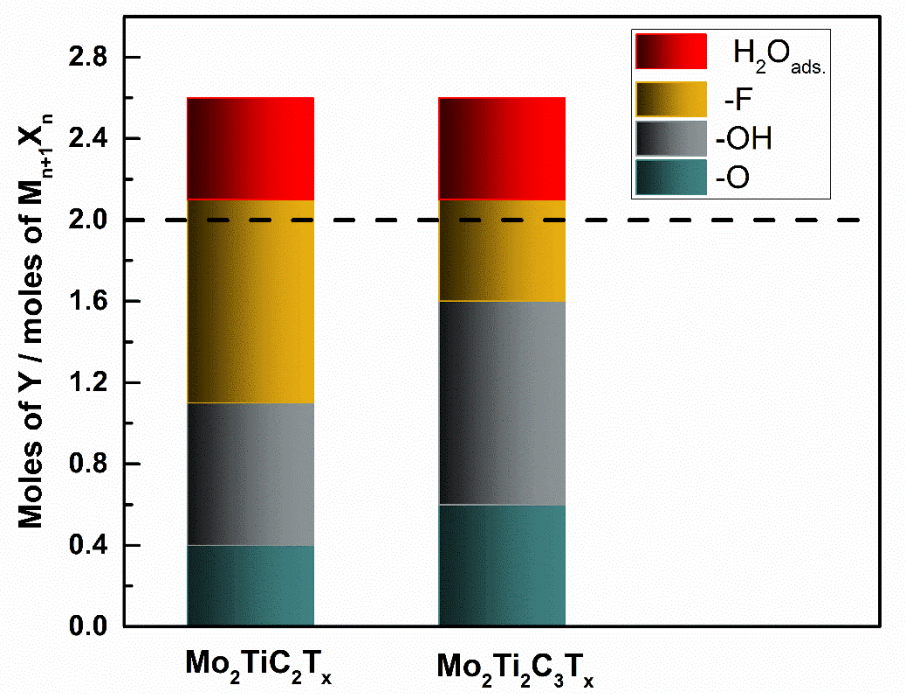

Figure 52. *Moles of Y per $M_{n+1}X_nT_x$ formula unit for $Mo_2Ti_{0.8}C_2O_{0.4}(OH)_{0.7}F_{1.0}0.5H_2O_{ads.}$ and $Mo_2Ti_{1.5}C_{2.5}O_{0.6}(OH)_{1.0}F_{0.5}.0.5H_2O_{ads.}$. Note that if one termination is assumed per surface M atom, then in all cases the theoretical T_x number per formula unit is 2 given by the horizontal dashed line. This is the case because only the sum of the moles of O, OH and F constitutes the terminations.*

To sum up this section, no general trends were found regarding the influence of M, and X elements or *n* on the distributions of the surface terminations. This might be due to the fact that the etching conditions for producing each MXene, with respect to: i) Duration of etching, ii) Concentration of the etchant and, iii) Temperature of the etching times, are different. This difference comes from the different M-A binding energy which affects the etching conditions [[155]]. For example, **Figure 53** shows no obvious trend for the moles per formula unit of -F terminations in MXenes as a function of the product of the etchant concentration and etching time. Having said that, reporting the actual surface terminations and their distributions for the various MXenes is essential for selecting the suitable MXene for a certain application.

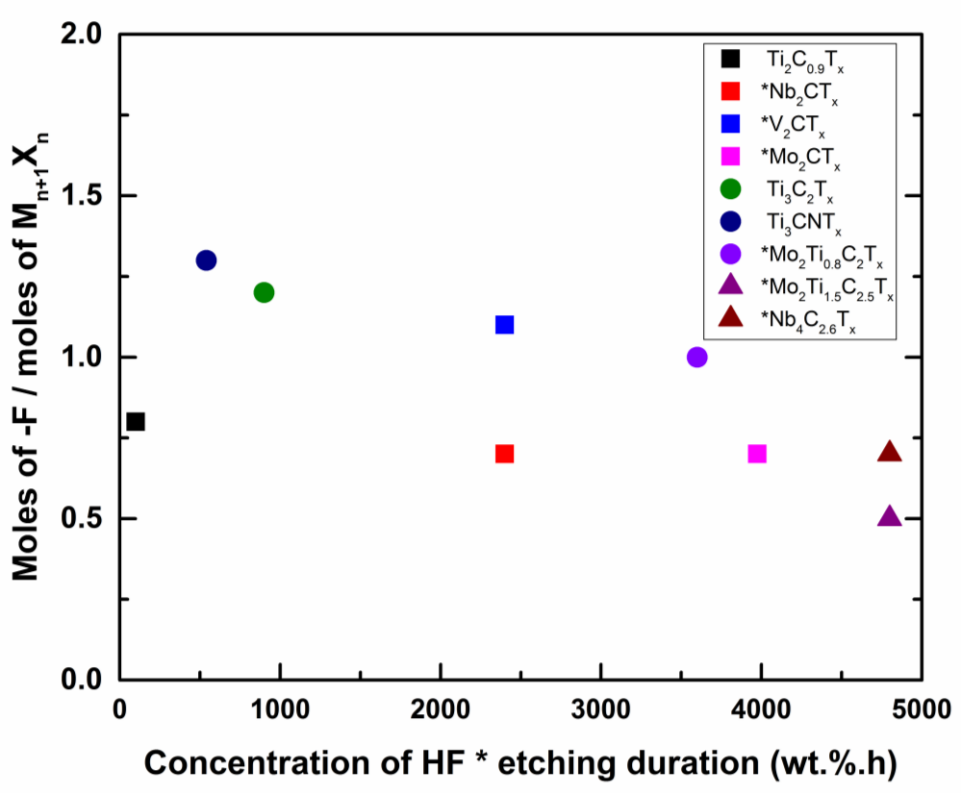

Figure 53. *Moles of -F terminations per formula unit of $M_{n+1}X_n$ as a function of the product of the HF concentration and the etching duration for all HF etched MXenes.*

4.3.4 Influence of Ar^+ sputtering of $Ti_3C_2T_x$

The moles of C and moles of the various surface terminations species (-O, -OH, and, -F) – per formula unit – in $Ti_3C_2T_x$ multilayered HF-etched MXene before and after Ar^+ sputtering are plotted in **Figure 54**. The derived formulae before and after sputtering for $Ti_3C_2T_x$ are: $[Ti_3C_2O_{0.3}(OH)_{0.32}F_{1.2}.0.3H_2O_{ads.}]$ and $[Ti_3C_{1.8}O_{0.6}(OH)_{0.4}F_{0.8}.0.1H_2O_{ads.}]$, respectively. From these results it is obvious that the M:X ratio has increased from 3:2 to 3:1.8, which is due to Ar^+ ion beam damage, selectively sputtering C atoms from the lattice. This is a commonly observed phenomenon for transition metal carbides [156].

The Ar^+ sputtering causes a change in the distributions of the surface terminations. The O:F ratio increases significantly after Ar^+ sputering of $Ti_3C_2T_x$ from 0.25 to 0.75. Whether the entirety of the increase in O:F is due to preferential –F

sputtering, or has some contribution from a decreased concentration of –F on the interior of the MXenes is unclear. The moles of –OH terminations per formula unit increases from 0.32 before sputtering to 0.4 after sputtering. The moles of $H_2O_{ads.}$ Per formula uint decreases significantly upon sputtering from 0.3 to 0.1.

Similar trends of C deficiency and alteration of the surface terminations species due to Ar^+ sputtering was observed for other MXenes as well [114]. Thus in order to obtain a realistic quantification of the various species in MXenes it is highly recommended to avoid Ar^+ sputtering.

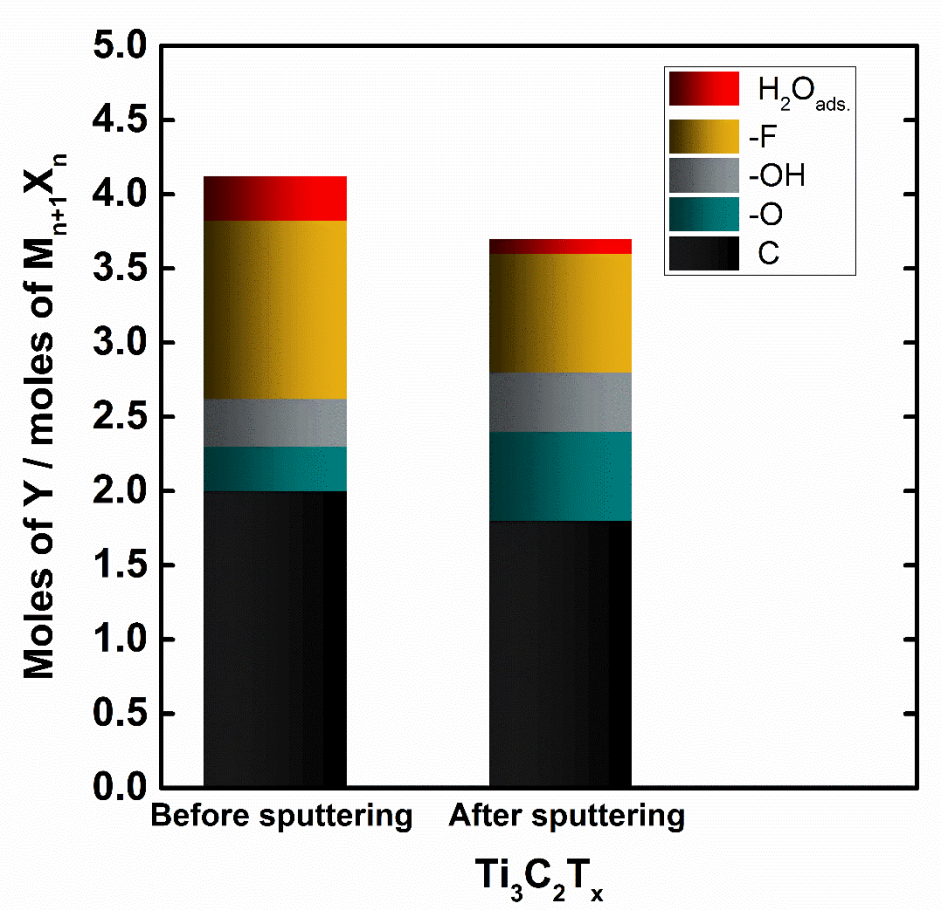

Figure 54. *Moles of Y per $Ti_3C_2T_x$ formula unit, before, and after, Ar^+ sputtering. Y includes the C atoms, terminations and adsorbed H_2O.*

4.3.5 Influence of aging of $Ti_3C_2T_x$

The effect of aging on the $Ti_3C_2T_x$ cold-pressed sample where the XPS spectra was measured within < 1 h after synthesis and after roughly 1 year of being left in the

ambient is demonstrated in **Figures 55** and **56**. The molar percentage of $Ti_3C_2T_x$ in the samples decreases upon aging from 95% to 51.7% as shown in **Figure 55.a** and **b**, respectively. Concomitantly, the Ti-oxides and oxyfluorides mole percentage increase from 5% to 48.3%.

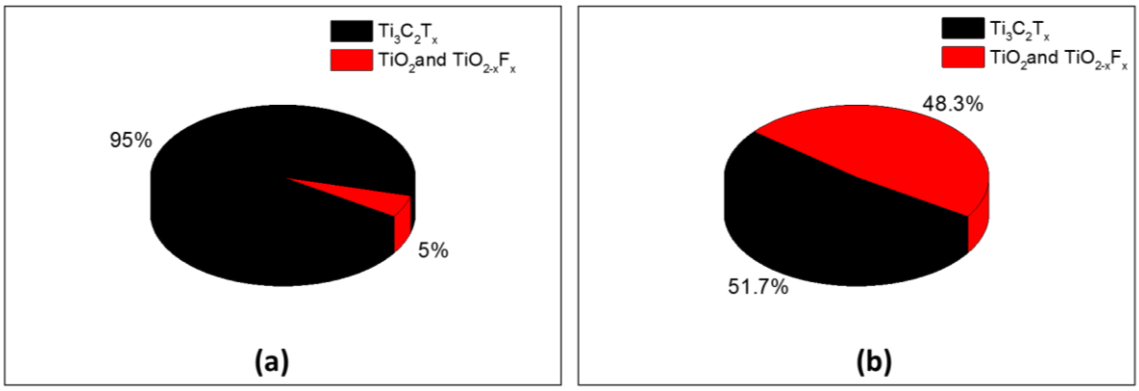

Figure 55. *Molar percentage of $Ti_3C_2T_x$ MXene and Ti oxides and oxyfluorides present in, (a) as-prepared $Ti_3C_2T_x$, and (b) aged $Ti_3C_2T_x$ cold pressed samples before sputtering.*

Accurately quantifying the various species that belong in the aged $Ti_3C_2T_x$ sample was not possible due to the large amounts of surface contaminations obscuring the relevant peaks. In order to compare the surface terminations changes in $Ti_3C_2T_x$ sample due to aging, sputtering was essential to remove most of the organic contaminations. However as noted above, sputtering is not recommended.

Nevertheless, **Figure 56** shows the moles per formula unit of the various surface termination species before and after aging for $Ti_3C_2T_x$. The chemical formulae for the pre-sputtered samples before and after aging are: $[Ti_3C_{1.8}O_{0.6}(OH)_{0.4}(OH\text{-}H_2O_{ads})_{0.1}F_{0.8}.0.1H_2O_{ads.}]$ and $[Ti_3C_{1.8}O_{0.6}(OH)_{0.9}(OH\text{-}H_2O_{ads})_{0.5}F_{0.3}.0.5H_2O_{ads.}]$. The moles of –F terminations per formula unit is reduced from 0.8 to 0.3 after aging. Concomitantly, the amount of –OH terminations is increased from 0.4 to 0.9 after aging. When viewed from a stoichiometric perspective, the M:O ratio (with the O content derived from the sum of the species: -O, and -OH) increases for $Ti_3C_2T_x$ as it ages.

These results indicate that as $Ti_3C_2T_x$ ages, its surface chemistry changes as –F groups are replaced by –OH and –O groups. This indicates that oxidation MXenes begins from the surface terminations, specifically on the -F terminated regions as they are the least stable compared to the O based terminations as predicted theoretically by Xie *et al.* [57]. Similar trends occur for all of the MXenes, though again, some show to be more prone to oxidation than others [114].

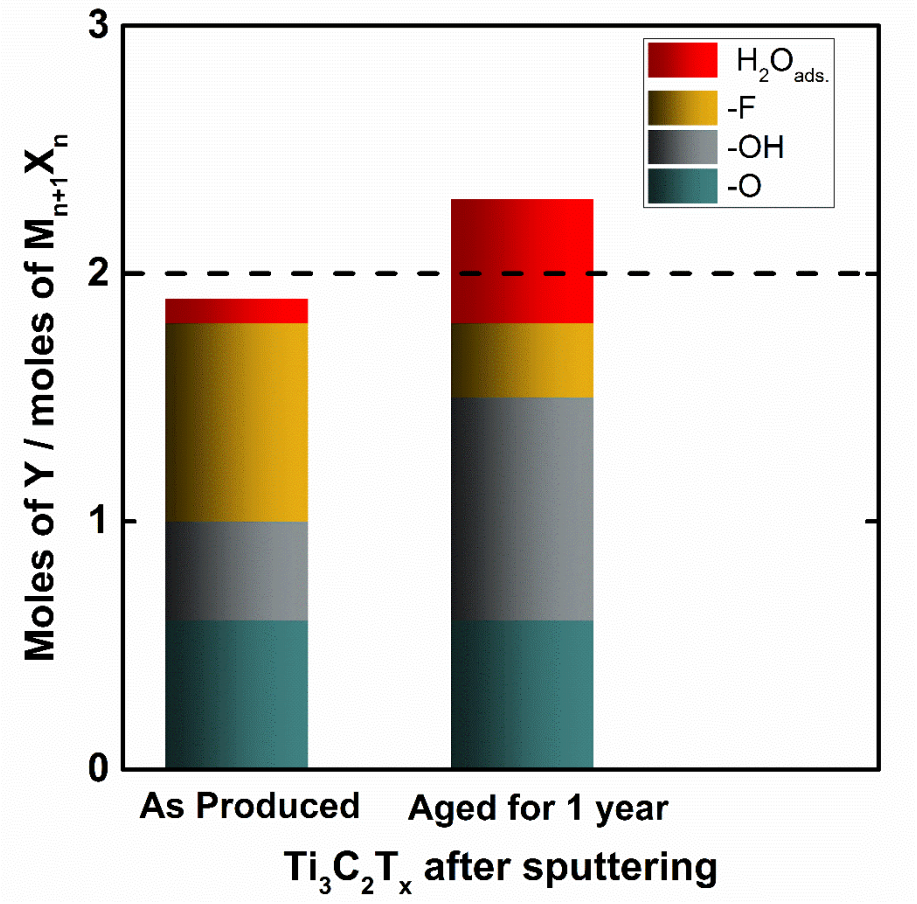

Figure 56. *Moles of Y per per $M_3X_2T_x$ formula unit for $Ti_3C_2T_x$ as produced and after aging for ≈ 1 year after sputtering. Y includes the terminations and adsorbed H_2O. Note that if one termination is assumed per surface M atom, then in all cases the theoretical T_x number per formula unit is 2 given by the horizontal dashed line. This is the case because only the sum of the moles of O, OH and F constitutes the terminations.*

Combined with the observation that sputtering decreases the amount of oxides, it is possible to illustrate the overall framework of the aged $Ti_3C_2T_x$ samples, wherein the center of a MXene ML is unaffected, while its surface is slowly oxidized. The latter

is then coated or surrounded by a C-film. The C film is probably present as a by-product of the oxidation process and likely helps to maintain conductive contact between MXene particles. The comparison between as-prepared and aged samples demonstrates that the use of MXene shortly after synthesis greatly reduces the fraction of oxides and adventitious C present.

4.3.6 Influence of etchants used to produce $Ti_3C_2T_x$

Several methods have been explored to selectively etch the A layers from the MAX phases converting them to MXenes. All of these methods have two things in common: a highly acidic solution and the presence of fluorine ions. But the produced MXenes behave differently. For instance, $Ti_3C_2T_x$ produced by 50 wt.% HF etching of Ti_3AlC_2 needs to be further intercalated with dimethyl sulfoxide, DMSO, in order to be delaminate into un-stacked single flakes [64]. However, after etching Ti_3AlC_2 with LiF + HCl, the produced $Ti_3C_2T_x$ can be delaminated without the need of an intercalant like DMSO [42]. For the above reasons, it is essential to investigate the influence of the various etchants on the distribution of the surface terminations.

The moles per formula unit of the various surface termination species (-O, -OH, and, -F), adsorbed H_2O molecules and Li^+ ions per $Ti_3X_2T_x$ formula unit as a function of the various etchants used: 50 wt. % HF, 10 wt. % HF, LiCl + HF, and LiF + HCl for $Ti_3C_2T_x$ multilayered MXenes are compared in **Figure 57**. Note that in the cases of LiCl + HF and LiF + HCl, there is an additional Li-O and/or Li-OH species that originates from the presence of Li^+ ions interacting with H_2O or with the Ti_3C_2-bound O-containing groups. The XPS analysis for the 10 wt.% HF, LiCl + HF, and LiF + HCl etched $Ti_3C_2T_x$ are represented in the Appendix **Figures 68, 71 and 72,** and **Tables 19, 22, and 23,** respectively. The chemical formulae for the un-sputtered $Ti_3C_2T_x$ samples produced by the following etchants: 50 wt. % HF, 10 wt. % HF, LiCl + HF, and LiF +

HCl are: [$Ti_3C_2O_{0.3}(OH)_{0.32}F_{1.2}.0.3H_2O_{ads}$], [$Ti_3C_2O_{0.5}(OH)_{0.46}F_{1.0}.0.3H_2O_{ads}$], [0.3Li-$Ti_3C_2O_{0.6}(OH)_{0.48}F_{0.8}.0.4H_2O_{ads}$], and [0.3Li-$Ti_3C_2O_{0.4}(OH)_{0.5}F_{0.9}.0.45H_2O_{ads.}$], respectively.

Interestingly, the value of x is a weak function of the etchant used. For example, for the etchants, 50 wt. % HF, 10 wt. % HF, LiCl + HF, and LiF + HCl, the values of x are 1.82, 1.96, 1.88, and 1.8, respectively. Similarly, the net negative charges of the surface terminations are almost the same for the different etchants (≈ 2.4) except for the 50 wt. % HF where it decreases to ≈ 2.1.

The O:F ratio, however, increases significantly when decreasing the concentration of HF from 50 wt.% to 10 wt.% from 0.25 to 0.5. The same trend was deduced by Wang *et al.* [101] through modeling the atomic pair distribution function, PDF, for the neutron measurements of the 50% and 10% HF-$Ti_3C_2T_x$ multilayered samples. As for the LiCl + HF and LiF + HCl cases the O:F ratio is 0.75 and 0.4, respectively.

The moles of Li^+ in the Li-$Ti_3C_2T_x$-HF/LiCl and Li-$Ti_3C_2T_x$-HCl/LiF samples is the same and equal to 0.3 moles per unit formula of $Ti_3X_2T_x$.

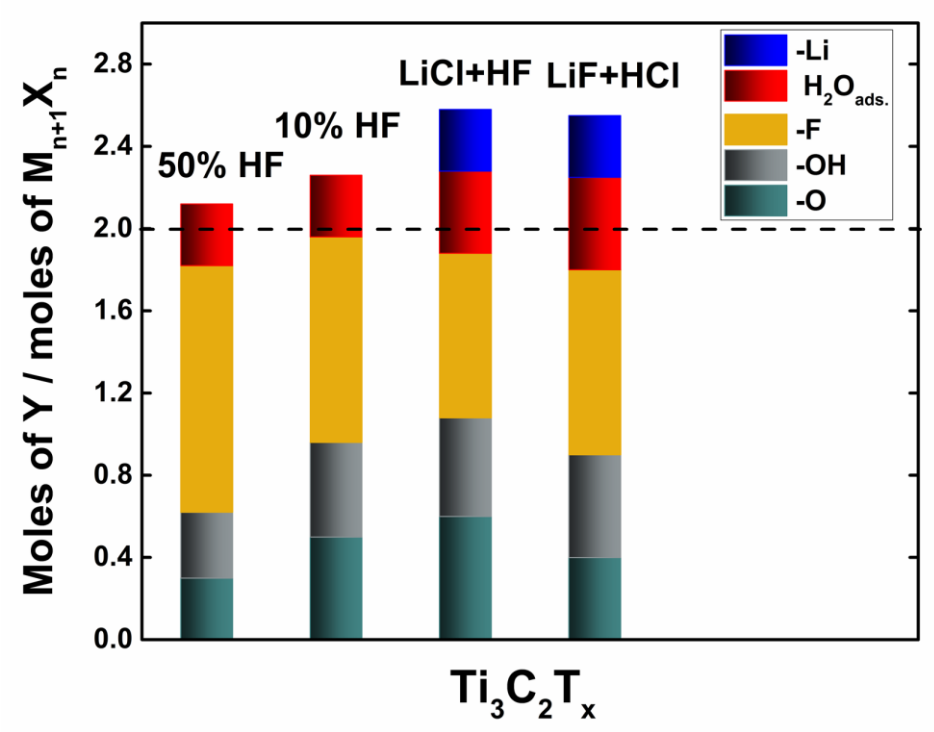

Figure 57: *Moles of Y per $M_3X_2T_x$ formula unit for $Ti_3C_2T_x$ produced using various etchants: 50% HF, 10% HF, LiCl + HCl, and LiF + HCl. Y includes the terminations, Li^+ adsorbed H_2O. Note that if one termination is assumed per surface M atom, then in all cases the theoretical T_x number per formula unit is 2 given by the horizontal dashed line. This is the case because only the sum of the moles of O, OH and F constitutes the terminations.*

4.3.7 Influence of NaOH, and KaOH on multilayered $Ti_3C_2T_x$-50HF

From the XPS analysis of the ML $Ti_3C_2T_x$-50HF samples treated with KOH and NaOH (Appendix: **Figures 69, and 70,** and **Tables 20, and 21,** respectively), the chemical formulae were found to be 0.6K-$Ti_{2.8}C_2O_{0.7}(OH)_{0.61}F_{0.5}.0.4H_2O_{ads}$ and 0.5Na-$Ti_{2.8}C_2O_{0.5}OH_{0.4}F_{0.5}0.3H_2O_{ads}$. The first noticeable observation is the Ti:C ratio which decreases from 1.5 to 1.4. In addition to the decrease in the content of -F surface terminations from 1.2 to 0.5 moles per unit formulae shown in **Figure 58**. The number of moles of -O is constant, however the moles of -OH moles doubled. These observations show a clear modification in the surface terminations when treating $Ti_3C_2T_x$ with base solution such as KOH and NaOH. Dall'Agnese *et al.* [157] showed superior performance in supercapacitors for electrodes made of ML $Ti_3C_2T_x$ after KOH

treatment, when tested in 1M H_2SO_4, it resulted in volumetric capacitance of 215 $F.cm^{-3}$ compared to 98 $F.cm^{-3}$ for untreated ML $Ti_3C_2T_x$ at a scan rate of 2 $mV.s^{-1}$. Moreover, according to DFT theoretical calculations, O- terminated Ti_3C_2 were predicted to show higher capacitance for LIB compareted to F-terminated $Ti_3C_2T_x$ [70]. Thus, these results confirm that it is possible to modify the surface terminations by reducing the -F terminations and subistituting them with -O and -OH terminations through treatment with KOH and NaOH which would enhance the electrochemical properties of MXenes for LIBs and supercapacitors applications.

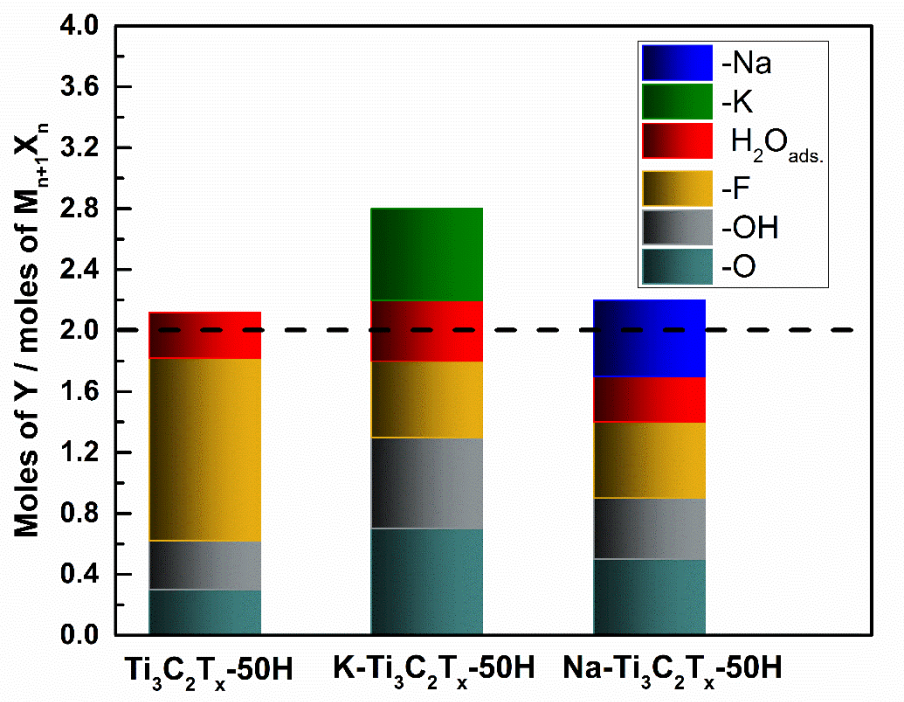

***Figure 58**. Moles of Y per $M_3X_2T_x$ formula unit for $Ti_3C_2T_x$-50HF, $Ti_3C_2T_x$-50HF treated with KOH (K-$Ti_3C_2T_x$-50HF), and NaOH (Na-$Ti_3C_2T_x$-50HF). Y includes the terminations, Na^+, K^+, and adsorbed H_2O. Note that if one termination is assumed per surface M atom, then in all cases the theoretical T_x number per formula unit is 2 given by the horizontal dashed line. This is the case because only the sum of the moles of O, OH and F constitutes the terminations.*

Figures 59.a-c show that the molar percentage of $Ti_3C_2T_x$ is reduced from 95% to 81.3 and 88.8% upon treatment with KOH and NaOH, respectively. Thus, $Ti_3C_2T_x$

oxidizes in basic solutions. A suggested mechanism for this reaction is explained in section 4.5.

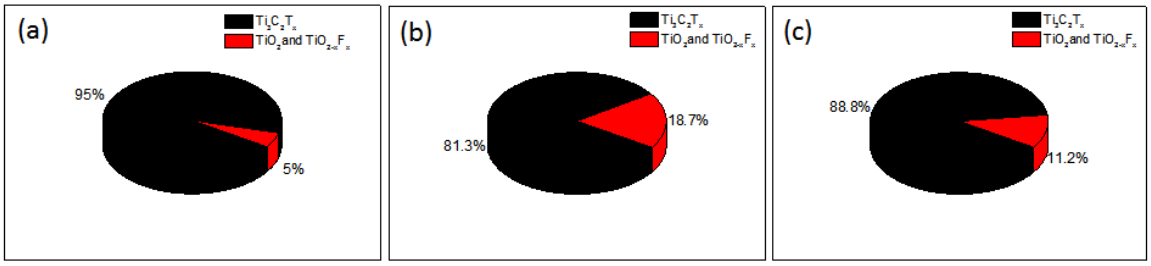

Figure 59. *Molar percentage of $Ti_3C_2T_x$ MXene and Ti oxides and oxyfluorides present in, (a) $Ti_3C_2T_x$-50HF, (b) $Ti_3C_2T_x$-50HF treated with KOH (K-$Ti_3C_2T_x$-50HF), and NaOH (Na-$Ti_3C_2T_x$-50HF) samples.*

4.3.8 Cation exchange in $Ti_3C_2T_x$ MXene

In sections 4.3.6 and 4.3.7, I have shown using XPS that ion intercalation occurs in $Ti_3C_2T_x$. This section investigates the possibility of cation exchange in $Ti_3C_2T_x$ and its detection using XPS. M. Ghidiu tested this idea by immersing ML Li-$Ti_3C_2T_x$-HF/LiCl powders in solutions metal chlorides (NaCl and RbCl) [85], as shown in **Figure 60**, while I investigated their chemistries before, and after, immersion in the metal chloride solutions using XPS technique.

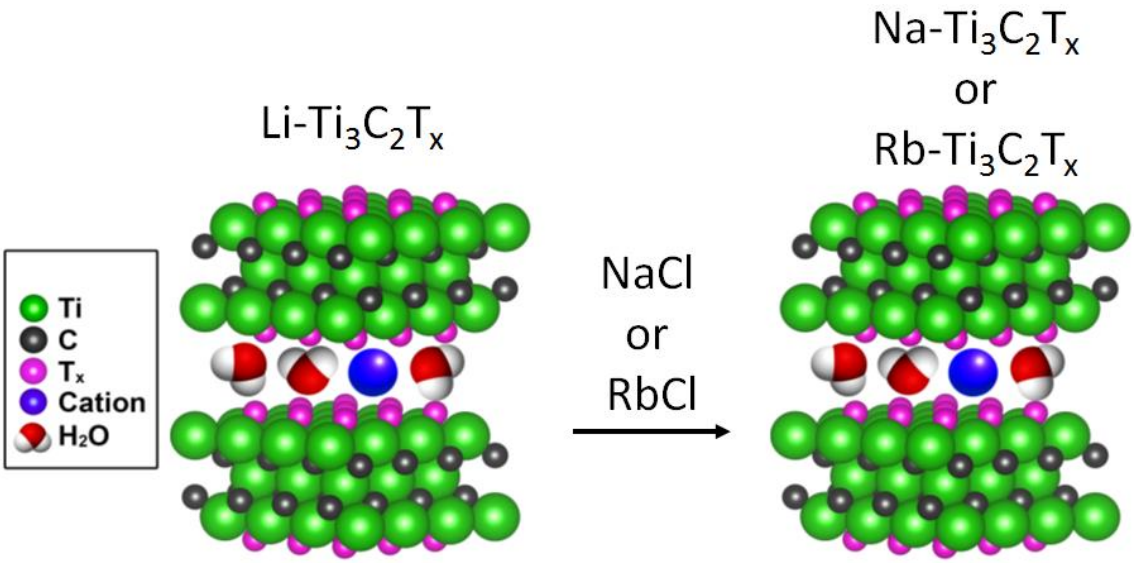

Figure 60. *Schematic showing the exchange of Li^+ ions, in Li-$Ti_3C_2T_x$-HF/LiCl, with Na^+ or Rb^+ ions from their chloride solutions (Ref.[85]).*

Figure 61.a plots the XPS spectra for Li 1s region for un-sputtered $Ti_3C_2T_x$-10HF, Li-$Ti_3C_2T_x$-HF/LiCl, Na-$Ti_3C_2T_x$-HF/LiCland Rb-$Ti_3C_2T_x$-HF/LiCl. For the $Ti_3C_2T_x$-10HF sample no peaks related to any Li species were found, while for the Li-$Ti_3C_2T_x$-HF/LiCl sample, two peaks related to Li species. These peaks correspond to LiF and/or LiCl species at a BE of 56.1 eV and resulted from the residue of etching, where some LiF and/or LiCl salts were not completely removed [85]. The other peak corresponds to Li-O and/or LiOH. At a BE of 54.2 eV, probably originates from the presence of Li^+ ions interacting with H_2O or with MXene-bound O-containing groups [158]. The Li-O and/or the LiOH peaks disappeared after the sample was immersed in NaCl or RbCl. XPS spectra of Li 1s region for Na-$Ti_3C_2T_x$-HF/LiCl, and Rb-$Ti_3C_2T_x$-HF/LiCl could not be fitted for this peak. This indicates the removal of the Li^+ ions from between the layers.

Figure 61.b shows the XPS spectra of Na 1s region for Na-$Ti_3C_2T_x$-HF/LiCl sample. This region was fit by four peaks corresponding to the following species: NaF/NaCl [128], NaOH/Na2O [159,160] Ti-C, and TiO_2. The former two originate from the Ti LMM Auger lines [128]. While the NaF/NaCl species most likely result from incomplete dissolution of NaCl and the possible formation of NaF, the NaOH/Na_2O species most probably originates from the intercalated Na^+ ions. **Figure 61.c** shows the XPS spectra of Rb 3d region for Rb-$Ti_3C_2T_x$-HF/LiCl. This region is fit by a species corresponding to Rb^+ ions probably intercalating between the MXene layers [161]. The disappearance of the Li^+ species in the Li 1s region for Na-$Ti_3C_2T_x$-HF/LiCl and Rb-$Ti_3C_2T_x$-HF/LiCl, and the appearance of Na^+ species in the Na 1s region and Rb^+ species in the Rb 3d region for Na-$Ti_3C_2T_x$-HF/LiCl and Rb-$Ti_3C_2T_x$-HF/LiCl, respectively, suggests complete ion exchange between the Li^+ and Na^+ or Rb^+. The chemical formulae of Na-$Ti_3C_2T_x$-HF/LiCl and Rb-$Ti_3C_2T_x$-HF/LiCl, obtained from

the XPS peak fittings, found in [85], are $0.24Na\text{-}Ti_3C_2O_{0.6}(OH)_{081}F_{0.6}.0.7H_2O_{ads.}$ and $0.16Rb\text{-}Ti_3C_2O_{0.5}(OH)_{0.6}F_{0.7}.0.5H_2O_{ads}$.

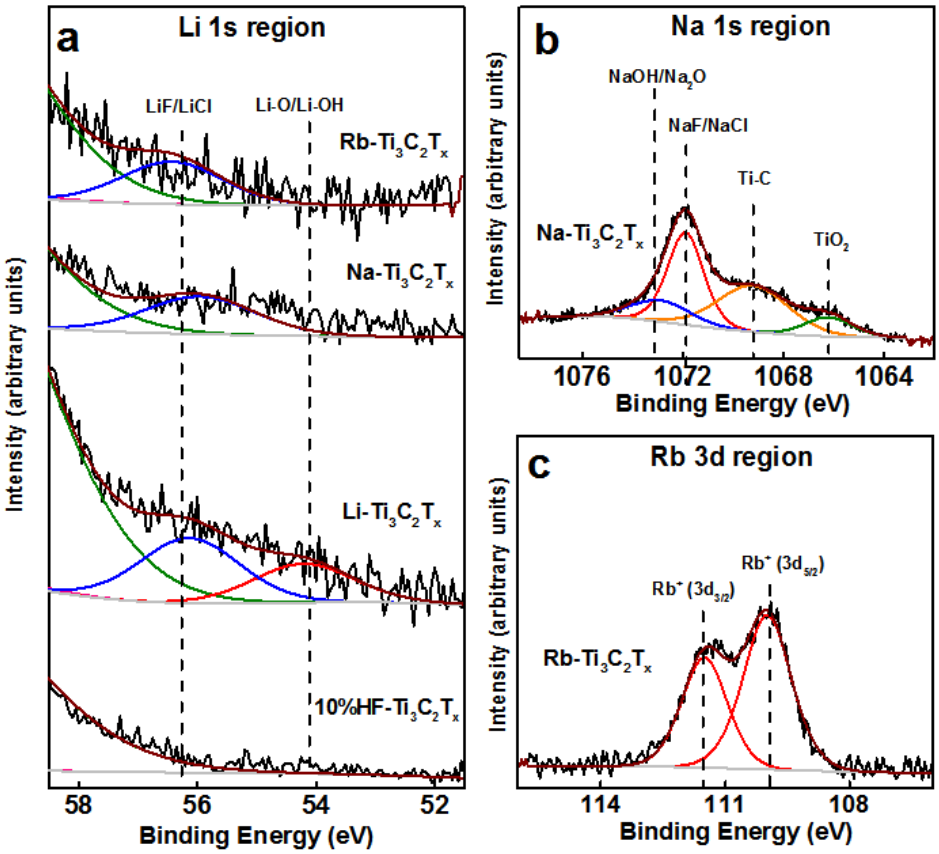

Figure 61. *XPS spectra with curve fitting for: a) Li 1s region for un-sputtered $Ti_3C_2T_x$-10HF, Li-$Ti_3C_2T_x$-HF/LiCl, Na-$Ti_3C_2T_x$-HF/LiCl, and Rb-$Ti_3C_2T_x$-HF/LiCl cold pressed disks. Dashed vertical lines represent, from left to right, species LiF/LiCl and $LiOH/Li_2O$; the large shoulder on the left is due to the Ti 3s peak, respectively; b) Na 1s region for un-sputtered Na-$Ti_3C_2T_x$-HF/LiCl. Dashed lines, from left to right, represent the species NaOH (Na 1s region), NaF/NaCl (Na 1s region), Ti-C (Auger LMM line), and TiO_2 (Auger LMM line), respectively; and c) Rb 3d region for Rb-$Ti_3C_2T_x$-HF/LiCl. Dashed vertical lines, from right to left represent the species Rb^+ ($3d_{5/2}$), RbCl ($3d_{5/2}$), Rb^+ ($3d_{3/2}$), and RbCl ($3d_{3/2}$), respectively (Ref. [85]).*

4.4 Determination of the nature and amounts of surface termination groups

This section discusses the nature of the surface termination groups, how they were formed and their total amount. I will start by the etching reactions mentioned in **Chapter 2** and will take the synthesis of $Ti_3C_2T_x$ as an example. When Ti_3AlC_2 is immersed in aqueous HF solution, the following reactions were proposed to take place by Naguib *et al*. [39]:

$$Ti_3AlC_2 + 3HF = AlF_3 + 3/2H_2 + Ti_3C_2 \quad (1)$$

$$Ti_3C_2 + 2H_2O = Ti_3C_2(OH)_2 + H_2 \quad (2)$$

$$Ti_3C_2 + 2HF = Ti_3C_2F_2 + H_2 \quad (3)$$

The second reaction produces -OH terminated Ti_3C_2. A schematic of the structure is shown in **Figure 62.a,** where each surface Ti atom is bonded to one OH group. Similarly, the third reaction produces -F terminated Ti_3C_2; a schematic the resulting structure is shown in **Figure 62.b**, where each surface Ti atom is bonded to one F atom. However, when looking at all chemical formulae of all MXenes obtained from the XPS analysis and discussed previously, there is a third surface termination species which is -O. Nuclear magnetic resonance (NMR) results have also shown that Ti_3C_2 produced by HF or LiF + HCl method a mixture surface termination of the three species: -OH, -F, and -O [162].

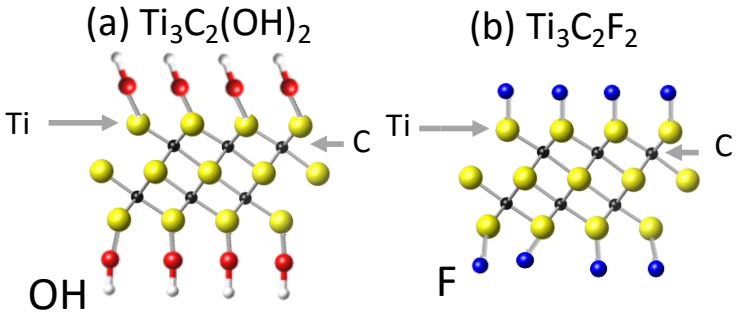

Figure 62. *Side view schematic of a) $Ti_3C_2(OH)_2$ and b) $Ti_3C_2F_2$ structures. Here the Ti atoms are colored in yellow, C, black, O, red, H, white and F, blue (not to scale).*

Therefore, the important question is how the -O terminations were formed and whether each O atom is bonded with a double bond to each Ti atom ($Ti_3C_2O_2$), **Figure 63.a**, or each O atom is bonded to two Ti atoms as a bridging O atom, viz. Ti_3C_2O, **Figure 63.b**. Under the etching conditions it is almost impossible to form $Ti_3C_2O_2$, since it requires the reaction of O_2 with Ti_3C_2 to form $Ti_3C_2O_2$ either by: i) reaction of Ti_3C_2 with O_2 dissolved in the etchant:

$$Ti_3C_2 + O_{dissolved} = Ti_3C_2O_2 \quad (14)$$

This reaction is highly unlikely to happen due to the low concentration of O_2 in the etchant compared to the concentration of OH^- and F^- ions, or ii) dissociation of water into H_2 and O_2 followed by reacting O_2 with Ti_3C_2, this path is also highly unlikely to happen due to the need of high energy for water splitting. Even if possible, it is well established that MXene are prone to oxidation into Ti-oxides when stored in water.

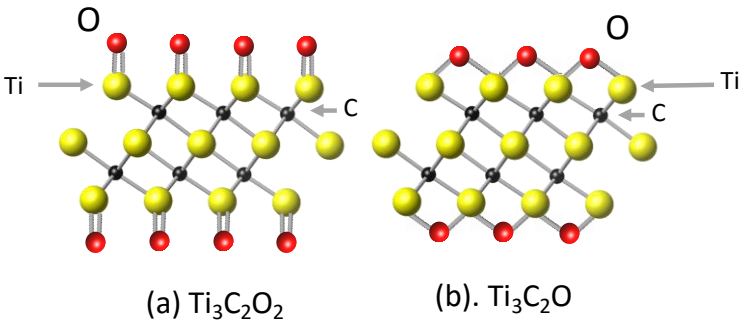

***Figure 63**. Side view schematic of a) $Ti_3C_2O_2$ and b) Ti_3C_2O structures. Here the Ti atoms are colored in yellow, C, black, and O, red, (not to scale).*

Xie *et al.* have predicted, through DFT calculations, that the -OH terminations can be converted into -O terminations through the following reaction at high temperatures [57]:

$$Ti_3C_2(OH)_2 = Ti_3C_2O_2 + H_2 \quad (15)$$

$$Ti_3C_2(OH)_2 = Ti_3C_2O + H_2O \quad (16)$$

The activation barrier for equation (15) is higher than that for equation (16), indicating the need of higher temperature for the first reaction to occur than that needed for the second one.

For the other MXenes: Ti_2CT_x-10HF, Nb_2CT_x-50HF, V_2CT_x-50HF, Mo_2CT_x-25HF, Ti_3CNT_x-30HF, $Mo_2T_iC_2T_x$-50HF, $Nb_4C_3T_x$-50HF, and $Mo_2Ti_2C_3T_x$-50HF, the average number of moles of surface terminations per moles of $M_{n+1}X_n$ is 1.95±0.3. The anomalies are Ti_2CT_x-10HF with x = 1.6, $Nb_4C_3T_x$-50HF with x = 2.6, and $Mo_2Ti_2C_3$-

50HF with x = 2.1. The reason for these discrepancies is not fully understood at this point, but for Ti_2CT_x-10HF it might be due to a deficiency in the Ti atoms, and for the $M_4X_3T_x$, one reason for x > 2 may be a deficiency in the C sites which in turn might be occupied with the surface termination groups.

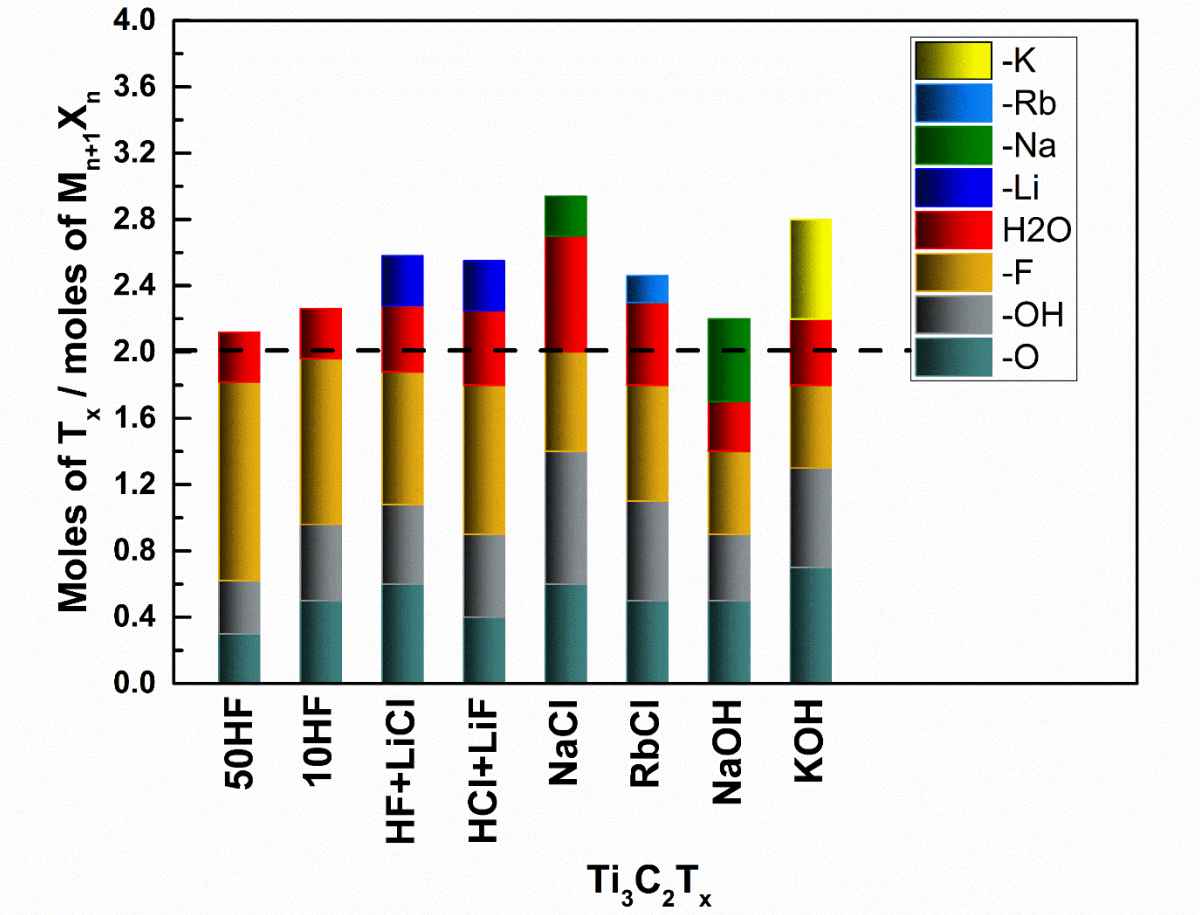

Figure 64. *Moles of Y per $M_3X_2T_x$ formula unit for $Ti_3C_2O_{0.3}(OH)_{0.32}F_{1.2}.0.3H_2O_{ads}$ (50HF), $Ti_3C_2O_{0.5}(OH)_{0.46}F_{1.0}.0.3H_2O_{ads}$ (10HF), $0.3Li\text{-}Ti_3C_2O_{0.6}(OH)_{0.48}F_{0.8}.0.4H_2O_{ads}$ (HF+LiCl), $0.3Li\text{-}Ti_3C_2O_{0.4}(OH)_{0.5}F_{0.9}.0.45H_2O_{ads}$(LiF+HCl), $0.24Na\text{-}Ti_3C_2O_{0.6}(OH)_{0.8}F_{0.6}.0.7H_2O_{ads}$ (NaCl), $0.16Rb\text{-}Ti_3C_2O_{0.5}(OH)_{0.6}F_{0.7}.0.5H_2O_{ads}$ (RbCl), $0.5Na\text{-}Ti_{2.8}C_2O_{0.5}(OH)_{0.4}F_{0.5}.0.3H_2O_{ads}$ (NaOH) and $0.6K\text{-}Ti_{2.8}C_2O_{0.7}(OH)_{0.61}F_{0.5}.0.4H_2O_{ads}$ (KOH). Note that if one termination is assumed per surface M atom, then in all cases the theoretical T_x number per formula unit is 2 given by the horizontal dashed line. This is the case because only the sum of the moles of O, OH and F constitutes the terminations.*

According to NMR studies and through multilevel structural modeling of atomic PDF analysis for high-quality neutron scattering measurements for $Ti_3C_2T_x$ produced by HF etching and LiF + HCL etching, evidence for protons between the

$Ti_3C_2T_x$ layers has been established [101,162]. Moreover, the zeta potential of $Ti_3C_2T_x$ particles at pH 7 is -29 mV [78]. Lastly, in this study it was established and confirmed that cationic exchange occurs readily in $Ti_3C_2T_x$. All these results suggest that in the presence of water, $Ti_3C_2(OH)_2$ dissociates producing protons. In the presence of water molecules, a hydronium, H_3O^+ ion is formed according to the following reactions:

$$Ti_3C_2(OH)_2 = Ti_3C_2(OH)O^- + H^+_{ads} \quad (17)$$

$$H^+_{ads} + H_2O_{ads} = [H_3O]^+ \quad (18)$$

The process is shown schematically in **Figure 65**.

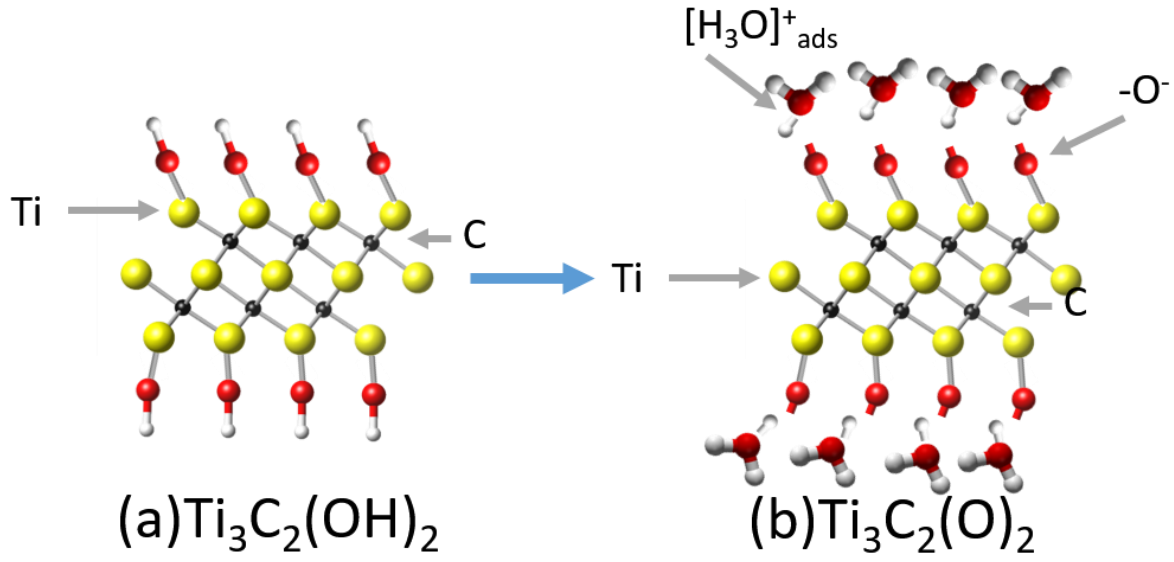

Figure 65. *Schematic showing the conversion a) -OH terminations to b) -O terminations on Ti_3C_2. Here the Ti atoms are colored in yellow, C, black, O, red, and H, white (not to scale).*

If this conjecture is correct a correlation between the moles of O-terminations per formula unit and the moles of what was labeled above H_2O_{ads} in the case of HF etching. After ion exchange a correlation should exist between the moles of O-terminations per formula unit and the sum of the moles of $H_2O_{ads} + A^+$, where A^+ is the number of alkali ion moles per formula unit. In making this conjecture it is implicitly

assumed that the number of moles of $[H_3O]^+$ is simply equal to the number of moles of -O terminations.

Figure 66.a plots the moles per formula unit of –O vs. (H_2O_{ads} + A^+) for all $Ti_3C_2T_x$ samples in this study. There is a weak correlation as shown in **Figure 66.a** where R^2 is ≈ 0.4 and the slope is ≈ 0.3. Ideally, if our conjecture is correct, the value of the slope would be unity meaning that the moles of -O are equal to the moles of (H_2O_{ads} + A^+). When plotting the moles per formula unit of –O vs. (H_2O_{ads} + A^+) for all MXenes in this study, **Figure 66.b**, the correlation is even more weaker, R^2 is ≈ 0.16 and the slope remains almost the same ≈ 0.3. To investigate the reason behind the weak correlation, the moles per formula unit of –O vs. (H_2O_{ads} + A^+) for all MXenes were plotted on a red line representing a slope of unity as shown in **Figure 66.c**. The actual chemistries of all the MXenes are presented in **Table 16**. Only one MXene -$Nb_4C_3T_x$-50HF - falls on that line. Most of the points are below the line and thus contain more H_2O than our conjecture predicts. The simplest explanation for these points is that interlayer water is present. Said otherwise, when these measurements were made, the samples were not fully dry. Given the recent results by Ghidiu *et al.* [85] who have shown by XRD that most cations are surrounded by a layer of more of water of hydration this explanation is reasonable.

The 5 points above the line are more problematic and at this point there is no good explanation. We note in passing that the errors associated with these 5 points were the highest recorded and thus at least some of the discrepancy can be simply due to measurement error. Said otherwise, some of the oxygen ascribed to these MXenes may actually O associated with CO and COO surface contamination groups. This comment notwithstanding, more careful work is needed to try and shed more light on the problem.

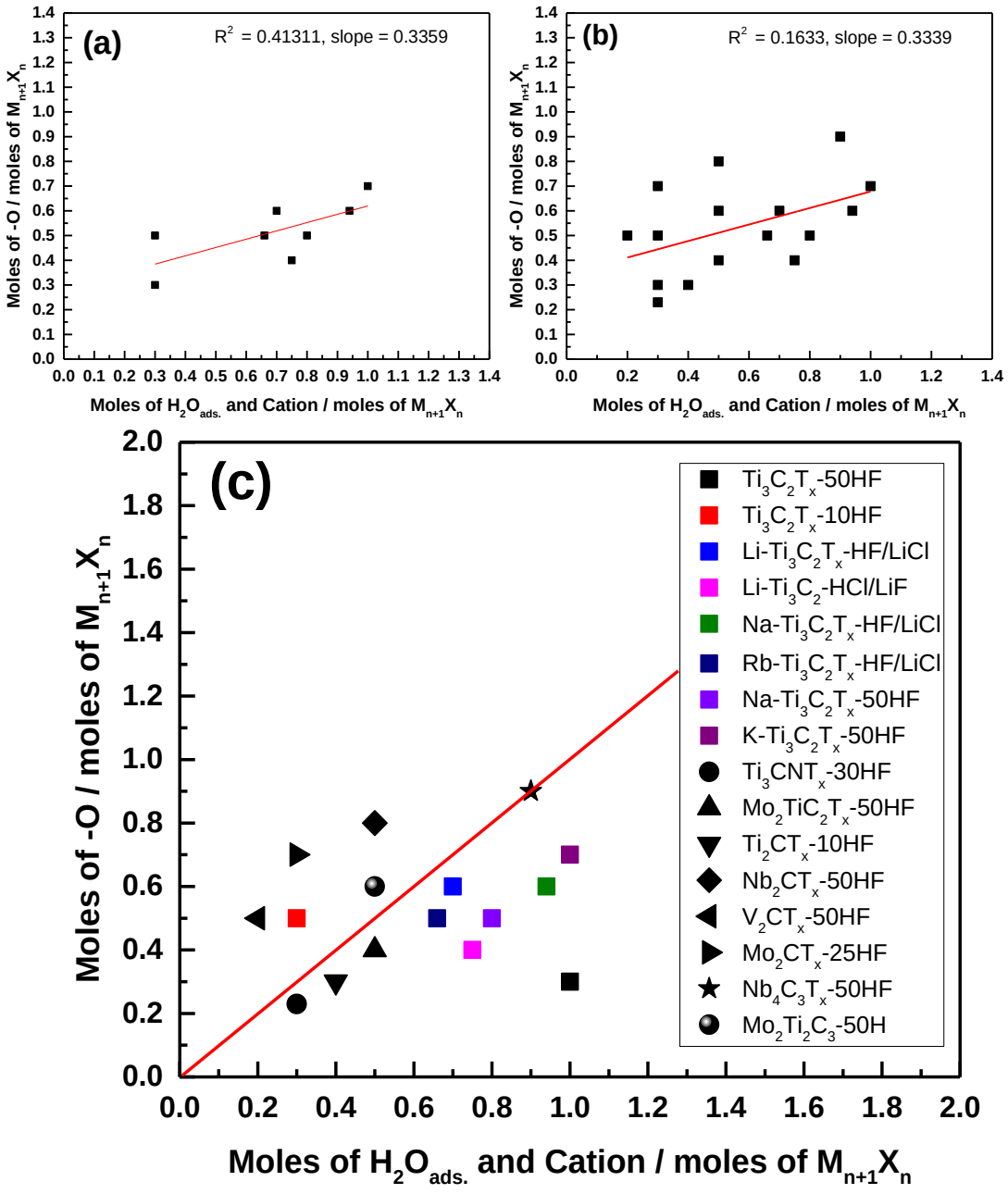

Figure 66. *Moles of -O terminations vs. moles of adsorbed water and cations per unit formula of $M_{n+1}X_nT_x$ for all* ***a.*** *all $Ti_3C_2T_x$ in this study shown in* ***Table 16*** *and* ***b.*** *all MXenes in this study shown in* ***Table 16****.* ***c.*** *Moles of -O terminations vs. moles of adsorbed water and cations per unit formula of $M_{n+1}X_nT_x$ for all MXenes. The red line of slope = 1, represents the condition where the moles of -O termination = moles of $H_2O_{ads.}$ + cations.*

Table 16. *Chemical formulae of all MXenes, presented in this study, determined from XPS spectra before sputtering. The label of each sample is listed in parentheses*

M_2XT_x	$M_3X_2T_x$	$M_4X_3T_x$
$Ti_2C_{0.9}O_{0.3}(OH)_{0.5}F_{0.8}.0.4H_2O_{ads}$ (Ti_2CT_x-10HF)	$Ti_3C_2O_{0.3}(OH)_{0.32}F_{1.2}.0.3H_2O_{ads.}$ ($Ti_3C_2T_x$-50HF)	$Nb_4C_{2.6}O_{0.9}(OH)_{1.0}F_{0.7}.0.9H_2O_{ads.}$ ($Nb_4C_3T_x$-50HF)
$Nb_2CO_{0.8}(OH)_{0.5}F_{0.7}.0.5H_2O_{ads.}$ (Nb_2CT_x-50HF)	$Ti_3CNO_{0.23}(OH)_{0.33}F_{1.3}.0.33H_2O_{ads.}$ (Ti3CNTx-30HF)	$Mo_2Ti_{1.5}C_{2.5}O_{0.6}(OH)_{1.0}F_{0.5}.0.5H_2O_{ads.}$ ($Mo_2Ti_2C_3T_x$-50HF)
$V_2CO_{0.5}(OH)_{0.2}F_{1.1}.0.2H_2O_{ads.}$ (V_2CT_x-50HF)	$Mo_2Ti_{0.8}C_2O_{0.4}(OH)_{0.7}F_{1.0}0.5H_2O_{ads.}$ (Mo_2TiC_2Tx-50HF)	
$Mo_2CT_xO_{0.7}(OH)_{0.4}F_{0.7}.0.3H_2O_{ads.}$ (Mo_2CTx-25HF)	$Ti_3C_2O_{0.5}(OH)_{0.46}F_{1.0}.0.3H_2O_{ads.}$ ($Ti_3C_2T_x$-10HF)	
	0.3Li-$Ti_3C_2O_{0.6}(OH)_{0.48}F_{0.8}.0.4H_2O_{ads.}$ (Li-$Ti_3C_2T_x$-LiCl/HF)	
	0.3Li-$Ti_3C_2O_{0.4}(OH)_{0.5}F_{0.9}.0.45H_2O_{ads.}$ (Li-$Ti_3C_2T_x$-LiF/HCl)	
	0.24Na-$Ti_3C_2O_{0.6}(OH)_{081}F_{0.6}.0.7H_2O_{ads.}$ (Na-$Ti_3C_2T_x$-LiCl/HF)	
	0.16Rb-$Ti_3C_2O_{0.5}(OH)_{0.6}F_{0.7}.0.5H_2O_{ads.}$ (Rb-$Ti_3C_2T_x$-LiCl/HF)	
	0.6K-$Ti_{2.8}C_2O_{0.7}(OH)_{0.61}F_{0.5}.0.4H_2O_{ads}$ (K-$Ti_3C_2T_x$-50HF)	
	0.5Na-$Ti_{2.8}C_2O_{0.5}OH_{0.4}F_{0.5}0.3H_2O_{ads.}$ (Na-$Ti_3C_2T_x$-50HF)	

To summarize this section, a mechanism for the formation -O termination through the dissociation of OH^- into -O and weakly bonded H^+ is proposed. The H^+ react with H_2O_{ads} forming $[H_3O]^+$. In the presence of other cations, the latter replace the $[H_3O]^+$. This exchange can be a complete or incomplete.

4.4.1 Calculating the oxidation number for C in $Ti_3C_2T_x$

By compensating the mole amounts of -O terminations with H^+ protons, the $Ti_3C_2T_x$ can be assumed neutral. Using in situ X-ray absorption (XAS), Lukatskaya *et*

al. [99] found that the average oxidation number for Ti in $Ti_3C_2T_x$ is 2.4. This information can be used to solve for the oxidation number of C in $Ti_3C_2T_x$, assuming that the oxidation states of O, F, H and OH and A^+ are -2, -1, +1, -1 and -1, respectively. The calculation of the oxidation number of C for all the $Ti_3C_2T_x$ samples is shown in **Table 17**. In all these calculations, the number of cations - including H_3O^+ is assumed to be equal to the number of O moles. This assumption is good in all cases except the second entry for which O < cations of H_2O_{ads} (see **Table 16**).

The average oxidation number for C in $Ti_3C_2T_x$ is thus -2.6±0.1. These results indicate that the average oxidation state of Ti and C are fixed and depend weakly on the nature and the distribution of the surface terminations or the intercalated cations. In other words, the surface terminations and intercalated cations adjust to neutralize the charge on the Ti_3C_2 blocks and not vice versa.

Table 17. *Moles and total charge of Ti, surface termination groups (-O, -OH, and -F), cations (H^+, Li^+, Na^+, K^+ and Rb^+), and the oxidation # of C in various $Ti_3C_2T_x$ (MXenes).*

	Ti [moles]	O [moles]	OH [moles]	F [moles]	Cation [moles]	Net charge[a]	C [oxid. #][b]
$Ti_3C_2T_x$-50HF	3	0.3	0.32	1.2	H^+ = 0.3	+5.38	-2.70
$Ti_3C_2T_x$ -10HF	3	0.5	0.46	1	H^+ = 0.5	+5.24	-2.60
Li-$Ti_3C_2T_x$-HCl/LiCl	3	0.6	0.48	0.8	Li^+ = 0.3 H^+= 0.3	+5.32	-2.70
Li-$Ti_3C_2T_x$-HCl/LiCl	3	0.4	0.45	0.9	Li^+ = 0.3 H^+ = 0.1	+5.45	-2.70
Na-$Ti_3C_2T_x$-HCl/LiCl	3	0.6	0.8	0.6	Na^+ = 0.24 H^+ = 0.36	+5.20	-2.60
Rb-$Ti_3C_2T_x$-HCl/LiCl	3	0.4	0.5	0.9	Rb^+ = 0.16 H^+ = 0.24	+5.40	-2.70
Na- $Ti_3C_2T_x$-50HF	2.8	0.5	0.4	0.5	Na^+ = 0.5	+5.32	-2.66
K- $Ti_3C_2T_x$-50HF	2.8	0.7	0.61	0.5	K^+ = 0.6 H^+ = 0.1	+4.91	-2.455

[a] Total charge = moles of Ti* its charge (+2.4) + molar amount of O* its charge (-2) + molar amount of OH* its charge (-1) + molar amount of F* its charge (-1) + molar amount of cation* its charge.
[b] Carbon oxidation number = -(total negative charge) / the molar amount of C.

In a similar manner the oxidation number of C in V_2CT_x can be calculated using the oxidation number of V determined from XANES by Wang *et al.* [163] to be +3. An average of the oxidation number of C for V_2CT_x was obtained from V_2CT_x formula obtained in this study and V_2CT_x and the formula obtained from NMR studies by Harris *et al.* [164] listed in **Table 18**. It is worth noting that the formula of V_2CT_x obtained in this study show $O^- > H_2O$, for that two cases were considered: 1. assuming all H^+ protons are $[H_3O]^-$ and 2. Assuming all O^- have H^+ protons. The average oxidation number for C in all cases of V_2CT_x was calculated to be -3.96±0.2 which is significantly higher than that for $Ti_3C_2T_x$.

Table 18. *Moles and total charge of V, surface termination groups (-O, -OH, and -F), protons H^+, and the oxidation # of C in V_2CT_x (MXenes).*

	V [moles]	O [moles]	OH [moles]	F [moles]	Protons [moles]	Net charge[a]	C [oxid. #][b]
V_2CT_x-50HF [This work] Assuming all H^+ is $[H_3O]^+$	2	0.5	0.2	1.1	$H^+ = 0.2$	+5.38	-3.9
V_2CT_x-50HF [This work] Assuming all $H^+ = O^-$	2	0.5	0.2	1.1	$H^+ = 0.5$	+5.38	-4.2
V_2CT_x [Ref.[164]]	2	--	1	1.2	--	+3.8	-3.8

[a] Total charge = moles of V* its charge (+3) + molar amount of O* its charge (-2) + molar amount of OH* its charge (-1) + molar amount of F* its charge (-1) + molar amount of proton* its charge.
[b] Carbon oxidation number = -(total charge) / the molar amount of C.

4.5 Mechanism of reaction of KOH and NaOH with $Ti_3C_2T_x$-50HF

In this section I am going to use the information deduced in section 4.4 regarding the nature of the surface termination groups, their total amounts, the presence of weakly bonded $[H_3O]^+$ protons and the cation exchange in $Ti_3C_2T_x$ MXenes in order to suggest a mechanism for the ration of KOH and NaOH with $Ti_3C_2T_x$.

The chemical formula for the $Ti_3C_2T_x$ before the hydroxide treatment is $Ti_3C_2O_{0.3}(OH)_{0.32}F_{1.2}.0.3[H_3O_{ads}]^+$. After KOH treatment, the chemical formula changes to $0.6K\text{-}Ti_{2.8}C_2O_{0.7}(OH)_{0.61}F_{0.5}.0.3H_2O_{ads}.0.1[H_3O_{ads}]^+$. The mechanism is described in the following steps:

1. Cation exchange occurs by replacing 0.3 moles of $[H_3O_{ads}]^+$ with 0.3 moles of K^+

   $Ti_3C_2O_{0.3}(OH)_{0.32}F_{1.2}.0.3[H_3O_{ads}]^+ + 0.3K^+ =$

   $0.3K\text{-}Ti_3C_2O_{0.3}(OH)_{0.32}F_{1.2} + 0.3[H_3O_{ads}]^+$
2. Preferential removal of Ti atoms took place, decreasing the Ti moles by 0.2 moles
3. The -O termination increased by 0.4 moles, from 0.3 to 0.7
4. The -F termination decreased by 0.7 moles, from 1.2 to 0.5
5. The -OH termination increased by 0.29 moles, from 0.32 to 0.61

6. The molar percentage of oxides and oxyflourides compared to $Ti_3C_2T_x$ in the sample increased from 5% to 18.7%
7. Points 2 to 6 results in the transformation of 0.2 moles of both Ti and F to $TiO_{2-x}F_x$ (to accommodate for the lost 0.2 moles of Ti), while another 0.4 moles of -F are replaced with O^- and H^+ (to accommodate for the increase of 0.4 moles in -O)

   $0.3K\text{-}Ti_3C_2O_{0.3}(OH)_{0.32}F_{1.2} + 0.2OH^- =$

   $0.3K\text{-}Ti_{2.8}C_2O_{0.3}(OH)_{0.32}F_1 + 0.2TiOF + 0.2H^+$

   $0.3K\text{-}Ti_{2.8}C_2O_{0.3}(OH)_{0.32}F_1 + 0.4OH^- + 0.3H_2O =$

   $0.3K\text{-}Ti_{2.8}C_2O_{0.7}(OH)_{0.32}F_{0.5}.0.4[H_3O_{ads}]^+ + 0.5F^-$
8. From the newly added $[H_3O]^+$, 0.3 moles are further exchanged with 0.3 moles of K^+ (now all 0.6 moles of K^+ are intercalated in the $Ti_3C_2T_x$)

   $0.3K\text{-}Ti_{2.8}C_2O_{0.7}(OH)_{0.32}F_{0.5}.0.4[H_3O_{ads}]^+ + 0.3K^+ =$

   $0.6K\text{-}Ti_{2.8}C_2O_{0.7}(OH)_{0.32}F_{0.5}.0.1[H_3O_{ads}]^+ + 0.3[H_3O_{ads.}]^+$
9. The remaining 0.1 mole of -F, out of the 0.7 moles reduced by the KOH treatment, is replaced with -OH terminations.

   $0.6K\text{-}Ti_{2.8}C_2O_{0.7}(OH)_{0.32}F_{0.56}.0.1[H_3O_{ads}]^+ + 0.1OH^- + 0.3[H_2O_{ads.}] =$

   $0.6K\text{-}Ti_{2.8}C_2O_{0.7}(OH)_{0.42}F_{0.5}.0.3H_2O_{ads}.0.1[H_3O_{ads}]^+$
10. This would leave 0.19 moles of -OH unaccounted for, these might have occupied some defects that occurred during the oxidation of some $Ti_3C_2T_x$ particles.

A similar mechanism occurs when treating $Ti_3C_2T_x$ with NaOH. After the NaOH treatment the chemical formula changes to $0.5Na\text{-}Ti_{2.8}C_2O_{0.5}(OH)_{0.4}F_{0.5}0.3H_2O_{ads.}$. The mechanism can be described according to the steps below:

1. Cation exchange takes place replacing 0.3 moles of $[H_3O]^+$ with 0.3 moles of Na^+

   $Ti_3C_2O_{0.3}(OH)_{0.32}F_{1.2}.0.3[H_3O_{ads}]^+ + 0.3Na^+ =$

   $0.3Na\text{-}Ti_3C_2O_{0.3}(OH)_{0.32}F_{1.2} + 0.3[H_3O_{ads}]^+$
2. Preferential removal of Ti atoms took place, decreasing the Ti moles by 0.2 moles
3. The -O termination increased by 0.2 moles, from 0.3 to 0.5
4. The -F termination decreased by 0.7, from 1.2 to 0.5
5. The -OH termination increased by 0.08, from 0.32 to 0.4
6. The molar percentage of oxides and oxyflourides compared to $Ti_3C_2T_x$ in the sample increased from 5.0% to 88.8%
7. Points 2 to 6 results in the transformation of 0.2 moles of both Ti and F to $TiO_{2-x}F_x$ (to accommodate for the lost 0.2 moles of Ti), while another 0.2 moles of -F are replaced with O^- and H^+ (to accommodate for the increase of 0.2 moles in -O)

   $0.3Na\text{-}Ti_3C_2O_{0.3}(OH)_{0.32}F_{1.2} + 0.2OH^- =$

   $0.3Na\text{-}Ti_{2.8}C_2O_{0.3}(OH)_{0.32}F_1 + 0.2TiOF + 0.2H^+$

   $0.3Na\text{-}Ti_{2.8}C_2O_{0.3}(OH)_{0.32}F_1 + 0.2\ OH^- + 0.3H_2O_{ads.} =$

   $0.3Na\text{-}Ti_{2.8}C_2O_{0.5}(OH)_{0.32}F_{0.8}.0.3[H_3O_{ads.}].0.2H_2O_{ads.} + 0.2F^-$
8. The newly added 0.2 moles of $[H_3O]^+$ are further exchanged with 0.2 moles of Na^+ (now all 0.5 moles of Na^+ are intercalated in the $Ti_3C_2T_x$)

   $0.3Na\text{-}Ti_{2.8}C_2O_{0.5}(OH)_{0.32}F_{0.8}.0.3[H_3O_{ads.}].0.2H_2O_{ads} + 0.2Na^+ =$

   $0.5Na\text{-}Ti_{2.8}C_2O_{0.5}(OH)_{0.32}F_{0.8}0.3[H_3O_{ads.}] + 0.2[H_3O_{ads}]^+$
9. Out of the remaining amount of -F terminations, 0.08 moles are replaced by 0.08 moles of -OH terminations (to account for the 0.08 mole increase in -OH)

   $0.5Na\text{-}Ti_{2.8}C_2O_{0.5}(OH)_{0.32}F_{0.8}.0.3[H_3O_{ads.}] + 0.08OH^- =$

   $0.5Na\text{-}Ti_{2.8}C_2O_{0.5}(OH)_{0.4}F_{0.72}.0.3[H_3O_{ads.}] + 0.08F^-$

10. This would leave 0.22 moles of -F unaccounted for, which might have turned to oxyflourides with the transformation of some MXenes to oxyflourides

It is worth noting that these experiments were conducted ex situ, i.e. the KOH treatment was not done inside the XPS, this might have an effect on the accuracy of the results and the comparison between the chemical formula before and after the treatments. To summarize this section, several processes are suggested to take place when treating $Ti_3C_2T_x$ particles in a hydroxide solution of either KOH or NAOH. These processes involved:

1. Selective removal of Ti and F atoms replaced by either -OH and/or -O and H^+
2. Ion exchange, replacing the $[H_3O]^+$ with cations
3. Replacement of -F terminations with either -OH and/or -O and H^+
4. Further oxidation of some MXene particles which transform to oxides and/or oxyflourides.

These results provided further understanding to the surface terminations in MXenes which would impact the choice of MXene for a certain application and would help scientists to manipulate the surface terminations and understand how this manipulation affects the chemistry of MXene. In addition to that, being able to determine the amounts of each surface termination group precisely would enable theoreticians to come with models for MXenes that are much more closer to the experimental data which would which would lead to a higher accuracy in their predictions for the electronic structures and properties of MXenes. Finally, this work has proven that XPS is a very powerful technique that can be used to obtain valuable information about the chemistry of MXenes and in particular the nature of the surface terminations and their distribution.

CHAPTER 5: SUMMARY AND FUTURE WORK

The main focus of this work was to identify and quantify the various chemical species in a new family of two-dimensional carbides and carbonitrides (MXenes) using XPS and to understand the mechanism behind the changes in surface terminations when treated with hydroxides or metal chloride solutions.

In-depth analyses of the XPS spectra of the core levels of cold-pressed disks of HF-etched $Ti_3C_2T_x$, Ti_2CT_x, Ti_3CNT_x, Nb_2CT_x, $Nb_4C_3T_x$, V_2CT_x, Mo_2CT_x, $Mo_2TiC_2T_x$, and $Mo_2Ti_2C_2T_x$ were carried out. Through peak fitting of the XPS spectra, MXene surface termination groups were identified to be a mixture of -O, F, and/or -OH, in addition to adsorbed H_2O molecules.

Chemical formulae for all the MXenes studied herein were obtained from the quantification of the various species obtained from the XPS analysis. The average value of x for all compounds with very different chemistries, etching solutions and post-etching treatments was calculated to be $\approx 1.9\pm0.3$, confirming that in essence the fundamental etching reaction is one where each surface M atom is ultimately bonded to either an OH or F. Said otherwise the fundamental etching reaction is simply:

$$M_{n+1}X_n + \text{etchant} = M_{n+1}X_n(OH)_{2-\Delta}F_\Delta$$

The presence of -O terminations is interpreted to result from a dissociation of a fraction of the -OH terminations into -O and a proton, with the latter forming $[H_3O]^+$. The positively charged $[H_3O]^+$ ion is in turn then held between the layers more tightly than water molecules that are not charged. The main evidence presented for this conclusion is a correlation between the moles of O terminations and adsorbed water per

formula unit of all MXenes. The correlation is not exact, however, most probably because of the presence of trapped water molecules and or water of hydration associated with intercalated cations. In 5 cases, the fraction of O terminations was > adsorbed water. More work is needed to understand this result.

Once the presence of $[H_3O]^+$ is appreciated, then simple cationic exchange explains the fact that all cations to which MXenes have been exposed end up between the MX-layers [43,47-49,65,85,158,165]. In this work, - through XPS analysis of $Ti_3C_2T_x$ etched by a mixture of LiF and HCl or LiCl and HF solutions - the presence of Li^+ intercalated ions was confirmed and quantified. After the Li^+ ion intercalated $Ti_3C_2T_x$ samples were immersed in a solution of RbCl or NaCl, the Li^+ ions were exchanged with Rb^+ or Na^+ ions, respectively. Similar cation intercalations occurred when immersing $Ti_3C_2T_x$ multilayers in NaOH and KOH solutions. In addition to that, such treatment resulted in a large reduction of the amount of -F terminations.

Combining our results with recent XANES measurements, that have shown that the average oxidation state of Ti to be +2.4, we show that the average oxidation state of the C atoms in the four as-produced and the five intercalated $Ti_3C_2T_x$ samples was determined to be ≈ -2.6±0.1. This is very important because it indicates that the charge on the Ti and C is constant and does not depend on the surface groups or the intercalated cations. Thus, the surface terminations and cations adjust to neutralize the charge on the Ti_3C_2 blocks. Similarly, the average oxidation number of C atoms in V_2CT_x was determined to be ≈ -3.96±0.2, using recent XANES results showing the average oxidation state of V is +3.0.

The treatment of HF-etched $Ti_3C_2T_x$ with KOH or NaOH resulted in a change in the chemistry the MXene by the following suggested processes: (1) selective removal of Ti and F atoms replaced by either -OH and/or -O and $[H_3O]^+$ ions, (2) ion exchange

and that replaced the $[H_3O]^+$ ions with K^+ or Na^+ cations, (3) replacement of -F terminations with either -OH and/or -O and $[H_3O]^+$ ions and (4) the oxidation of some MXene particles which converts them to oxides and/or oxyflourides.

There were no obvious correlations between changes in M, X or *n* on the distribution of the surface termination groups.

Sputtering the surface of MXene with Ar^+ ions leads to: (i) The change in the binding energy of the chemical species, (ii) selective sputtering of C, and (iii) changes in the distribution of surface terminations. Therefore, it is not recommended to sputter the MXene samples when doing XPS analysis to identify and quantify the various chemical species. Storing MXenes in air leads to their slow and gradual oxidation which starts at the -F terminated sites transforming them to metal oxyfluorides and a decrease the amount of -F terminations in the MXene.

For the same MXene compound, taking $Ti_3C_2T_x$ as an example, the distribution of surface terminations is affected by the type and concentration of the etchant. Decreasing the HF concentration resulted in decreasing the -F terminations and increasing the -O terminations.

The importance of this work is manifested in determining and identifying the surface termination groups which is useful for testing theoretical models for MXenes that are closer to their experimental structure and chemistry which in return should provide more accurate predictions for the MXene properties.

Future directions

Effect of Annealing. There are number of questions that should be answered to further progress our understanding of the surface chemistry of MXenes. One of the important questions is the role of heat on modifying the surface terminations of

MXenes. Several theoretical work investigated this topic [57], however there is no conclusive and in-depth experimental study through in situ XPS characterization that was directed towards studying this point.

Effect of various gas treatments. Reports on the behavior of MXene in various atmospheres are scarce. Several theoretical and experimental studies were dedicated to examine the potential of MXenes as gas sensors [52,166]. An in-depth investigation of the surface chemistry modifications of MXenes in the presence of various gases is essential for evaluating the use of MXenes as gas sensors.

Determining the oxidation state of the X element in MXenes other than $Ti_3C_2T_x$. The determination of the oxidation state of the M elements in MXenes other than $Ti_3C_2T_x$, and V_2CT_x by XANES is essential for obtaining the oxidation state of the X element. In other words, XANES and XPS complement each other and allow for the determination of the oxidation states of both M and X elements in MXenes.

Hydration in-situ XPS analysis. Water plays an important role in the structure of MXenes, water molecules are adsorbed on the MXene surface, intercalated between the layers and/or dissociated into other chemical species. Thus it is essential to study the interaction of water with the MXene surface under various temperature ranges using in-situ XPS.

APPENDIX A: COMPARISON OF XPS SPECTRA OF THE MAX AND MXENE PHASES

A.1 V_2AlC vs. V_2CT_x

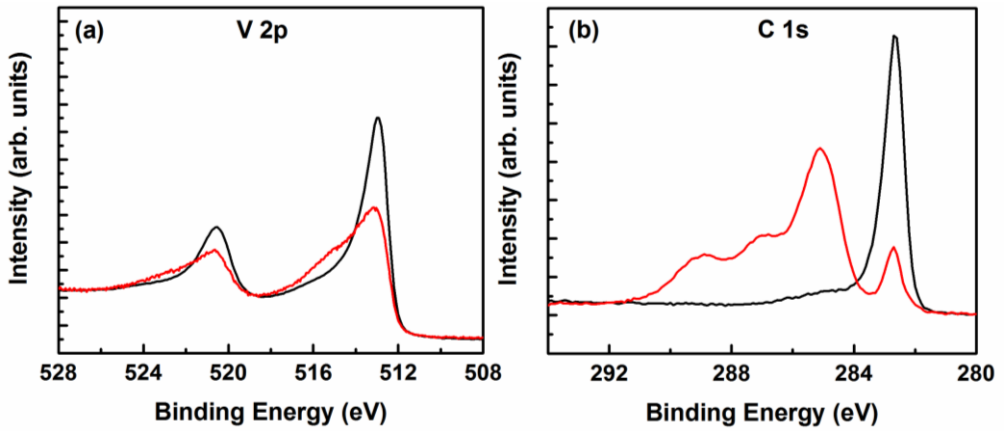

Figure 67. *XPS spectra of (a) V 2p region and (b) C 1s region for V_2AlC (black) and V_2CT_x (red).*

APPENDIX B: XPS ANALYSIS OF MXENES

B1. XPS analysis for $Ti_3C_2T_x$-10HF

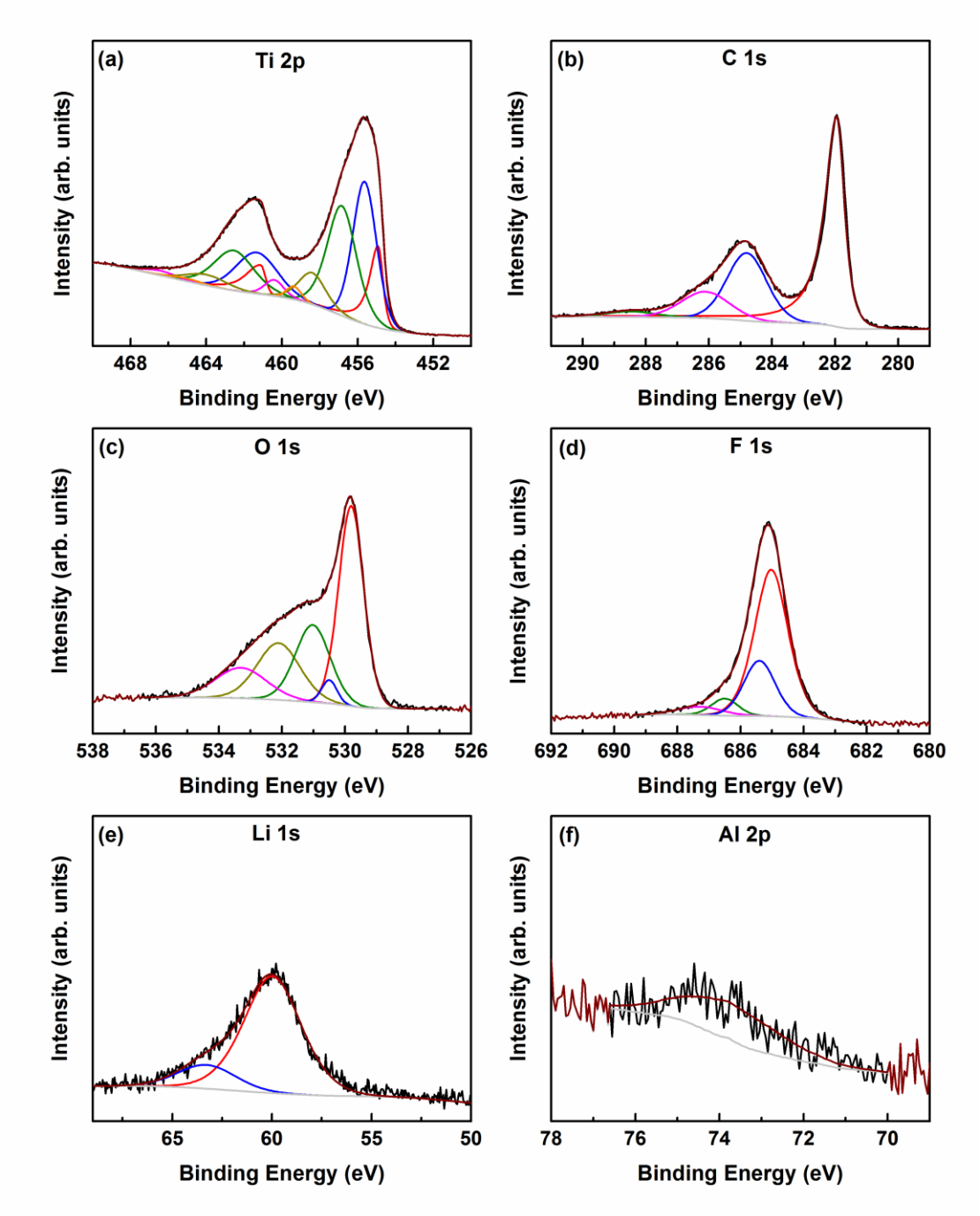

Figure 68. *XPS spectra with curve fitting for: (a) Ti 2p, (b) C 1s, (c) O 1s, (d) F 1s, (e) Li 1s, and (f) Al 2p regions for un-sputtered $Ti_3C_2T_x$-10HF cold pressed disk. Various peaks shown represent various species assumed to exist. Labels and peak colors are coordinated. The results are summarized in* ***Table 19****.*

Table 19. *Summary of XPS peak fitting results for un-sputtered ML $Ti_3C_2T_x$-10HF cold pressed disk. The numbers in parenthesis in column 2 for the Ti 2p region are peak locations of Ti $2p_{1/2}$; their respective FWHMs are listed in column 3 in parenthesis.*

Region	BE [eV][a]	FWHM [eV][a]	Fraction	Assigned to	Reference
Ti $2p_{3/2}$ ($2p_{1/2}$)	455.2 (461.4)	0.9 (1.4)	0.14	(OH, or O)-Ti-C	[123,124]
	456.0 (461.7)	1.4 (2.0)	0.20	(OH, or O)-Ti^{2+}-C	[123]
	457.1 (462.8)	1.8 (2.2)	0.28	(OH, or O)-Ti^{3+}-C	[123]
	458.9 (464.5)	1.8 (2.2)	0.14	TiO_2	[120,121]
	459.5 (465.2)	1.3 (2.0)	0.15	$TiO_{2-x}F_x$	[122]
	460.2 (466.2)	1.5 (2.7)	0.09	C-Ti-F_x	[126]
C 1s	282.3	0.9	0.28	C-Ti-T_x	[123,124]
	284.8	1.7	0.15	C-C	[127]
	285.4	2.0	0.47	CH_x	[127]
	287.2	1.6	0.05	C-O	[127]
	289.7	2.2	0.05	COO	[127]
O 1s	529.9	1.2	0.05	TiO_2	[105,120]
	530.8	1.5	0.38	$TiO_{2-x}F_x$	[122]
	531.5	1.0	0.08	C-Ti-O_x and/or OR[b]	[105,128]
	532.1	1.2	0.16	C-Ti-$(OH)_x$ and/or OR[b]	[105]
	532.7	1.3	0.19	Al_2O_3 and/or OR[b]	[128-130]
	533.5	1.7	0.14	H_2O_{ads} and/or OR[b]	[105,128]
F 1s	685.4	1.2	0.35	C-Ti-F_x	[126]
	686.1	2.0	0.53	$TiO_{2-x}F_x$	[122]
	688.0	1.7	0.12	$Al(OF)_x$	[129]
Al 2p	75.9	2.5	1.0	$Al(OF)_x$	[129]

[a] Values in parenthesis correspond to the $2p_{1/2}$ component.
[b] OR stands for organic compounds due to atmospheric surface contaminations.
[c] The spin orbit split for Al $2p_{3/2}$ and $2p_{1/2}$ were not resolved.

B2. XPS analysis of multilayered K-$Ti_3C_2T_x$-50HF

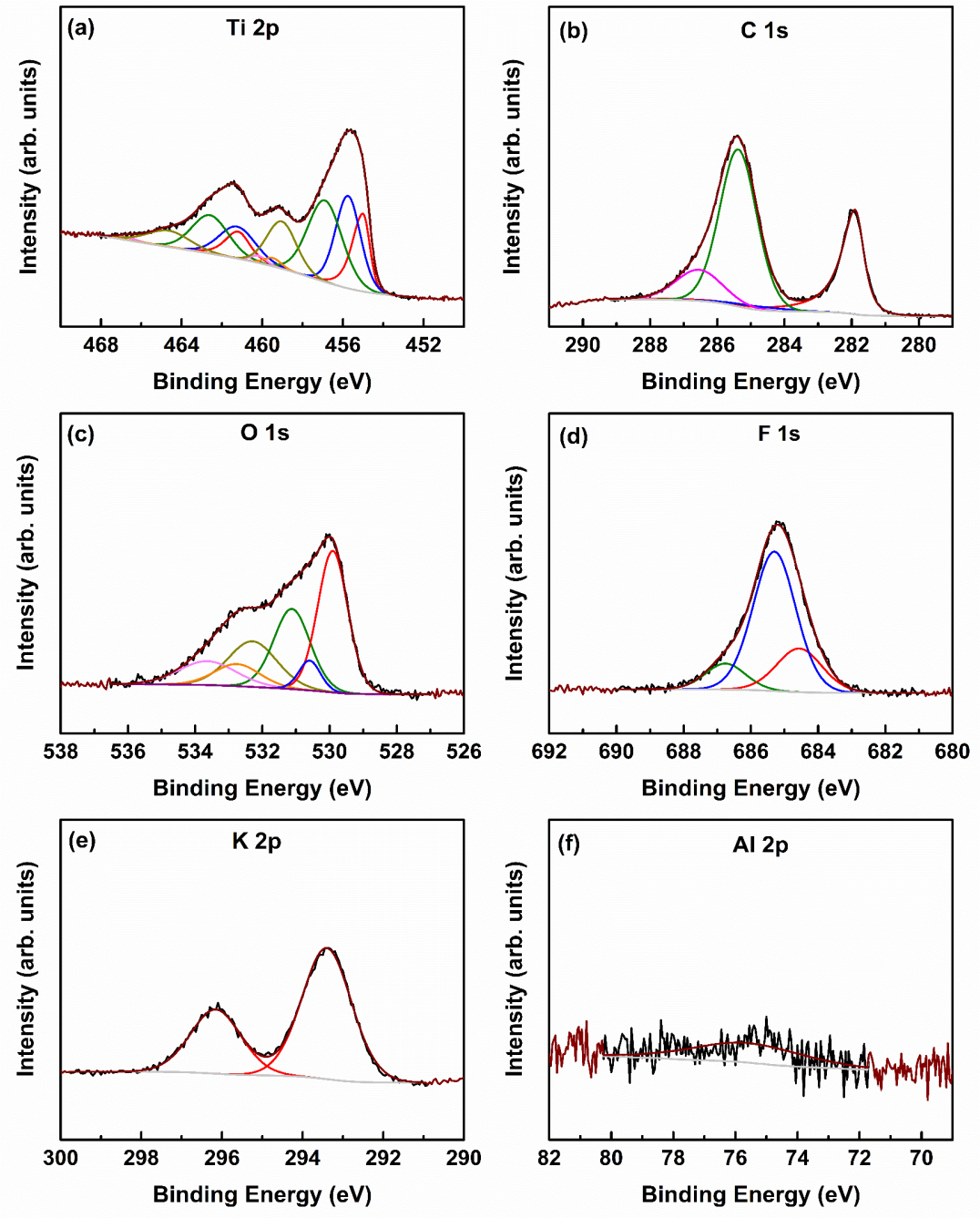

Figure 69. XPS spectra with curve fitting for: (a) Ti 2p, (b) C 1s, (c) O 1s, (d) F 1s, (e) K 2p, and (f) Al 2p regions for un-sputtered ML K-$Ti_3C_2T_x$-50HF cold pressed disk. Various peaks shown represent various species assumed to exist. Labels and peak colors are coordinated. The results are summarized in ***Table 20****.*

***Table 20**. Summary of XPS peak fitting results for un-sputtered ML K-$Ti_3C_2T_x$-50HF cold pressed disk. The numbers in parenthesis in column 2 for the Ti 2p region are peak locations of* Ti $2p_{1/2}$*; their respective FWHMs are listed in column 3 in parenthesis.*

Region	BE [eV][a]	FWHM [eV][a]	Fraction	Assigned to	Reference
Ti $2p_{3/2}$ ($2p_{1/2}$)	455.0 (461.2)	0.8 (1.4)	0.18	(OH, or O)-Ti-C	[123,124]
	455.8 (461.3)	1.5 (2.1)	0.28	(OH, or O)-Ti^{2+}-C	[123]
	456.9 (462.6)	2.0 (2.1)	0.34	(OH, or O)-Ti^{3+}-C	[123]
	459.0 (464.6)	1.7 (2.5)	0.17	TiO_2	[120,121]
	459.5 (465.5)	1.0 (2.0)	0.01	$TiO_{2-x}F_x$	[122]
	460.2 (466.7)	1.0 (1.2)	0.02	C-Ti-F_x	[126]
C 1s	281.9	0.6	0.29	C-Ti-T_x	[123,124]
	284.8	2.0	0.02	C-C	[127]
	285.4	1.3	0.55	CH_x	[127]
	286.5	1.6	0.14	C-O	[127]
O 1s	529.9	1.7	0.34	TiO_2	[105,120]
	530.6	0.8	0.05	$TiO_{2-x}F_x$	[122]
	531.1	1.3	0.24	C-Ti-O_x and/or OR[b]	[105,128]
	532.3	1.7	0.18	C-Ti- $(OH)_x$ and/or OR[b]	[105]
	532.8	1.6	0.08	Al_2O_3 and/or OR[b]	[128-130]
	533.6	2.0	0.11	H_2O_{ads} and/or OR[b]	[105,128]
F 1s	684.6	1.6	0.22	C-Ti-F_x	[126]
	685.3	1.5	0.66	$TiO_{2-x}F_x$	[122]
	686.8	1.4	0.12	AlF_x	[129]
Al 2p[c]	75.6	4.2	1.0	AlF_x	[129]
K $2p_{3/2}$ ($2p_{1/2}$)	293.4 (296.2)	1.4 (1.5)	1.0	K^+ ions	[167]

[a] Values in parenthesis correspond to the $2p_{1/2}$ component.
[b] OR stands for organic compounds due to atmospheric surface contaminations.
[c] The spin orbit split for Al $2p_{3/2}$ and $2p_{1/2}$ were not resolved.

B3. XPS analysis of multilayered Na-$Ti_3C_2T_x$-50HF

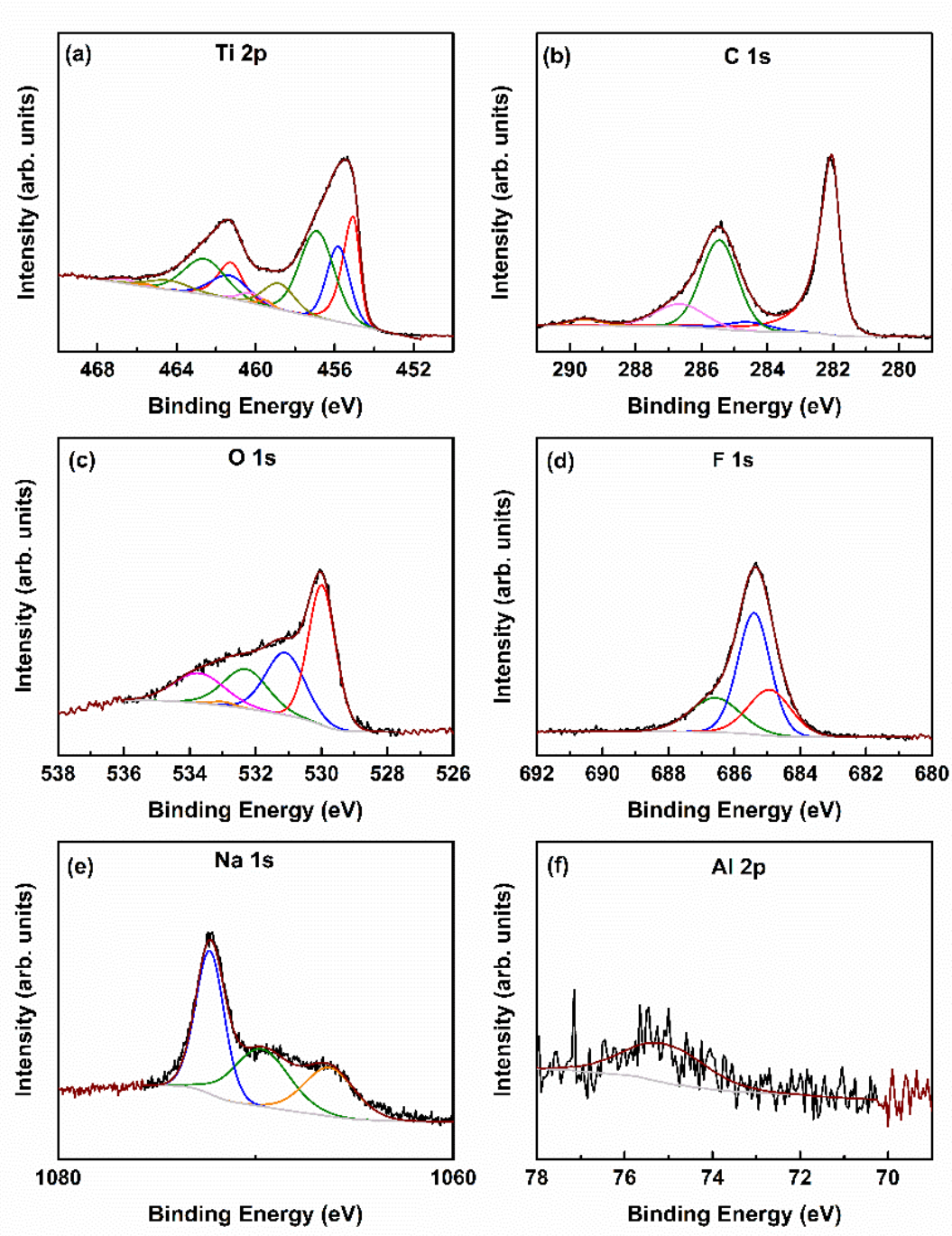

Figure 70. *XPS spectra with curve fitting for: (a) Ti 2p, (b) C 1s, (c) O 1s, (d) F 1s, (e) Na 1s, and (f) Al 2p regions for un-sputtered ML Na-$Ti_3C_2T_x$-50HF cold pressed disk. Various peaks shown represent various species assumed to exist. Labels and peak colors are coordinated. The results are summarized in* ***Table 21****.*

***Table 21**. Summary of XPS peak fitting results for un-sputtered ML Na-$Ti_3C_2T_x$-50HF cold pressed disk. The numbers in parenthesis in column 2 for the Ti 2p region are peak locations of* Ti $2p_{1/2}$*; their respective FWHMs are listed in column 3 in parenthesis.*

Region	BE [eV][a]	FWHM [eV][a]	Fraction	Assigned to	Reference
	455.1 (461.3)	0.8 (1.4)	0.25	(OH, or O)-Ti-C	[123,124]
	455.8 (461.3)	1.4 (2.2)	0.22	(OH, or O)-Ti^{2+}-C	[123]
Ti $2p_{3/2}$	456.9 (462.6)	2.0 (2.5)	0.38	(OH, or O)-Ti^{3+}-C	[123]
($2p_{1/2}$)	458.8 (464.4)	1.7 (2.5)	0.10	TiO_2	[120,121]
	459.5 (465.5)	0.8 (0.9)	0.02	$TiO_{2-x}F_x$	[122]
	460.2 (466.7)	1.1 (1.3)	0.03	C-Ti-F_x	[126]
	282.0	0.6	0.49	C-Ti-T_x	[123,124]
	284.6	1.6	0.04	C-C	[127]
C 1s	285.5	1.3	0.33	CH_x	[127]
	286.7	1.8	0.11	C-O	[127]
	289.5	1.2	0.03	COO	[127]
	530.0	1.0	0.40	$TiO_{2-x}F_x$	[122]
	531.1	1.4	0.25	C-Ti-O_x and/or OR[b]	[105,128]
O 1s	532.3	1.6	0.18	C-Ti- $(OH)_x$ and/or OR[b]	[105]
	532.9	0.8	0.01	Al_2O_3 and/or OR[b]	[128-130]
	533.7	1.8	0.16	H_2O_{ads} and/or OR[b]	[105,128]
	684.9	1.5	0.26	C-Ti-F_x	[126]
F 1s	685.4	1.2	0.52	$TiO_{2-x}F_x$	[122]
	686.6	1.8	0.22	$Al(OF)_x$	[129]
Al 2p[c]	75.1	2.2	1.0	$Al(OF)_x$	[129]
	1066.2	3.0		TiO_2 (Auger LMM line)	[118]
Na 1s	1069.5	3.3		Ti-C (Auger LMM line)	[118]
	1072.2	1.7	1.0	Na^+ ions	[159,160]

[a] Values in parenthesis correspond to the $2p_{1/2}$ component.
[b] OR stands for organic compounds due to atmospheric surface contaminations.
[c] The spin orbit split for Al $2p_{3/2}$ and $2p_{1/2}$ were not resolved.

B4. XPS analysis for Li-$Ti_3C_2T_x$-HF/LiCl

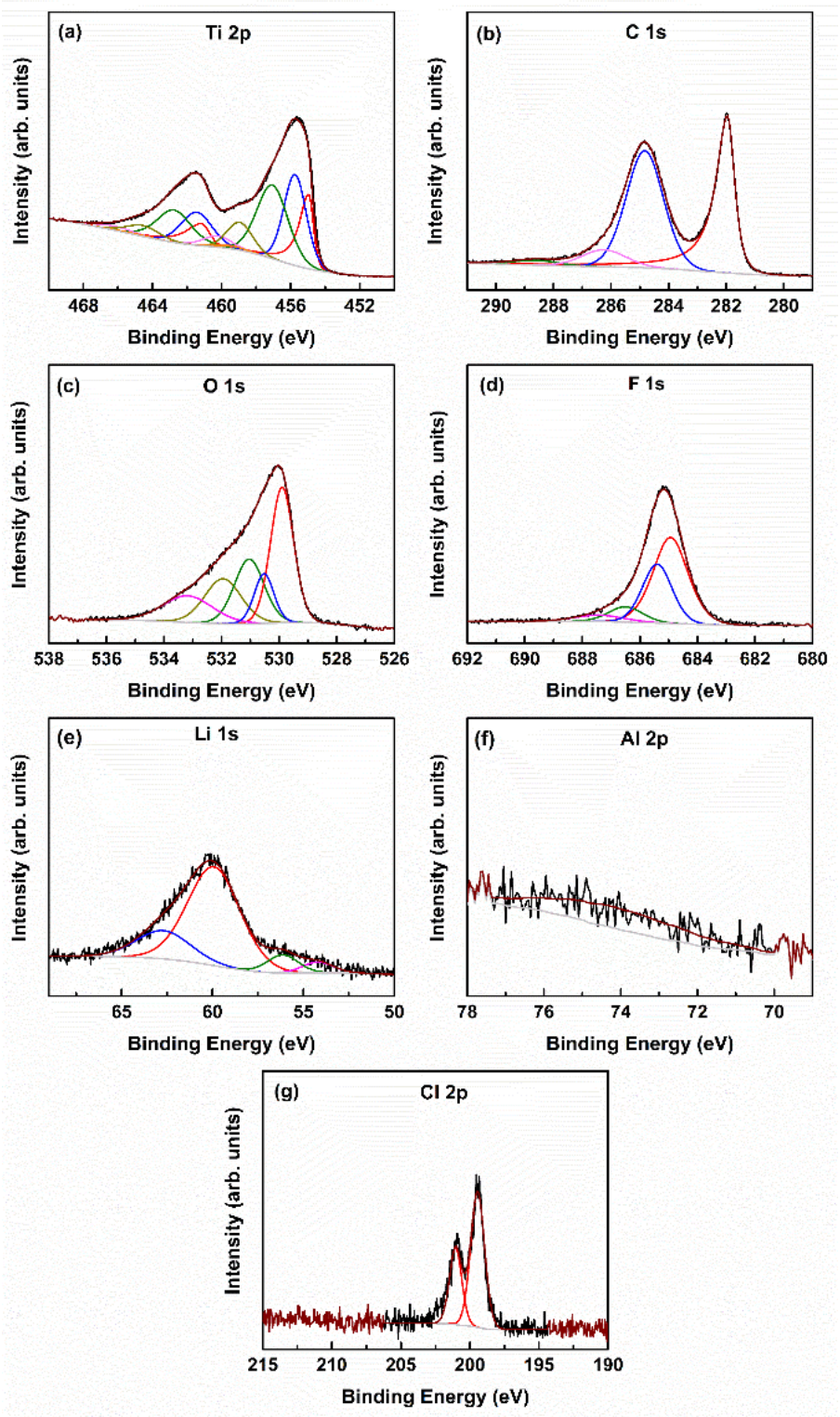

Figure 71. *XPS spectra with curve fitting for: (a) Ti 2p, (b) C 1s, (c) O 1s, (d) F 1s, (e) Li 1s, and (f) Al 2p regions for un-sputtered Li-$Ti_3C_2T_x$-HF/LiCl cold pressed disk. Various peaks shown represent various species assumed to exist. Labels and peak colors are coordinated. The results are summarized in* ***Table 22****.*

***Table 22**. Summary of XPS peak fitting results for un-sputtered ML Li-$Ti_3C_2T_x$-HF/LiCl cold pressed disk. The numbers in parenthesis in column 2 for the Ti 2p region are peak locations of* Ti $2p_{1/2}$*; their respective FWHMs are listed in column 3 in parenthesis.*

Region	BE [eV][a]	FWHM [eV][a]	Fraction	Assigned to	Reference
Ti $2p_{3/2}$ ($2p_{1/2}$)	455.0 (461.2)	0.7 (1.1)	0.19	(OH, or O)-Ti-C	[123,124]
	455.7 (461.4)	1.5 (2.1)	0.30	(OH, or O)-Ti^{2+}-C	[123]
	457.1 (462.8)	2.1 (2.3)	0.34	(OH, or O)-Ti^{3+}-C	[123]
	458.9 (464.6)	1.8 (2.2)	0.10	TiO_2	[120,121]
	459.5 (465.2)	1.8 (2.7)	0.01	$TiO_{2-x}F_x$	[122]
	460.2 (466.2)	1.9 (2.7)	0.06	C-Ti-F_x	[126]
C 1s	282.0	0.6	0.44	C-Ti-T_x	[123,124]
	284.8	1.5	0.46	C-C	[127]
	286.3	1.8	0.08	C-O	[127]
	288.6	1.8	0.02	COO	[127]
O 1s	529.9	0.9	0.35	TiO_2	[105,120]
	530.5	0.8	0.11	$TiO_{2-x}F_x$	[122]
	531.0	1.2	0.21	C-Ti-O_x and/or OR[b]	[105,128]
	532.0	1.5	0.18	C-Ti- $(OH)_x$ and/or OR[b]	[105]
	533.2	2.0	0.15	H_2O_{ads} and/or OR[b]	[105,128]
F 1s	684.9	1.4	0.54	C-Ti-F_x	[126]
	685.4	1.2	0.31	$TiO_{2-x}F_x$	[122]
	686.5	1.4	0.09	$Al(OF)_x$	[129]
	687.4	1.5	0.06	AlF_x	[129]
Al 2p[c]	74.2	4.4	1.0	AlF_x	[129]
Li 1s	54.2	2.0	0.37	Li-O/Li-OH	[168 169] [170]
	56.1	2.0	0.63	LiF/LiCl	[168 169]
	59.9	3.4		Ti-C (Ti 3s)	[168 169]
	62.7	3.5		TiO_2 (Ti 3s)	
Cl $2p_{3/2}$ ($2p_{1/2}$)	199.3 (200.9)	1.3 (1.1)	1.0	LiCl	[171]

[a] Values in parenthesis correspond to the $2p_{1/2}$ component.
[b] OR stands for organic compounds due to atmospheric surface contaminations.
[c] The spin orbit split for Al $2p_{3/2}$ and $2p_{1/2}$ were not resolved.

B5. XPS analysis for Li-$Ti_3C_2T_x$-HCl /LiF

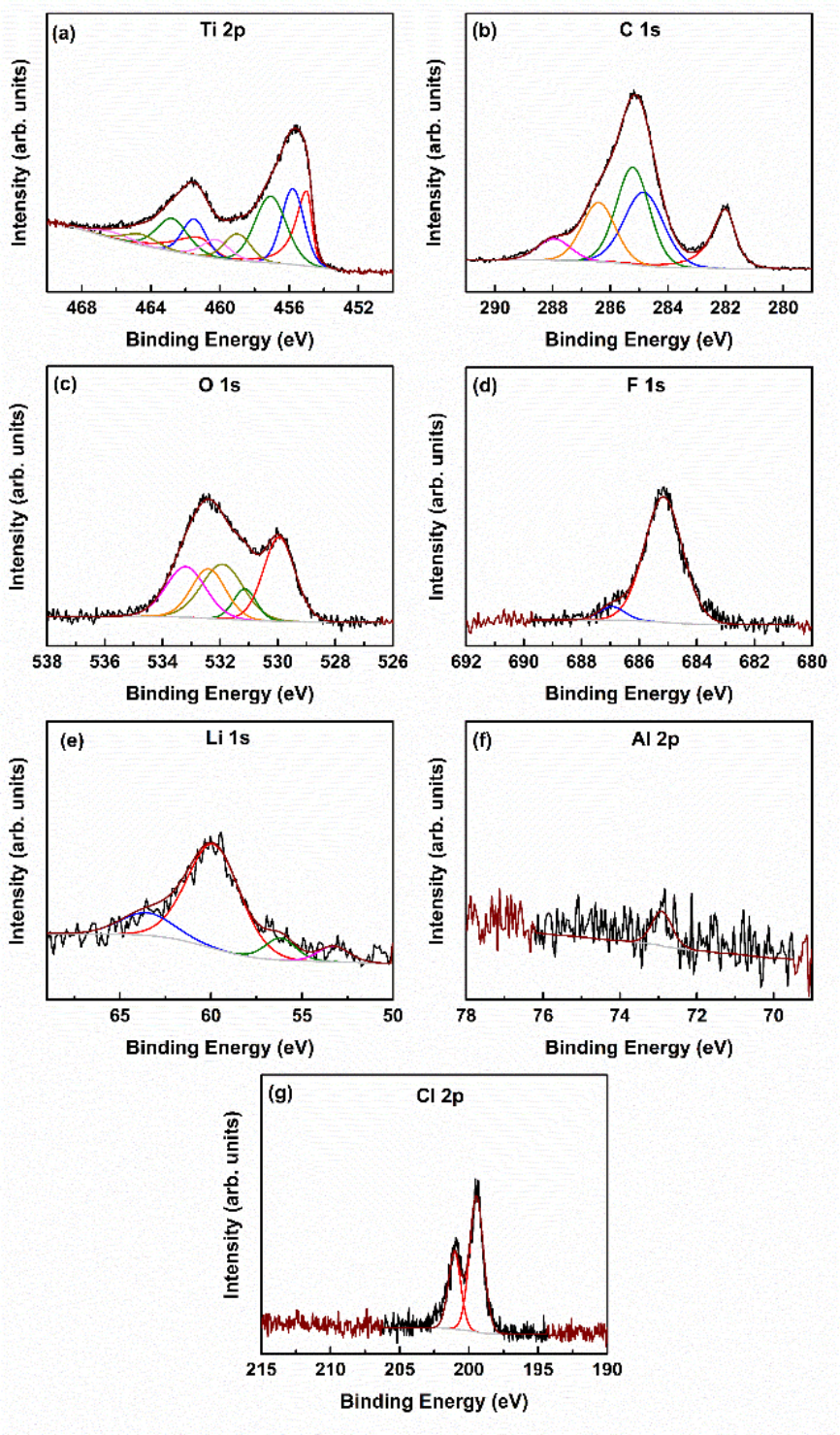

Figure 72. *XPS spectra with curve fitting for: (a) Ti 2p, (b) C 1s, (c) O 1s, (d) F 1s, (e) Li 1s, and (f) Al 2p regions for un-sputtered Li-$Ti_3C_2T_x$-HCl/LiF cold pressed disk. Various peaks shown represent various species assumed to exist. Labels and peak colors are coordinated. The results are summarized in* ***Table 23****.*

***Table 23**. Summary of XPS peak fitting results for un-sputtered ML Li-$Ti_3C_2T_x$-HCl/LiF cold pressed disk. The numbers in parenthesis in column 2 for the Ti 2p region are peak locations of* Ti $2p_{1/2}$*; their respective FWHMs are listed in column 3 in parenthesis.*

Region	BE [eV][a]	FWHM [eV][a]	Fraction	Assigned to	Reference
Ti $2p_{3/2}$ ($2p_{1/2}$)	455.0 (461.2)	0.8 (1.9)	0.23	(OH, or O)-Ti-C	[123,124]
	455.8 (461.5)	1.5 (1.6)	0.26	(OH, or O)-Ti^{2+}-C	[123]
	457.1 (462.8)	2.1 (2.1)	0.32	(OH, or O)-Ti^{3+}-C	[123]
	459.0 (464.6)	1.8 (2.2)	0.08	TiO_2 and/or $TiO_{2-x}F_x$	[120,121, 122]
	460.2 (466.2)	1.9 (2.7)	0.11	C-Ti-F_x	[126]
C 1s	282.0	0.8	0.17	C-Ti-T_x	[123,124]
	284.8	1.6	0.27	C-C	[127]
	285.2	1.4	0.31	CH_x	[127]
	286.4	1.4	0.19	C-O	[127]
	288.0	1.4	0.06	COO	[127]
O 1s	530.0	1.3	0.29	TiO_2 and/or $TiO_{2-x}F_x$	[105,120, 122]
	531.1	1.0	0.08	C-Ti-O_x and/or OR[b]	[105,128]
	531.9	1.7	0.24	C-Ti- $(OH)_x$ and/or OR[b]	[105]
	532.4	1.4	0.18	Al_2O_3 and/or OR[b]	[128-130]
	533.2	1.6	0.21	H_2O_{ads} and/or OR[b]	[105,128]
F 1s	685.2	1.6	0.93	C-Ti-F_x	[126]
	686.9	1.1	0.07	$TiO_{2-x}F_x$	[122]
Al 2p[c]	73.0	0.6	1.0	AlF_x	[129]
Li 1s	53.3	2.0	0.42	Li-O/Li-OH	[168 169] [170]
	56.2	2.0	0.58	LiF/LiCl	[168 169]
	59.9	3.4		Ti-C (Ti 3s)	[168 169]
	63.5	3.5		TiO_2 (Ti 3s)	
Cl $2p_{3/2}$ $2p_{1/2}$	199.4 (201.0)	1.2 (1.0)	1.0	LiCl	[171]

[a] Values in parenthesis correspond to the $2p_{1/2}$ component.
[b] OR stands for organic compounds due to atmospheric surface contaminations.
[c] The spin orbit split for Al $2p_{3/2}$ and $2p_{1/2}$ were not resolved.

Table 24. *Summary of elemental global at. % - including non-MXene entities – before sputtering.*

	Ti	C	F	O	Al	N	K	Na	Li	Cl
$Ti_3C_2T_x$-10HF	29.1±0.8	35.5±0.9	13.9±0.4	20.9±0.6	0.6±0.2	< 0.1				
K-$Ti_3C_2T_x$-50HF	19.3±0.7	37.2±0.8	14.2±0.7	18.9±0.9	1.9±0.7	< 0.1	4.3±0.3			
Na-$Ti_3C_2T_x$-50HF	20.5±1.1	26.3±1.3	12.3±0.2	11.4±0.4	1.1±0.3	< 0.1		4.1±0.5		
Li-$Ti_3C_2T_x$-HF/LiCl	25.0±1.2	36.4±1.1	10.9± 0.9	21.0±0.3	0.6±0.4	< 0.1			5.7±0.5	0.4±0.2
Li-$Ti_3C_2T_x$-HCl/LiF	14.3±0.2	53.0±1.8	6.8±0.3	14.9±0.9	0.5±0.1	< 0.1			9.0±1.0	1.5±0.3

LIST OF REFERENCES

1 Novoselov, K. S. *et al.* Electric field effect in atomically thin carbon films. *Science* **306**, 666-669 (2004).

2 Geim, A. K. *et al* The rise of graphene. *Nat. Mater.* **6**, 183-191 (2007).

3 Bianco, A. *et al.* All in the graphene family – A recommended nomenclature for two-dimensional carbon materials. *Carbon* **65**, 1-6 (2013).

4 Balandin, A. A. *et al.* Superior thermal conductivity of single-layer graphene. *Nano Lett.* **8**, 902-907 (2008).

5 Lee, C., *et al*. Measurement of the Elastic Properties and Intrinsic Strength of Monolayer Graphene. *Science* **321**, 385-388 (2008).

6 Nair, R. R. *et al.* Fine structure constant defines visual transparency of graphene. *Science* **320**, 1308 (2008).

7 Moon, J. *et al.* Top-gated epitaxial graphene FETs on Si-face SiC wafers with a peak transconductance of 600 mS/mm. *Electron Device Letters, IEEE* **31**, 260-262 (2010).

8 Lin, Y. M. *et al.* 100-GHz Transistors from wafer-scale epitaxial graphene. *Science* **327**, 662-662 (2010).

9 Liu, J. *et al.* Multilayer stacked low-temperature-reduced graphene oxide Films: preparation, Characterization, and Application in Polymer Memory Devices. *Small* **6**, 1536-1542 (2010).

10 Tian, H. *et al.* Memory devices: in situ tuning of switching window in a gate-controlled bilayer graphene-electrode resistive memory device. *Adv. Mater.* **27**, 7766-7766 (2015).

11 Gomez De Arco, L. *et al.* Continuous, highly flexible, and transparent graphene films by chemical vapor deposition for organic photovoltaics. *ACS Nano* **4**, 2865-2873 (2010).

12 Bae, S. *et al.* Roll-to-roll production of 30-inch graphene films for transparent electrodes. *Nat. Nanotechnol.* **5**, 574-578 (2010).

13 Kobayashi, T. *et al.* Production of a 100-m-long high-quality graphene transparent conductive film by roll-to-roll chemical vapor deposition and transfer process. *Appl. Phys. Lett.* **102**, 023112-023114 (2013).

14 Sun, S., *et al*. Enhanced dye-sensitized solar cell using graphene-TiO_2 photoanode prepared by heterogeneous coagulation. *Appl. Phys. Lett.* **96**, 083113-083115, (2010).

15 Yan, X., *et al*. Large, solution-processable graphene quantum dots as light absorbers for photovoltaics. *Nano Lett.* **10**, 1869-1873 (2010).

16 Dan, Y. *et al*. A. C. Intrinsic response of graphene vapor sensors. *Nano Lett.* **9**, 1472-1475 (2009).

17 Wang, C. *et al.* A label-free and portable graphene FET aptasensor for children blood lead detection. *Scientific reports* **6**, 21711-2178 (2016).

18 Wu, S., *et al.* Graphene-based electrochemical sensors. *Small* **9**, 1160-1172 (2013).

19 Pacilé, D., *et al.* A. The two-dimensional phase of boron nitride: Few-atomic-layer sheets and suspended membranes. *Appl. Phys. Lett.* **92**, 133107-133109 (2008).

20 Dean, C. *et al.* Boron nitride substrates for high-quality graphene electronics. *Nat. Nanotechnol.* **5**, 722-726 (2010).

21 Coleman, J. N. *et al.* Two-dimensional nanosheets produced by liquid exfoliation of layered materials. *Science* **331**, 568-571, (2011).

22 Ma, R. *et al.* T. Nanosheets of oxides and hydroxides: Ultimate 2D charge-bearing functional crystallites. *Adv. Mater.* **22**, 5082-5104, (2010).

23 Vogt, P. *et al.* Silicene: compelling experimental evidence for graphenelike two-dimensional silicon. *Phys. Rev. Lett.* **108**, 155501-155503 (2012).

24 Liu, H. *et al.* Phosphorene: an unexplored 2D semiconductor with a high hole mobility. *ACS Nano* **8**, 4033-4041 (2014).

25 Dávila, M. *et al.* Germanene: a novel two-dimensional germanium allotrope akin to graphene and silicene. *New Journal of Physics* **16**, 095002-095012 (2014).

26 Liu, Z. *et al.* Functionalized graphene and other two-dimensional materials for photovoltaic devices: device design and processing. *Chem. Soc. Rev.* **44**, 5638-5679 (2015).

27 Giovannetti, G. *et al.* Doping graphene with metal contacts. *Phys. Rev. Lett.* **101**, 026803-026806 (2008).

28 Kasry, A., *et al.* Chemical doping of large-area stacked graphene films for use as transparent, conducting electrodes. *ACS Nano* **4**, 3839-3844 (2010).

29 Pei, S. *et al.* Direct reduction of graphene oxide films into highly conductive and flexible graphene films by hydrohalic acids. *Carbon* **48**, 4466-4474 (2010).

30 Yu, W. *et al.* Toward tunable band gap and tunable dirac point in bilayer graphene with molecular doping. *Nano Lett.* **11**, 4759-4763 (2011).

31 Yan, Z. *et al.* Controlled ambipolar-to-unipolar conversion in graphene field-effect transistors through surface coating with poly (ethylene imine)/poly (ethylene glycol) films. *Small* **8**, 59-62 (2012).

32 Blake, P. *et al.* Graphene-based liquid crystal device. *Nano Lett.* **8**, 1704-1708 (2008).

33 Zhou, Y. *et al.* A universal method to produce low–work function electrodes for organic electronics. *Science* **336**, 327-332 (2012).

34 Jo, G. *et al.* Tuning of a graphene-electrode work function to enhance the efficiency of organic bulk heterojunction photovoltaic cells with an inverted structure. *Appl. Phys. Lett.* **97**, 213301 (2010).

35 Tongay, S. *et al.* Broad-range modulation of light emission in two-dimensional semiconductors by molecular physisorption gating. *Nano Lett.* **13**, 2831-2836 (2013).

36 Fang, H. *et al.* High-performance single layered WSe_2 p-FETs with chemically doped contacts. *Nano Lett.* **12**, 3788-3792 (2012).

37 Lin, J. D. *et al.* Electron-doping-enhanced trion formation in monolayer molybdenum disulfide functionalized with cesium carbonate. *ACS Nano* **8**, 5323-5329 (2014).

38 Mouri, S., Miyauchi, Y. & Matsuda, K. Tunable photoluminescence of monolayer MoS_2 via chemical doping. *Nano Lett.* **13**, 5944-5948 (2013).

39 Naguib, M. *et al.* Two-dimensional nanocrystals produced by exfoliation of Ti_3AlC_2. *Adv. Mater.* **23**, 4248-4253 (2011).

40 Naguib, M. *et al.* Two-dimensional transition metal carbides. *ACS Nano* **6**, 1322-1331 (2012).

41 Barsoum, M. W. *MAX Phases: Properties of Machinable Ternary Carbides and Nitrides*. (John Wiley & Sons 2013).

42 Ghidiu, M. *et al.* Conductive two-dimensional titanium carbide 'clay' with high volumetric capacitance. *Nature* **516**, 78-81 (2014).

43 Lukatskaya, M. R. *et al.* Cation intercalation and high volumetric capacitance of two-dimensional titanium carbide. *Science* **341**, 1502-1505 (2013).

44 Er, D. *et al.* Ti_3C_2 MXene as a high capacity electrode material for metal (Li, Na, K, Ca) ion batteries. *ACS Appl. Mater. Interfaces* **6**, 11173-11179 (2014).

45 Naguib, M. *et al.* New two-dimensional niobium and vanadium carbides as promising materials for Li-ion batteries. *J. Am. Chem. Soc.* **135**, 15966-15969 (2013).

46 Mashtalir, O., *et al.* Amine-assisted delamination of Nb_2C MXene for Li-Ion energy storage devices. *Adv. Mater.* **27**, 3501-3506 (2015).

47 Peng, Q. *et al.* Unique lead adsorption behavior of activated hydroxyl group in two-dimensional titanium carbide. *J. Am. Chem. Soc.* **136**, 4113-4116, (2014).

48 Ren, C. E. *et al.* Charge- and size-selective ion sieving through $Ti_3C_2T_x$ MXene Membranes. *The Journal of Physical Chemistry Letters* **6**, 4026-4031, (2015).

49 Come, J. *et al.* Controlling the actuation properties of MXene paper electrodes upon cation intercalation. *Nano Energy* **17**, 27-35 (2015).

50 Mashtalir, O. *et al.* Dye adsorption and decomposition on two-dimensional titanium carbide in aqueous media. *Journal of Materials Chemistry A* **2**, 14334-14338 (2014).

51 Halim, J. *et al.* Transparent conductive two-dimensional titanium carbide epitaxial thin films. *Chem. Mater.* **26**, 2374-2381 (2014).

52 Chen, J. *et al.* CO_2 and temperature dual responsive "Smart" MXene phases. *Chem. Commun. (Cambridge, U. K.)* **51**, 314-317 (2015).

53 Naguib, M., *et al.* 25th-anniversary article: MXenes: a new family of two-dimensional materials. *Adv. Mater.* **26**, 992-1005 (2014).

54 Khazaei, M. *et al.* Novel electronic and magnetic properties of two-dimensional transition metal carbides and nitrides. *Adv. Funct. Mater.* **23**, 2185-2192 (2013).

55 Khazaei, M. *et al.* Two-dimensional molybdenum carbides: potential thermoelectric materials of the MXene family. *Phys. Chem. Chem. Phys.* **16**, 7841-7849, (2014).

56 Xie, Y. *et al.* Hybrid density functional study of structural and electronic properties of functionalized $Ti_{n+1}X_n$ (X= C, N) monolayers. *Phys Rev B* **87**, 235441-2354450 (2013).

57 Xie, Y. *et al.* Role of surface structure on Li-ion energy storage capacity of two-dimensional transition-metal carbides. *J. Am. Chem. Soc.* **136**, 6385-6394 (2014).

58 Bose, S. *et al.* In-situ synthesis and characterization of electrically conductive polypyrrole/graphene nanocomposites. *Polymer* **51**, 5921-5928 (2010).

59 Das, A. *et al.* Monitoring dopants by Raman scattering in an electrochemically top-gated graphene transistor. *Nat. Nanotechnol.* **3**, 210-215 (2008).

60 Sheng, Z.-H. *et al.* Catalyst-free synthesis of nitrogen-doped graphene via thermal annealing graphite oxide with melamine and its excellent electrocatalysis. *ACS Nano* **5**, 4350-4358 (2011).

61 Shi, Y. *et al.* Selective decoration of Au nanoparticles on monolayer MoS_2 Single Crystals. *Scientific Reports* **3**, 1839-1841 (2013).

62 Lei, S. *et al.* Surface functionalization of two-dimensional metal chalcogenides by Lewis acid–base chemistry. *Nat Nano* **11**, 465-471 (2016).

63 Miranda, A. *et al.* A. Electronic properties of freestanding $Ti_3C_2T_x$ MXene monolayers. *Appl. Phys. Lett.* **108**, 033102-033105 (2016).

64 Mashtalir, O. *et al.* Intercalation and delamination of layered carbides and carbonitrides. *Nature communications* **4**, 1716-1722 (2013).

65 Naguib, M., *et al.* Large-scale delamination of multi-layers transition metal carbides and carbonitrides "MXenes". *Dalton Trans.* **44**, 9353-9358, (2015).

66 Enyashin, A. N. *et al.* Structural and electronic properties and stability of MXenes Ti_2C and Ti_3C_2 functionalized by methoxy groups. *The Journal of Physical Chemistry C* **117**, 13637-13643 (2013).

67 Naguib, M. *et al.* MXene: a promising transition metal carbide anode for lithium-ion batteries. *Electrochem. Commun.* **16**, 61-64 (2012).

68 Tang, Q., Zhou, Z. & Shen, P. Are MXenes promising anode materials for Li ion batteries? Computational studies on electronic properties and Li storage capability of Ti_3C_2 and $Ti_3C_2X_2$ (X = F, OH) monolayer. *J. Am. Chem. Soc.* **134**, 16909-16916, (2012).

69 Sun, D. *et al.* Two-dimensional Ti_3C_2 as anode material for Li-ion batteries. *Electrochem. Commun.* **47**, 80-83 (2014).

70 Eames, C. *et al.* Ion intercalation into two-dimensional transition-metal carbides: Global screening for new high-capacity battery materials. *J. Am. Chem. Soc.* **136**, 16270-16276 (2014).

71 Come, J. *et al.* A Non-Aqueous Asymmetric Cell with a Ti2C-Based Two-Dimensional Negative Electrode. *J. Electrochem. Soc.* **159**, A1368-A1373, (2012).

72 Dall'Agnese, Y., *et al.* Two-dimensional vanadium carbide (MXene) as positive electrode for sodium-ion capacitors. *The journal of physical chemistry letters* **6**, 2305-2309 (2015).

73 Wang, X. *et al.* Pseudocapacitance of MXene nanosheets for high-power sodium-ion hybrid capacitors. *Nature communications* **6** (2015).

74 Dall'Agnese, Y. *et al.* High capacitance of surface-modified 2D titanium carbide in acidic electrolyte. *Electrochem. Commun.* **48**, 118-122, (2014).

75 Rakhi, R. *et al.* Effect of postetch annealing gas composition on the structural and electrochemical Properties of Ti_2CT_x MXene Electrodes for Supercapacitor Applications. *Chem. Mater.* **27**, 5314-5323 (2015).

76 Yu, X.-f. *et al.* Monolayer Ti_2CO_2: a promising candidate for NH_3 Sensor or capturer with high sensitivity and selectivity. *ACS Appl. Mater. Interfaces* **7**, 13707-13713 (2015).

77 Liu, H. *et al.* A novel nitrite biosensor based on the direct electrochemistry of hemoglobin immobilized on MXene-Ti_3C_2. *Sensors and Actuators B: Chemical* **218**, 60-66 (2015).

78 Ying, Y. *et al.* Two-dimensional titanium carbide for efficiently reductive removal of highly toxic chromium (VI) from Water. *ACS Appl. Mater. Interfaces* **7**, 1795-1803 (2015).

79 Xie, X., , Ding, W., Nie, Y. & Wei, Z. in *Chem. Commun. (Cambridge, U. K.)* **49**, 10112-10114 (2013).

80 Ingason, A. S. *et al.* A nanolaminated magnetic phase: Mn_2GaC. *Materials Research Letters* **2**, 89-93 (2014).

81 Kuchida, S. *et al.* Superconductivity in Lu< sub> 2</sub> SnC. *Physica C: Superconductivity* **494**, 77-79 (2013).

82 Barsoum, M. W. The $M_{N+1}AX_N$ phases: A new class of solids : Thermodynamically stable nanolaminates. *Prog. Solid State Chem.* **28**, 201-281 (2000).

83 Magnuson, M. *et al.* Electronic structure investigation of Ti_3AlC_2, Ti_3SiC_2, and Ti_3GeC_2 by soft x-ray emission spectroscopy. *Phys Rev B* **72**, 245101 (2005).

84 Eklund, P. *et al.*The $M_{n+1}AX_n$ phases: Materials science and thin-film processing. *Thin Solid Films* **518**, 1851-1878 (2010).

85 Ghidiu, M. *et al.* Ion-exchange and cation solvation reactions in Ti_3C_2 MXene. *Chem. Mater.* **28**, 3507-3514 (2016).

86 Ghidiu, M. *et al.* Synthesis and characterization of two-dimensional Nb_4C_3 (MXene). *Chem. Commun. (Cambridge, U. K.)*,**50**, 9517-9520 (2014).

87 Zhou, J. *et al.* A two-dimensional zirconium carbide by selective etching of Al_3C_3 from nanolaminated $Zr_3Al_3C_5$. *Angew. Chem.* **128**, 5092-5097 (2016).

88 Yang, J. *et al.* Two-dimensional Nb-based M_4C_3 solid solutions (MXenes). *J. Am. Ceram. Soc.* **99**, 660-666 (2015).

89 Anasori, B. *et al.* Two-dimensional, ordered, double transition metals carbides (MXenes). *ACS Nano*, **9**, 9507-9516 (2015).

90 Shein, I. *et al.* A. Graphene-like titanium carbides and nitrides $Ti_{n+1}C_n$, $Ti_{n+1}N_n$(n = 1, 2, and 3) from de-intercalated MAX phases: First-principles probing of their structural, electronic properties and relative stability. *Computational Materials Science* **65**, 104-114 (2012).

91 Tang, Q. *et al.* Are MXenes promising anode materials for Li ion batteries? Computational studies on electronic properties and Li storage capability of Ti_3C_2 and $Ti_3C_2X_2$ (X= F, OH) Monolayer *J. Am. Chem. Soc.* **134**, 16909-16916 (2012).

92 Khazaei, M. *et al.* Novel electronic and magnetic properties of two-dimensional transition metal carbides and nitrides. *Adv. Funct. Mater.* **23**, 2185-2192 (2012).

93 Enyashin, A. *et al.* 2D titanium carbonitrides and their hydroxylated derivatives: Structural, electronic properties and stability of MXenes $Ti_3C_{2-x}N_x$ and $Ti_3C_{2-x}N_x(OH)_2$. *J. Solid State Chem.* **207**, 42-48 (2013).

94 Shein, I. R. *et al.* Planar nano-block structures $Ti_{n+1}Al_{0.5}C_n$ and $Ti_{n+1}C_n$ (n = 1, and 2) from MAX phases: Structural, electronic properties and relative stability from first principles calculations. *Superlattices Microstruct.* **52**, 147-157 (2012).

95 Enyashin, A. N. *et al.* Atomic structure, comparative stability and electronic properties of hydroxylated Ti_2C and Ti_3C_2 nanotubes. *Computational and Theoretical Chemistry* **989**, 27-32 (2012).

96 Bai, Y. *et al.* Dependence of elastic and optical properties on surface terminated groups in two-dimensional MXene monolayers: a first-principles study. *RSC Advances* **6**, 35731-35739 (2016).

97 Anasori, B. *et al.* Control of electronic properties of 2D carbides (MXenes) by manipulating their transition metal layers. *Nanoscale Horizons* **1**, 227-234 (2016).

98 Karlsson, L. *et al.* Atomically resolved structural and chemical investigation of single MXene sheets. *Nano Lett.* **15**, 4955-4960 (2015).

99 Lukatskaya, M. R. *et al.* Probing the mechanism of high capacitance in 2D titanium carbide using in situ X-ray absorption spectroscopy. *Advanced Energy Materials* **5**, 1500589-1500562 (2015).

100 Shi, C. *et al.* Structure of nanocrystalline Ti_3C_2 MXene using atomic pair distribution function. *Phys. Rev. Lett.* **112**, 125501 (2014).

101 Wang, H.-W. *et al.* Resolving the Structure of Ti3C2T x MXenes through Multilevel Structural Modeling of the Atomic Pair Distribution Function. *Chem. Mater.* **28**, 349-359 (2015).

102 Henderson, M. A. The interaction of water with solid surfaces: fundamental aspects revisited. *Surf. Sci. Rep.* **46**, 1-308 (2002).

103 Diebold, U. The surface science of titanium dioxide. *Surf. Sci. Rep.* **48**, 53-229 (2003).

104 Lane, C. D., *et al.* Electron-stimulated oxidation of thin water films adsorbed on TiO_2 (110). *The Journal of Physical Chemistry C* **111**, 16319-16329 (2007).

105 Yamamoto, S. *et al.* In situ x-ray photoelectron spectroscopy studies of water on metals and oxides at ambient conditions. *J Phys-Condens Mat* **20**, 184025-184038 (2008).

106 Sham, T. *et al.* M. X-ray photoelectron spectroscopy (XPS) studies of clean and hydrated TiO 2 (rutile) surfaces. *Chem. Phys. Lett.* **68**, 426-432 (1979).

107 Wang, L.-Q. *et al.* The adsorption of liquid and vapor water on TiO_2 (110) surfaces: the role of defects. *Surf. Sci.* **344**, 237-250 (1995).108

108 Wang, L.-Q. *et al.* The adsorption of liquid and vapor water on TiO_2 (110) surfaces: the role of defects. *Surf. Sci.* **344**, 237-250 (1995).

109 Wendt, S. *et al.* Formation and splitting of paired hydroxyl groups on reduced TiO_2 (110). *Phys. Rev. Lett.* **96**, 066107-066110 (2006).

110 Bikondoa, O. *et al.* Direct visualization of defect-mediated dissociation of water on TiO_2 (110). *Nat. Mater.* **5**, 189-192 (2006).

111 Frantz, P. *et al.* S. V. Detailed spectroscopic studies of oxygen on metal carbide surfaces. *Surf. Sci.* **412**, 384-396 (1998).

112 Merrill, P. *et al.* Adsorption of water on TiC (100): Evidence for complex reaction and desorption pathways. *The Journal of Physical Chemistry B* **102**, 7606-7612 (1998).

113 Didziulis, S. V. *et al.* Substrate-dependent reactivity of water on metal carbide surfaces. *The Journal of Physical Chemistry B* **103**, 11129-11140 (1999).

114 Halim, J. *et al.* X-ray photoelectron spectroscopy of select multi-layered transition metal carbides (MXenes). *Appl. Surf. Sci.* **362**, 406-417 (2016).

115 Van der Heide, P. *X-ray photoelectron spectroscopy: an introduction to principles and practices*. (John Wiley & Sons, 2011).

116 Wagner, C. *et al.* Empirical atomic sensitivity factors for quantitative analysis by electron spectroscopy for chemical analysis. *Surf. Interface Anal.* **3**, 211-225 (1981).

117 Biesinger, M. *et al.* Resolving surface chemical states in XPS analysis of first row transition metals, oxides and hydroxides: Sc, Ti, V, Cu and Zn. *Appl. Surf. Sci.* **257**, 887-898 (2010).

118 Briggs, D. *et al.* Practical surface analysis by Auger and X-ray photoelectron spectroscopy. *D. Briggs, & M. P. Seah,(Editors), John Wiley & Sons, Chichester* (1983).

119 Briggs, D. XPS: basic principles, spectral features and qualitative analysis. *Surface Analysis by Auger and X-ray Photoelectron Spectroscopy, Cromwell Press, Trowbridge*, 37-38 (2003).

120 Diebold, U. TiO_2 by XPS. *Surface Science Spectra* **4**, 227 (1996).

121 Santerre, F. *et al.* Properties of TiC thin films grown by pulsed laser deposition. *Appl. Surf. Sci.* **148**, 24-33 (1999).

122 Tanuma, T. *et al.* Partially Fluorinated Metal Oxide Catalysts for a Friedel–Crafts-type Reaction of Dichlorofluoromethane with Tetrafluoroethylene. *Catal. Lett.* **136**, 77-82 (2009).

123 Schier, V. *et al.* J. ARXPS-analysis of sputtered TiC, SiC and $Ti_{0.5}Si_{0.5}C$ layers. *Fresenius J Anal Chem* **346**, 227-232 (1993).

124 Myhra, S. *et al.* Crystal-chemistry of the Ti_3AlC_2 and Ti_4AlN_3 layered carbide/nitride phases - characterization by XPS. *J. Phys. Chem. Solids* **62**, 811-817 (2001).

125 Lukatskaya, M. R. *et al.* Room-temperature carbide-derived carbon synthesis by electrochemical etching of MAX phases. *Angew Chem Int Ed Engl* **53**, 4877-4880 (2014).

126 Sultana, T. *et al.* XPS analysis of laser transmission micro-joint between poly (vinylidene fluoride) and titanium. *Appl. Surf. Sci.* **255**, 2569-2573 (2008).

127 Jayaweera, P. M. *et al.* Photoreaction of ethanol on TiO_2(110) single-crystal surface. *J. Phys. Chem. C* **111**, 1764-1769 (2007).

128 Beamson, G. *et al. High Resolution XPS of Organic Polymers: The Scienta ESCA300 Database*. (Wiley, 1992).

129 Ernst, K. H. *et al.* Fluorine-induced corrosion of aluminum microchip bond pads - an XPS and AES analysis. *Surf. Interface Anal.* **21**, 691-696 (1994).

130 Popova, I. *et al.* Depth-dependent electrical impedance distribution in Al_2O_3 films on Al(111)-detection of an inner barrier layer. *Langmuir* **16**, 10309-10314 (2000).

131 Guemmaz, M. *et al.* Band structure of substoichiometric titanium nitrides and carbonitrides: spectroscopical and theoretical investigations. *J. Phys.: Condens. Matter* **9**, 8453-8463 (1997).

132 Cheng, Y. *et al.* Characterization of TiN, TiC and TiCN coatings on Ti–50.6 at.% Ni alloy deposited by PIII and deposition technique. *Surf. Coat. Technol.* **201**, 4909-4912 (2007).

133 Sexton, B. A. *et al.* Coordination of acetonitrile (CH_3CN) to platinum (111): Evidence for an η_2(C,N) species. *Surf. Sci.* **129**, 21-36 (1983).

134 Barbaray, B. *et al.* Effects of nitrogen dioxide and water vapor on oxidation of sulfur dioxide over vanadium pentoxide particles. *Environ. Sci. Technol.* **12**, 1294-1297 (1978).

135 Halbritter, J. *et al.* Angle resolved XPS studies of oxides at Nb-, NbN-, NbC- and Nb_3Sn- Surfaces. *IEEE Trans. Magn.* **23**, 1381-1384 (1987).

136 Romero, R. *et al.* D. Nb_2O_5 thin films obtained by chemical spray pyrolysis. *Surf. Interface Anal.* **36**, 888-891 (2004).

137 Chen, L. *et al.* Bipolar resistive switching characteristics of atomic layer deposited Nb_2O_5 thin films for nonvolatile memory application. *Current Applied Physics* **11**, 849-852 (2011).

138 Guo, S. Q. *et al.* Facile preparation of hierarchical Nb_2O_5 microspheres with photocatalytic activities and electrochemical properties. *Journal of Materials Chemistry A* **2**, 9236-9243 (2014).

139 Luo, Y., Wang *et al.* Hydrogen sorption kinetics of MgH_2 catalyzed with NbF_5. *J. Alloys Compd.* **453**, 138-142 (2008).

140 Marques, M. *et al.* XRD, XPS and SEM characterisation of Cu–NbC nanocomposite produced by mechanical alloying. *Mater. Chem. Phys.* **109**, 174-180 (2008).

141 Miller, C. *et al.*High temperature oxidation of Nb, NbC and Ni_3Nb and oxygen enhanced crack growth. *Scr. Mater.* **42**, 227-232 (2000).

142 Weibin, Z. *et al.* The investigation of NbO2 and Nb2O5 electronic structure by XPS, UPS and first principles methods. *Surf. Interface Anal.* **45**, 1206-1210 (2013).

143 Dacca, A. *et al.* XPS analysis of the surface composition of niobium for superconducting RF cavities. *Appl. Surf. Sci.* **126**, 219-230 (1998).

144 Choi, J.-G. The surface properties of vanadium compounds by X-ray photoelectron spectroscopy. *Appl. Surf. Sci.* **148**, 64-72 (1999).

145 Groult, H. *et al.* Vanadium oxide fluoride-Ggaphite intercalation compounds: structural characteristics and electrochemical insertion of lithium cations. *J. Electrochem. Soc.* **143**, 2093-2099 (1996).

146 Hu, C. *et al.* On the rapid synthesis of the ternary Mo_2GaC. *J. Am. Ceram. Soc.* **98**, 2713-2715 (2015).

147 Hu, C. *et al.* Mo 2 Ga 2 C: a new ternary nanolaminated carbide. *Chem. Commun. (Cambridge, U. K.)* **51**, 6560-6563 (2015).

148 Lai, C. C. *et al.* Structural and chemical determination of the new nanolaminated carbide Mo_2Ga_2C from first principles and materials analysis. *Acta Mater.* **99**, 157-164 (2015).

149 Óvári, L. *et al.* Surface and subsurface oxidation of Mo_2C/Mo(100): low-energy ion-scattering, Auger electron, angle-resolved X-ray photoelectron, and mass spectroscopy studies. *The Journal of Physical Chemistry B* **109**, 4638-4645 (2005).

150 Park, S. j., Sun, C. p. & Purtell, R. A mechanistic study of SF_6/O_2 reactive ion etching of molybdenum. *Journal of Vacuum Science & Technology B* **5**, 1372-1373 (1987).

151 Kiwi-Minsker, L. *et al.* A. Microstructured reactors for catalytic reactions. *Catal. Today* **110**, 2-14 (2005).

152 Anasori, B. *et al.* Experimental and theoretical characterization of ordered MAX phases Mo_2TiAlC_2 and $Mo_2Ti_2AlC_3$. *J. Appl. Phys.* **118**, 094304-094313 (2015).

153 Anasori, B. *et al.* Mo_2TiAlC_2: A new ordered layered ternary carbide. *Scr. Mater.* **101**, 5-7 (2015).

154 Etzkorn, J. *et al.* V_2AlC, V_4AlC_{3-x} (x = 0.31), and $V_{12}Al_3C_8$: synthesis, crystal growth, structure, and superstructure. *Inorg. Chem.* **46**, 7646-7653 (2007).

155 Sun, Z. *et al.* J. M. Calculated elastic properties of M_2AlC (M= Ti, V, Cr, Nb and Ta). *Solid State Commun.* **129**, 589-592 (2004).

156 Lewin, E. *et al.* Influence of sputter damage on the XPS analysis of metastable nanocomposite coatings. *Surf. Coat. Technol.* **204**, 455-462 (2009).

157 Dall'Agnese, Y. *et al.* High capacitance of surface-modified 2D titanium carbide in acidic electrolyte. *Electrochem. Commun.* **48**, 118-122 (2014).

158 Ren, C. E. *et al.* Porous Two-Dimensional Transition Metal Carbide (MXene) Flakes for High-Performance Li-Ion Storage. *ChemElectroChem* **3**, 689-693 (2016).

159 Citrin, P. High-resolution X-ray photoemission from sodium metal and its hydroxide. *Phys Rev B* **8**, 5545-5556 (1973).

160 Nefedov, V. *et al.* A comparison of different spectrometers and charge corrections used in X-ray photoelectron spectroscopy. *J. Electron Spectrosc. Relat. Phenom.* **10**, 121-124 (1977).

161 Guo, C. *et al.* Near-infrared absorption properties of Rb_xWO_3 nanoparticles. *CrystEngComm* **14**, 7727-7732 (2012).

162 Hope, M. A. *et al.* NMR reveals the surface functionalisation of Ti_3C_2 MXene. *Phys. Chem. Chem. Phys.* **18**, 5099-5102 (2016).

163 Wang, L. *et al.* Loading actinides in multi-layered structures for nuclear waste treatment: the first case study of uranium capture with vanadium carbide MXene. *ACS Appl. Mater. Interfaces* DOI: 10.1021/acsami.6b02989 (2016).

164 Harris, K. J. *et al.* Direct measurement of surface termination groups and their connectivity in the 2D MXene V_2CT_x using NMR spectroscopy. *The Journal of Physical Chemistry C* **119**, 13713-13720 (2015).

165 Halim, J. *et al.* Synthesis and characterization of 2D molybdenum carbide (MXene). *Adv. Funct. Mater.* **26**, 3118-3127 (2016).

166 Khazaei, M. *et al.* OH terminated two-dimensional transition metal carbides and nitrides (MXenes) as ultralow work function materials. *Phys. Rev. B* **92**, 075411-075420 (2015).

167 Caballero, A. *et al.* Adsorption and oxidation of K deposited on graphite. *Surf. Sci.* **364**, 253-265 (1996).

168 Theng, B. *et al.* Nuclear magnetic resonance and X-ray photoelectron spectroscopic investigation of lithium migration in montmorillonite. *Clays Clay Miner.* **45**, 718-723 (1997).

169 Ebina, T. *et al.* XPS and DFT study on the migration of lithium in montmorillonite. *Clay Science* **10**, 569-581 (1999).

170 Niehoff, P. *et al.* Interface investigations of a commercial lithium ion battery graphite anode material by sputter depth profile X-ray photoelectron spectroscopy. *Langmuir* **29**, 5806-5816 (2013).

171 Kanamura, K. *et al.* XPS analysis of a lithium surface immersed in propylene carbonate solution containing various salts. *J. Electroanal. Chem.* **333**, 127-142 (1992).

VITA

Joseph Halim
E-mail: joseph.n.ernest@gmail.com
https://scholar.google.se/citations?user=ZAst3GEAAAAJ&hl=en

EDUCATION

Drexel University, **Philadelphia, PA, USA**
PhD, Materials Science and Engineering *01/2012-06/2016*
Linköping University, **Linköping, Sweden**
Licentiate, Thin Film Physics *02/2012-10/2014*
Cairo University, Giza, Egypt
M.S., Metallurgical Engineering, *09/2009-04/2011*
B.S., Metallurgical Engineering, with Honors Degree *09/2004-07/2009*

PUBLICATIONS

1. A. Byeon, MQ Zhao, CE Ren, **J. Halim**, S. Kota, P. Urbankowski, B. Anasori, M.W. Barsoum, and, Y. Gogotsi, "*Two-Dimensional Titanium Carbide MXene As a Cathode Material for Hybrid Magnesium/Lithium-Ion Batteries",* ***ACS Applied Materials & Interfaces***, 2016, DOI: 10.1021/acsami.6b04198.
2. M. Ghidiu, J. Halim, S. Kota, D. Bish, Y. Gogotsi, and, M.W. Barsoum, "*Ion-Exchange and Cation Solvation Reactions in Ti_3C_2 MXene",* ***Chemistry of Materials***, 2016, 28, pp. 3507-3514.
3. T. Lapauw, K. Lambrinou, T. Cabioc'h, **J. Halim**, J. Lu, A Pesach, O Rivin, O Ozeri, EN Caspi, L. Hultman, P Eklund, J. Rosen, M.W. Barsoum, and, J. Vleugels, "*Synthesis of the New MAX Phase Zr_2AlC",* ***Journal of the European Ceramic Society***, 2016, 36, pp. 1847-1853.
4. K. Hantanasirisakul, MQ Zhao, P. Urbankowski, **J. Halim**, B. Anasori, S. Kota, CE Ren, M.W. Barsoum, and, Y. Gogotsi, "*Fabrication of $Ti_3C_2T_x$ MXene Transparent Thin Films with Tunable Optoelectronic Properties",* ***Advanced Electronic Materials***, 2016, 2, pp. 1600050-1600056.
5. **J. Halim**, S. Kota, M.R. Lukatskaya, M. Naguib, MQ Zhao, E.J. Moon, J. Pitock, J. Nanda, S.J. May, Y. Gogotsi, and, M.W. Barsoum, "*Synthesis and Characterization of 2D Molybdenum Carbide (MXene)",* ***Advanced Functional Materials***, 2016,26, pp. 3118-3127.
6. C.E. Ren, M.Q. Zhao, T. Makaryan, **J. Halim**, M. Boota, S. Kota, B. Anasori, M.W Barsoum and, Y. Gogotsi, *"Porous Two-Dimensional Transition Metal Carbide (MXene) Flakes for High-Performance Li-Ion Storage*", ***ChemElectroChem***, 2016, 3, pp. 689-693.
7. T. Lapauw, **J. Halim**, J. Lu, T. Cabioc'h, L. Hultman, M.W. Barsoum, K. Lambrinou, and, J. Vleugels, "*Synthesis of the Novel Zr_3AlC_2 MAX Phase*", ***Journal of the European Ceramic Society***, 2016, 36, pp. 943-947.
8. J. Yang, M. Michael, M. Ghidiu, L.M. Pan, J. Gu, J. Nanda, **J. Halim**, Y. Gogotsi, and, M.W. Barsoum, "*Two-Dimensional Nb-Based M_4C_3 Solid Solutions (Mxenes)*", ***Journal of the American Ceramic Society***, 2016, 99, pp. 660-666.
9. **J. Halim**, K.M. Cook, M. Naguib, P. Eklund, Y. Gogotsi, J. Rosen, and M.W. Barsoum, "*X-ray Photelectron Spectroscopy of Select Multi-layered Transition Metal Carides (MXenes)*", ***Applied Surface Science***, 2016, 362, pp. 406-417.
10. A. Miranda, **J. Halim,** M.W. Barsoum, and, A. Lorke, "*Electronic Properties of Freestanding $Ti_3C_2T_x$ MXene Monolayers*", ***Applied Physics Letters,*** 2016, 108, pp. 033102-033104.
11. R. Meshkian, LÅ Näslund, **J. Halim**, J. Lu, M. W. Barsoum, J. Rosen, "*Synthesis of Two-Dimentional Molybdenum Carbide, Mo_2C, from the Gallium Based Atomic Laminate Mo_2Ga_2C*", ***Scripta Materialia***, 2015, 108, pp. 147-150.
12. B. Anasori, M. Dahlqvist, **J. Halim**, E. J. Moon, J. Lu, B. C. Hosler, E. N. Capsi, S. J. May, L. Hultman, P. Eklund, J. Rosen, M. W. Barsoum. "*Experimental and Theoretical Characterization of Ordered MAX Phases Mo_2TiAlC_2 and $Mo_2Ti_2AlC_3$*", ***Journal of Applied Physics***, 2015, 118, pp. 0943041-0943414.
13. C. Hu, C. Li, **J. Halim**, S. Kota, D. J. Tallman, M. W. Barsoum, "*On the Rapid Synthesis of the Ternary Mo_2Ga_2C*", ***Journal of the American Ceramic Society***, 2015, 98, pp. 2713-2715.

14. L. H. Karlsson, J. Birch, **J. Halim**, M. W. Barsoum, and, P. OÅ. Persson, "*Atomically Resolved Structural and Chemical Investigation of Single MXene Sheets*", ***Nano Letters***, 2015, 15, pp. 4955-4960.
15. C. Hu, C.-C. Lai, J. Lu, **J. Halim,** L. Sun, J. Zhang, J. Yang, B. Anasori, J. Wang, Y. Sakka, L. Hultman, P. Eklund, J. Rosen, and, M. W. Barsoum, "*Mo_2Ga_2C: A New Ternary Nanolaminated Carbide*", ***Chemical Communications***, 2015, 51, pp. 6560-6563.
16. **J. Halim**, M.R. Lukatskaya, K.M. Cook, J. Lu, C.R. Smith, L.A. Laslund, S.J. May, L. Hultman, Y.Gogotsi, P. Eklund, and, M.W. Barsoum, "*Transparent Conductive Two-dimensional Titanium Carbide Epitaxial Thin Films*", ***Chemistry of Materials***, 2014, 26, pp. 2374–2381.
17. B. Anasori, **J. Halim**, J. Lu, C.A. Voigt, L. Hultman, and, M. W. Barsoum, "*Mo_2TiAlC_2: A New Ordered Layered Ternary Carbide*", ***Scripta Materialia***, 2014, 101, PP. 5-7.
18. M. Naguib, G. W. Bentzel, J. Shah, **J. Halim**, E. N. Capsi, J. Lu, L. Hultman, and, M. W. Barsoum, "*New Solid Solution MAX Phases: $(Ti_{0.5}, V_{0.5})_3AlC_2$, $(Nb_{0.5}, V_{0.5})_2AlC$, $(Nb_{0.5}, V_{0.5})_4AlC_3$ and $(Nb_{0.8}, Zr_{0.2})_2AlC$*", ***Materials Research Letters***, 2014, 2, pp. 233-240.
19. M.R. Lukatskaya, **J. Halim**, B. Dyatkin, M. Naguib, Y.S. Buranova, M.W. Barsoum, and, Y. Gogotsi, "*Room-Temperature Carbide-Derived Carbon Synthesis by Electrochemical Etching of MAX Phases*", ***Angewandte Chemie International Edition in English***, 2014, 53, pp.4877-4880.
20. M. Naguib, **J. Halim**, J. Lu, K.M. Cook, L. Hultman, Y. Gogotsi, and, M.W. Barsoum, "*New Two-dimensional Niobium and Vanadium Carbides as Promising Materials for Li-ion Batteries*", ***Journal of the American Chemical Society***, 2013, 135, pp. 15966-15969.
21. **J. Halim**, R. Abdel-Karim, S. El-Raghy, M. Nabil, and, A. Waheed, "*Electrodeposition and Characterization of Nanocrystalline Ni-Mo Catalysts for Hydrogen Production*", ***Journal of Nanomaterials***, 2012, 845673, pp. 1–8.
22. R. Abdel-Karim, **J. Halim**, S. El-Raghy, M. Nabil, and, A. Waheed, "*Surface Morphology and Electrochemical Characterization of Electrodeposited Ni-Mo Nanocomposites as Cathodes for Hydrogen Evolution"*, ***Journal of Alloys and Compounds***, 2012, 530, pp. 85-90.